Synthesis and Optical Characterisation of Barium Magnesium Aluminate Nanophosphors as Blue Light Emitting Source

A
Thesis
Submitted for the award of degree of

Doctor of Philosophy

By

Suninder Jeet
(Regn. No. 901112010)

Under the Supervision of

Dr. O. P. Pandey
Senior Professor and Head

School of Physics and Materials Science
Thapar Institute of Engineering & Technology, Patiala–147004

August 2019

DECLARATION

I hereby certify that the work presented in thesis entitled, **"Synthesis and Optical Characterisation of Barium Magnesium Aluminate Nanophosphors as Blue Light Emitting Source"**, submitted in partial fulfillment of the requirement for award of degree of "DOCTOR OF PHILOSOPHY", in the School of Physics and Materials Science, Thapar Institute of Engineering & Technology, Patiala (Punjab), India, is an exclusive record of my own research work under the supervision of Dr. O.P. Pandey. The thesis in part or in full has not been submitted in any other university or institute for the award of any degree.

Suninder Jeet

(Suninder Jeet)

This is to certify that the above statement made by the candidate is correct and true to the best of my knowledge.

Date: 21-8-2019

O P Pandey

Dr. O. P. Pandey

Senior Professor and Head

School of Physics & Materials Science

Thapar Institute of Engineering & Technology

Patiala – 147004

INDIA

Acknowledgements

The journey of my Ph.D. was a long one with its share of highs and lows. It has been a great learning experience for me on both professional and the personal fronts. Throughout these years, I have had great luck to work with many inspiring, competent and nice people who have contributed in assorted ways in research. It is a pleasure to convey my gratitude to everyone who has been helpful in the successful realization of this thesis.

In the first place, I owe my most sincere gratitude to the creator who shaped my dreams into reality, my mentor and supervisor, ***Dr. O. P. Pandey,*** for his dynamic and meticulous supervision and exemplary guidance all throughout the research work. I am indebted to him for his devoted time, positive criticism, timely advice and for providing with a conducive environment for research. His encouragement, moral support and care helped me to overcome all the hurdles and achieve my goals. His passion towards learning through continuous reading and humble nature has always been an inspiration for me. Perseverance, exuberance and affirmative approach are some of the traits he imprinted on my personality. I deem myself fortunate enough to work under his guidance. I solemnly submit my honest and humble thanks to him. Very special thanks to ***Mrs. Sushila Pandey*** who has been a constant source of moral support and encouragement throughout.

I am deeply grateful to the members of my Doctoral committee, ***Dr. B. N. Chudasama, Dr. D. P. Singh*** and ***Dr. Amjad Ali*** for their encouragement, helpful suggestions and perceptive comments during my progress report presentations. They have always shown their willingness to discuss ideas about the work. I owe my profound thankfulness to ***Dr. Kulvir Singh*** and ***Dr. N. K. Verma*** for their whole-heated support and blessings. I extend my sincere gratitude to all the faculty members of School of Physics and Materials science who always gave their timely help whenever required. Most of the results described in this thesis would not have been obtained without the help of few laboratories and institutes like ***Panjab University, Punjabi University, IIT Madras, JNU, IUAC***.

I would like to express my gratitude to ***Dr. D. Haranath***, Associate Professor in Physics at NIT Warrangal, for sparing his valuable time whenever I approached him and showing me the way ahead. I am thankful to ***Dr. Manoj Sharma***, Postdoctoral Research Fellow at NTU, Singapore, for sharing his expertise and valuable guidance in the initial stages of my work. Very special heartfelt thanks to ***Dr. Gurbinder Kaur,*** Research Scientist, for always motivating and encouraging me. I am indebted to her for her valuable guidance, scientific inputs and whole-hearted willingness to help. I could always look back on her for any support during my course of Ph.D. I feel privileged to be associated with a person like her during my life.

I wish to extend my warmest thanks to my dear friends and labmates ***Mr. Rameez Ahmed, Mr. Piyush Sharma, Ms. Shivani Bansal, Mr. Aayush Gupta, Ms. Damandeep Kaur, Mr. Sanjay Upadhaya, Mr. Puneet Vashisht, Ms. Shivani Jindal, Ms. Chhavi, Mr. Kaushlendra Pandey, Ms.***

Indu Gupta, Ms. Raveena and ***Ms. Yashpreet Kaur*** for their constant help and support in every way possible. A special mention of thanks to ***Ms. Ruby Priya*** for her constant support, timely help and cooperation. I would also like to thank some friends and co-workers from early days of my research tenure ***Dr. Samita Thakur, Dr. Chandni, Dr. Samiksha Verma, Dr. Pooja Singla, Dr. Suresh Kumar, Dr. Gaurav Singla, Dr. Manish Mittal, Dr. Jagdeep Kaur, Dr. Paramjot Jha, Ms. Navjot Kaur, Dr. Sakshi Gupta and Dr. Satwinder Singh*** for their valuable help during the initial stage of my work.

I would like to thank ***Mrs. Neelam, Mr. Inder Mani Mishra, Mr. Lal, Mr. Purshotam, Mr. Jant Singh, Mrs. Parveen, Mr. Pardeep*** and ***Mr. Vijay*** for their kind help and support in all the administrative work.

My special acknowledgement goes to my husband ***Dr. Deepak Kumar*** for his support and generous care. He has always been by my side during the difficult times and kept motivating me. I sincerely thank him for his encouragement and every possible help throughout my research work. A very special heartfelt thanks to my son ***Tejasveer***. Having him midway of my Ph.D. was certainly not easy but he has made my life wonderful. His smiling face has always made me happy and filled me with inspiration. Thank you my son for co-operating with me and sorry for having a little less of me. I would also like to extend a huge loving thanks to my sister ***Mrs. Maninder Jeet*** for her support, unconditional love and prayers. A very special mention of thanks to my niece ***Ms. Navnoor Kaur*****,** for her lovely smiles and chirpy talks always filled me with joy.

I dedicate this work to my mother ***Mrs. Manjeet Kaur*** and my father ***Er. Harbhajan Singh.*** My Ph.D. would have been a distant dream without the support, love, sacrifices and paryers of my parents. Their infallible support at this point of time made me realize my dreams. Their patience and sacrifices will always remain my inspiration. Words are not enough to express my gratitude towards them. I feel fortunate enough to have them as my parents. Without there help and support, I would have landed nowhere. **THANK YOU** for being there always and lifting me uphill this phase of life.

Besides this, I would like to extend my gratitude to one and all who have directly or indirectly helped me in the successful completion of this work.

Above all, I thank ***Almighty*** for giving me strength and courage to carry out my work.

Suninder Jeet

LIST OF PUBLICATIONS

1. Template free synthesis route to monophasic $BaMgAl_{10}O_{17}:Eu^{2+}$ with high luminescence efficiency, Suninder Jeet and O. P. Pandey, **Journal of Alloys and Compounds, 750 (2018) 85-91**.

2. The effect of templates on the morphological and optical properties of $BaMgAl_{10}O_{17}:Eu^{2+}$ phosphors, Suninder Jeet and O. P. Pandey, **Vacuum, 161 (2019) 119-124**.

3. Enhanced photoluminescence intensity of blue light emitting $BaMgAl_{10}O_{17}:Eu^{2+}$ phosphor with Dy^{3+} co-doping, Suninder Jeet and O. P. Pandey, **Journal of Materials Science: Materials in Electronics, 31 (2020) 1116-1125**.

Conferences Attended

1. Attended International Conference on Emerging Trends in Physics for Environmental Monitoring & Management (ETPEMM-12), held at Punjabi University, Patiala, from February 13-15, 2012.
2. Attended International Conference on Recent Trends in Applied Physics & Material Science (RAM 2013), held at Govt. College of Engineering & Technology, Bikaner, from February 1-2, 2013.
3. Presented poster on "Morphological and Optical Characterization of Europium Doped Barium Magnesium Aluminate Phosphors", at International Conference on Nano Science and Technology (ICONSAT-2014), held at Punjab University, Chandigarh, from March 3-5, 2014.
4. "Synthesis and Optical Study of Barium Magnesium Aluminate Blue Phosphors", Suninder Jeet and O. P. Pandey, **AIP Conference Proceedings, 1661, 100005 (2015) 1-5**, presented poster at International Conference on Condensed Matter Physics (ICCMP – 2014), held at Himachal Pradesh University, Shimla, from November 4-6, 2014.
5. Presented Poster on "Investigation on Structural and Optical Properties of Dy^{3+} Sensitized $BaMgAl_{10}O_{17}:Eu^{2+}$ Nanophosphors", at International Symposium on Functional Materials (ISFM-2018), held at Hotel Shivalik View, Chandigarh, from April 13-15, 2018.

Index

Contents *Page No.*

List of Figures

Contents *Page No.*

CHAPTER 1: INTRODUCTION

CHAPTER 3: EXPERIMENTAL TECHNIQUES

CHAPTER 4: RESULTS AND DISCUSSION – I

CHAPTER 5: RESULTS AND DISCUSSION – II

CHAPTER 6: RESULTS AND DISCUSSION – III

List of Tables

Contents *Page No.*

CHAPTER 5: RESULTS AND DISCUSSION - II

CHAPTER 6: RESULTS AND DISCUSSION - III

PREFACE

Extensive research has been carried out on the blue light emitting phosphors till date. The blue phosphor is an important and promising candidate in display and lighting technology. $BaMgAl_{10}O_{17}:Eu^{2+}$ ($BAM:Eu^{2+}$) is the commercially used blue phosphor. The present work studies the photoluminescence properties of $BAM:Eu^{2+}$ nanophosphors prepared by solution combustion synthesis process. Activator concentration, phase purity, crystallinity and morphology are the governing factors for high luminescence efficiency for any phosphor. Based on these factors various techniques were used and studied to enhance the photoluminescence efficiency of the $BAM:Eu^{2+}$ nanophosphors. The entire work in this thesis is presented in seven chapters. The outline of these seven chapters is given below.

Chapter 1 discusses the fundamentals of photoluminescence giving an insight into the trivalent and divalent rare earth ions as luminescent centers. This chapter also covers some important topics explaining luminescence phenomenon in phosphors. Red, green and blue light emitting phosphors are discussed concisely. Applications of phosphors are given in brief. Importance of blue phosphors and a brief introduction to $BaMgAl_{10}O_{17}$ host material concludes the chapter.

Chapter 2 summarizes current research in the field of phosohors. Earlier reported work of various researchers has been reviewed. Effect of various parameters on morphological and optical properties of BAM has been given. The chapter discusses BAM phosphors along with different synthesis routes, effect of co-doping, alkali ion incorporation, polymer addition, theoretical assessment and degradation mechanism. The last section of the chapter gives gaps in the study and the objectives for the work presented in the thesis.

Chapter 3 gives the experimental details followed for the synthesis of the materials and different characterization techniques used during the course of present study. The complete procedure of the synthesis technique along with different molar concentrations of different dopants, co-dopants and surfactants are given. Details of different techniques and instruments employed to characterize the prepared samples has been given in terms of their instrument names, model number and operating conditions. Sample names with their corresponding codes have been listed systematically in tabular form.

Chapter 4 studies the photoluminescence properties of BAM:Eu^{2+} phosphor and the effect of pure phase on the photoluminescence properties of BAM:Eu^{2+} nanophosphor. The BAM:Eu^{2+} nanophosphor was prepared by solution combustion synthesis method. The modification in the synthesis route in terms of two additional steps namely acid leaching and annealing and their affect on the morphological and optical properties of BAM:Eu^{2+} nanophosphor has been discussed. To check the efficiency of the prepared nanophosphors, their CIE color coordinates and color purity has been calculated.

Chapter 5 presents the effect of morphology on the photoluminescence efficiency of BAM:Eu^{2+} nanophosphor. β-cyclodextrin (β-CD) and thioglycerol (TG) were used as tempalate agents during synthesis of BAM:Eu^{2+} nanophosphors by solution combustion synthesis route. The enhancement in photoluminescence emission intensity of BAM:Eu^{2+} nanophosphor due to change in morphology through β-CD and TG inclusion has been discussed in detail. The CIE color coordinates and thermal stability results of the prepared nanophosphors has been studied to check their efficiency and applicability.

Chapter 6 gives the detailed study on the effect of substitution or co-doping of Dy^{3+}, Ca^{2+} and alkali metal ions Li^{+}, Na^{+} and K^{+} on the structural and optical properties of BAM:Eu^{2+} nanophosphor prepared by solution combustion synthesis method. The chapter has been divided into three sections. The first section studies the effect of Dy^{3+} ions co-doping on structural and optical properties of BAM:Eu^{2+} nanophosphor. Thermoluminescence study of BAM:Eu^{2+} /Dy^{3+} nanophosphor has been analysed to obtain information about the traps created. The photoluminescence properties of BAM:Eu^{2+} /Dy^{3+} nanophosphor has been studied in detail. The second section of this chapter deals with the effect of alkali metal ion on the optical properties of BAM:Eu^{2+} nanophosphor. The third section studies the effect of Ca^{2+} co-doping on photoluminescence efficiency of BAM:Eu^{2+} nanophosphor. A detailed discussion has been given on the increase in the photoluminescence emission intensity of BAM:Eu^{2+} nanophosphor due to co-doping of these ions. The CIE color coordinates and color purity of all the samples have been calculated. Also, to check the usability and the efficacy of the prepared phosphors thermal stability of all the prepared phosphors has been studied.

Chapter 7 summarizes and concludes the results obtained from the structural, morphological and optical characterisations of the samples prepared through different experiments and variations as discussed in the previous chapters. Finally, at the end of the chapter some suggestions for the future study in this field are given.

CHAPTER 1

INTRODUCTION

Overview

The research in the field of photoluminescence is growing rapidly. The present chapter addresses the basic concepts involved in photoluminescence mechanism and discusses the influence of trivalent and divalent rare earth ions as luminescent centers. Phosphors emitting red, green and blue light are discussed. The applications of phosphors in various fields is given. The chapter is concluded with importance of blue phosphors and a brief introduction to $BaMgAl_{10}O_{17}$ host material.

1.1. Introduction

The 21st century is a digitally smart world where fast emerging modern societies are getting closer with the advancement in technology. Smart devices, smart screens and smart lighting are the buzzwords of the 21st century. Electronic displays act as a human – electronic interface in various devices such as computers, mobile phones, TV and human visual systems. Every one of these devices use luminescent materials, likewise called phosphors. Phosphors are materials emitting photons after excitation by some external energy source like ultraviolet light or light of any wavelength in the electromagnetic spectrum range. This phenomenon involving energy absorption and photon emission is called luminescence. In luminescence phenomenon, a substance releases excess of its energy as electromagnetic radiation either quickly or over some stretch of time. The excitation is in the form of some external energy like electromagnetic radiation or electron beam. Depending on the type of excitation energy, luminescence can be grouped into photoluminescence, cathodoluminescence and so on. The different types of luminescence and their excitation sources are tabulated in table 1.1. Phosphors are generally solid inorganic materials, which are intentionally doped with impurities. Therefore, phosphor comprises of a host material like oxides, nitrates, phosphates, silicates and an impurity ion called activator. Rare earth ions are utilized as activators because they have weak interaction with host lattice due to the involvement of d electron and f-f transitions. For luminescence to occur, the energy absorption takes place by host lattice or by activator. Generally, activator ion absorbs excitation energy, gets excited and returns to ground state with subsequent emission of the photon. Second kind of impurity ion called sensitizer is doped if activator ions show weak absorption. Sensitizer upon absorbing excitation energy transfers the energy to activator, which then generates luminescence. Transport of energy through the luminescent material is the essence of this process. Thus, the luminescence process considers both the influence of host lattice and activator ion. The proper choice of emission ion, without changing the host lattice can lead to the modification of the emission color [1].

Table 1.1: Classification of luminescence

S.No.	Type of Luminescence	Excitation Source	Applications
1.	Photoluminescence	Electromagnetic Radiation	Fluorescent lamps, White LEDs, PDPs
2.	Cathodoluminescence	Electron beam	FED, CRT
3.	Electroluminescence	Electric Voltage	LEDs, Flat pannel displays, screens
4.	Triboluminescence	Mechanical Energy	Remote sensing
5.	X-Ray luminescence	X – Rays	X - Ray detectors
6.	Chemiluminescence	Chemical Reaction	Labeling and gas sensors
7.	Thermoluminescence	Heating	Dosimeters and detectors
8.	Radioluminescence	α – rays, β – rays, γ – rays	Scintilators

1.2. Fundamentals of Luminescence

1.2.1. Photoluminescence Mechanism

Excitation and emission are the basic working principles of luminescent materials or phosphors. As shown in figure 1.1 (a & b), after absorbing excitation energy, the activator ion A gets excited to an excited state A*, an unstable state. Then it returns to ground state with the radiation emission. This emission can be either radiative or non-radiative. Radiative emission results in photoluminescence. In non-radiative emission, the host lattice absorbs the liberated energy and heats the host lattice. The non-radiative emission does not result in photoluminescence instead the energy is lost in non-radiative emission. Therefore, to create efficient photoluminescent materials, the non-radiative emission should be minimum.

In luminescent materials where activator ions have weak absorption for excitation energy, another impurity ion called sensitizer is added to host lattice. The sensitizer S after absorbing the excitation energy gets excited to excited state S*. From here the energy is transferred to activator ion, which gets excited to the excited state A_1*, which is populated by energy transfer. The activator ion then undergoes non-radiative decay from excited state A_1* to slightly lower state A_2*. Subsequently, the activator ion from the state A_2* returns to ground state with radiative emission (photoluminescence emission) [2]. The non-radiative decay from A_1* to A_2* prevents back transfer. The activators and sensitizers that absorb excitation energy are called luminescent centers.

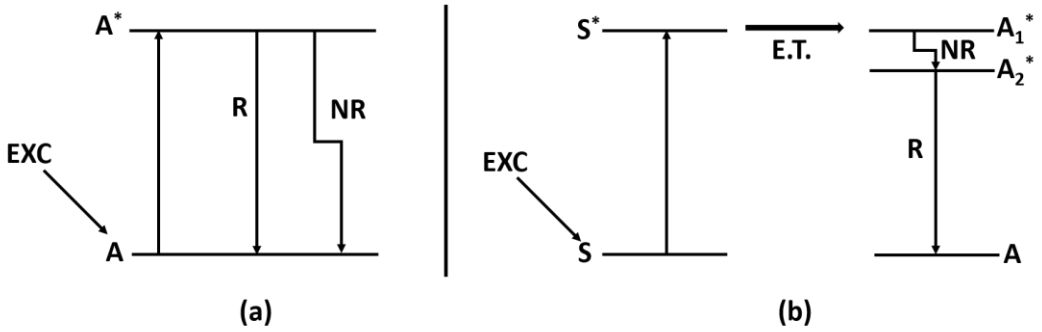

Figure 1.1 (a & b): Luminescent mechanism for luminescent ion. A is ground state, A^* is excited state of A, EXC is excitation, R is radiative return to ground state A, NR is non-radiative return to ground state A, S is sensitizer ion, S^* is excited state of sensitizer ion, E.T. is energy transfer, A_1^* is excited state populated by energy transfer, A_2^* is excited level slightly lower than A_1^* [2]

The significant processes that occur in a luminescent material are as follows:

1. Absorption of excitation energy by activator, sensitizer or host lattice.
2. Emission from activator.
3. Non-radiative emission.
4. Energy transfer.

These physical processes are discussed below:

1.2.2. Excitation

A luminescent material emits photons only after the absorption of required energy. The two types of excitation processes are namely, direct and indirect excitation. Direct excitation involves direct absorption of excitation energy for atoms to get excited. While, for indirect excitation, energy is first absorbed by the host lattice and then transferred to the excited state of activator ion. Energy requirement for direct excitation is less in comparison to indirect excitation because energy levels of activator ions lie in the middle of conduction and valence band of host material. Thus, direct excitation is more efficient than indirect excitation. The type of activator ion, for example, Eu^{2+}, Mn^{2+}, Eu^{3+}, Ce^{3+} etc. and host lattice determines the excitation spectrum of a phosphor [3]. UV and visible radiation can directly excite activators whereas; high-energy excitation is required for host lattice excitation. Shape of the excitation spectra can be broad or narrow. The configurational coordinate diagram interprets the width of the excitation

spectra, which is a potential energy curve where absorbing center varies as a function of configurational coordinate. For it, we assume a center metal ion surrounded by ligands as shown in figure 1.2 (a). The ligands move back and forth from the center metal ion in phase also called symmetrical stretching and the corresponding configurational coordinate diagram is shown in figure 1.2 (b). The value of equilibrium constant (R_o') is different for excited states. This difference is due to the different or weaker chemical bond in excited state when compared to ground state. Therefore, the parabolas for excited state are shifted by a value ΔR and $\Delta R = R_o' - R_o$. When optical energy is absorbed, the center from ground state is raised to the excited state. The optical transitions in configurational diagram are considered as vertical transitions because these transitions are optical transitions, whereas horizontal displacements correspond to nuclear transitions. Here *R* is internuclear distance. The movement of electrons is faster than nuclei, therefore, electronic transitions occur in nearly stable surroundings whereas; nuclei positions are adjusted later appropriately.

The optical energy is absorbed in the vibrational level v = 0 starting transition. Highest probability of transition is at R = 0 (figure 1.3). The transition ends at the periphery of the parabola for the excited state. At this point, excited state vibrational levels have highest amplitude and give the maxima of excitation spectra. The transition can also occur at values lower or greater than R_o. This energy difference decides the absorption bandwidth of the excitation spectrum. For larger energy difference, the absorption bandwidth is more and vice versa. The two parabolas overlap each other if R = 0, thus bandwidth vanishes and the spectra becomes a narrow line. The optical transition from ground state vibrational level to excited state vibrational level is relative to

$$\langle e|r|g\rangle \langle \chi_{v'}|\chi_o\rangle \quad (1.1)$$

Here electronic wave functions for excited and ground state are given by e and g respectively, r represents electric-dipole operator and vibrational wave function is given by χ [2, 4]. The first part of the equation (1.1) gives electronic matrix element whereas the second part gives vibrational overlap. Shape of absorption band is determined by the second part.

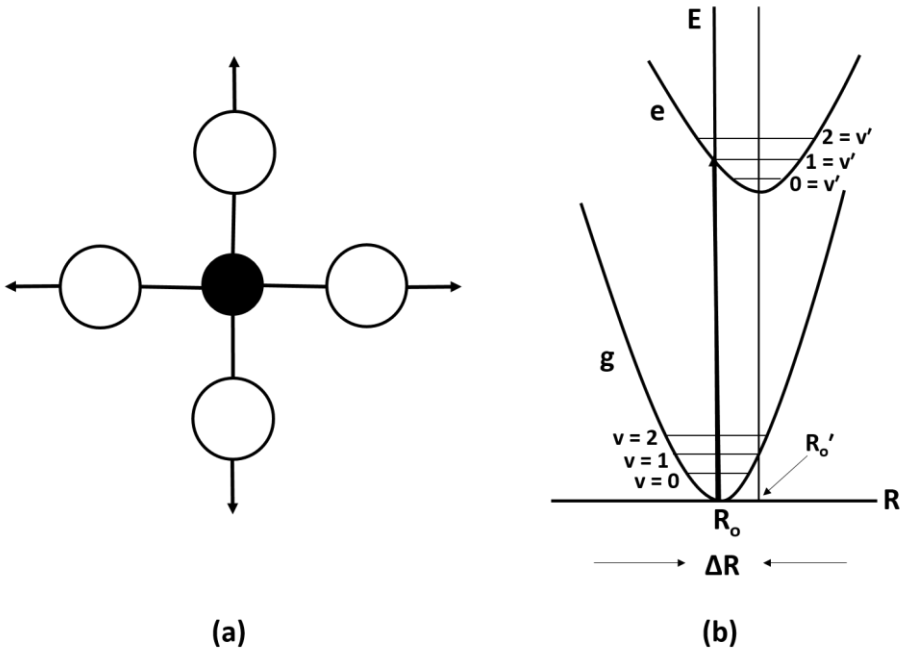

Figure 1.2: (a) Schematic representation of symmetrical stretching vibration for square-planar complex. The black circle is the center metal ion and open circles are the ligands. **(b)** is configurational coordinate diagram, where g is ground state, e is excited state, R is metal-ligand distance, Ro is equilibrium distance, Ro' is equilibrium distance for excited state, v represents vibrational states for ground state, v' represents vibrational states for excited state, ΔR is the shift between the excited state and ground state parabolas ($\Delta R = R_o' - R_o$) [2]

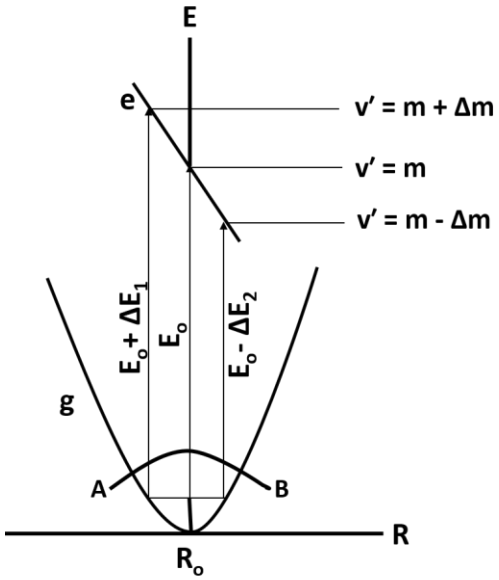

Figure 1.3: The optical absorption transition from ground state (g) to excited state (e) and curve AB represents broad absorption band [2]

1.2.2.1. Selection Rules

Electronic matrix element in the first part of the equation (1.1) gives the intensity of transition. However, probability of occurrence for every transition between various energy levels is not same as it is governed by selection rules. Thus, not every transition between ground state and excited state can be an optical transition. Only the transitions that fulfill the selection rules are the optical transitions. The two vital selection rules are:

1. **Spin selection rule ($\Delta S \neq 0$):** It prohibits the electronic transitions between different spin state levels.
2. **Parity selection rule:** It prohibits the electronic transitions between d and s shells, f shell and within d shell.

Despite selection rules, the prohibited transitions emerge with lesser intensity because of the various other factors that weaken these rules. These factors arise because of interactions between the atoms that produce hybrid electronic state. These hybrid electronic states become partially allowed because of the intermixture of opposite parity sites. As a result, weak forbidden transitions appear [2, 4].

1.2.2.2. Host Lattice Influence

Optical properties of luminescent center depend upon its surrounding ions. The same luminescent center exhibits different optical properties in different host lattices. Energy level and host lattice are the governing factors for the absorption band of a dopant ion. Since the neighboring ions in host lattice influence the energy levels of free ions, therefore, the nature of chemical bond between free ion and host lattice influence the excitation spectra of dopant ion. Two important factors affecting the excitation spectra are:

i. **Nephelauxetic Effect:** Covalency of bonds between ligand and the ion that absorbs energy is measure by this effect. With an increase in covalency, electrons spread out over wider orbitals i.e. the electron cloud expands, thus, reducing the electronic interaction. Therefore, due to the expansion of electron cloud, electronic transitions between energy levels shift to the lower energy end. As the expansion of electron cloud results in the shift so this effect is also called **cloud-expanding effect**. Parameter β measures the intensity of nephelauxetic effect and is given by equation (1.2).

$$\beta = \frac{(\sigma_f - \sigma)}{\sigma} \quad (1.2)$$

where energy of free ion is given by σ_f and absorption maxima by σ. Absorption maxima depends upon the type of host material [5].

ii. **Crystal Field Splitting:** Crystal field is an electric field present due to surroundings at the site of the ion. Crystal field is responsible for the splitting of certain optical transitions. Therefore, the strength of optical transitions depends on strength of the crystal field. For example, Cr_2O_3 is green and $Al_2O_3:Cr^{3+}$ is red despite the same crystal structure. This is because the Cr^{3+} ions in $Al_2O_3:Cr^{3+}$ occupy smaller Al^{3+} sites and hence experience strong crystal field as compared to Cr_2O_3. Therefore the optical transitions in $Al_2O_3:Cr^{3+}$ are at higher energy than in Cr_2O_3 and hence different color. Thus, different host lattices have different crystal fields, which give different splitting. Therefore, the optical center serves as the probe of the surroundings. The absorption band for 4f-5d electronic transitions is strongly influenced by the surroundings of the rare earth ions whereas for 4f-4f interconfigurational transitions the absorption band does not vary with the host lattice because 4f electrons are well shielded by outer electrons.

1.2.3. Emission

After excitation energy is absorbed by a luminescent system, the ion that absorbs energy gets promoted to a higher vibrational level of its excited state where a part of its energy is released. The center first returns to the lowest vibrational level of its excited state thus, bringing the exciting ions to their equilibrium state. This release of energy is a low-intensity non-radiative process known as relaxation. Figure 1.4 shows the configurational coordinate diagram of emission process. Excited ion returns to its ground state from a lowest vibrational level of excited state with spontaneous radiation emission and the ion reach some high vibrational level of ground state. Then, after relaxation, it reaches the lowest vibrational level of ground state. Selection rules for excitation and emission process are the same. However, excitation occurs in the presence of some radiation field whereas, emission is a spontaneous process.

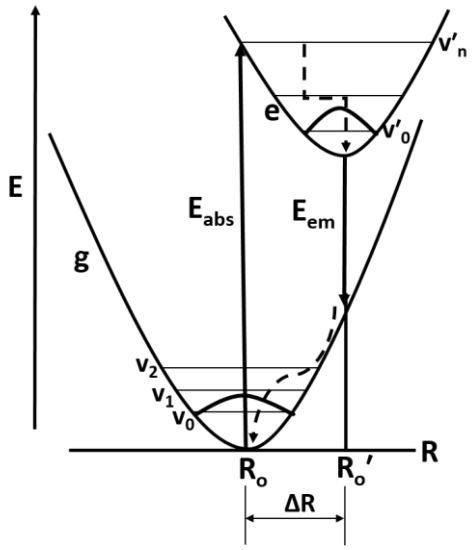

Figure 1.4: Configurational coordinate diagram explaining emission and relaxation processes. ΔR gives the parabola offset [3]

1.2.3.1. Stokes Shift: The emission occurs at an energy lower than that of absorption because of the loss of some energy in the relaxation process ($E_{em} < E_{abs}$). The difference in energy between maxima of lowest excitation band and maxima of lowest emission band of same electronic transition is called **Stokes shift**. It is clear from figure 1.4 that value of Stokes shift is directly proportional to ΔR. However, for achieving high luminescence a smaller value of Stokes shift is desirable. If in figure 1.4, the two parabolas have same shape or equal force constants, then the Stokes shift (*SS*) is expressed as:

$$\mathbf{SS = 2Shv} \qquad (1.3)$$

Where hv gives the spacing between two vibrational levels and constant S is Huang-Rhys coupling constant.

1.2.3.2. Concentration Quenching: Increase in luminescent center concentration increases luminescence intensity of a given host lattice. Increase in concentration of luminescent centers increases absorption efficiency hence increasing luminescence intensity. After a critical value of luminescent centers is reached, the luminescence intensity starts decreasing and is called **concentration quenching**. Increase in luminescent centers concentration decreases the distance between luminescent centers hence decreasing the efficient energy transfer. Therefore, concentration quenching depends upon energy transfer between luminescent centers. Excitation

energy can be transferred to an enormous number of centers before radiative emission. There are certain amount of defects or impurities present in the phosphor materials, which act as the acceptors for this excitation energy. If the distance between acceptors and donors is preferable for efficient energy transfer, then the excitation energy is transferred to these sites. In a non-radiative process, acceptors act as an energy sink and absorbed energy is relaxed to ground state. As acceptors quench the luminescence, they are also called **killers** and this phenomenon is called **donor-killer energy migration**. Some of the excitation energy is lost by **cross-relaxation**. In this mechanism, resonant energy transfer occurs between two identical centers adjoining each other having similar energy level structure. Therefore, cross-relaxation mechanism and donor-killer migration are the two factors accountable for concentration quenching [6].

1.2.4. Non-radiative Transitions

Transition from an excited state to ground state results in radiative emission but if the return to ground state is without emission of radiation then it is called **non-radiative return**. Luminescence quenching in phosphor material results in this non-radiative process. The most important requirement for a phosphor is its high luminescence output therefore; the non-radiative processes for a good phosphor should be minimum. The non-radiative processes that challenge the radiative emission are given below:

1.2.4.1. Multiphonon Emission: It is a non-radiative de-excitation process. Figure 1.5 (a & b) shows configurational coordinate diagram for strong and weak lattice coupling respectively. For strong electron lattice coupling parabolas for excited and ground state cross each other whereas, for weak electron lattice coupling the two parabolas do not cross each and are parallel. Luminescent center upon absorption of energy reaches point P at excited state as shown in figure 1.5 (a). In normal cases, the luminescent center returns to lowest vibrational level through relaxation, and then returns to ground state with photon emission. Whereas, with the presence of cross point Y, luminescent center is first relaxed to a level corresponding to point Y. This vibrational level corresponding to point Y belongs to ground state as well as to the excited state. Therefore, the probability of de-excitation through the level corresponding to point Y is higher via phonon states of ground state parabola. The luminescent center thus returns to ground state through non-radiative multiphonon emission. As the two parabolas are not crossing in figure 1.5 (b) therefore, non-radiative de-excitation is not possible for this case. Here, de-excitation takes

place at point B transferring instantaneously to point C and relaxing non-radiatively reaching at point A. Generally, this kind of multiphonon emission is observed for RE^{3+} rare earth ions.

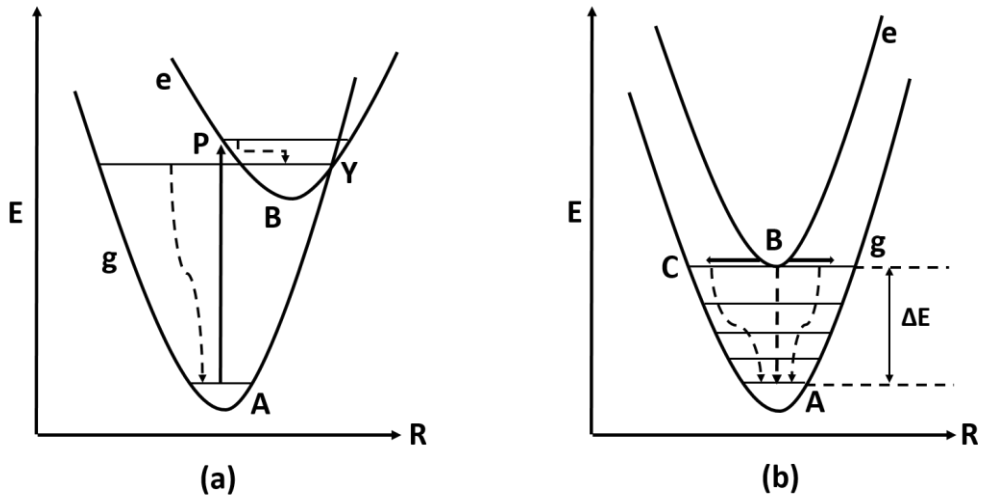

Figure 1.5: Configurational coordinate diagram for **(a)** Strong electron-lattice coupling multiphonon emission and **(b)** weak electron-lattice coupling multiphonon emission [3]

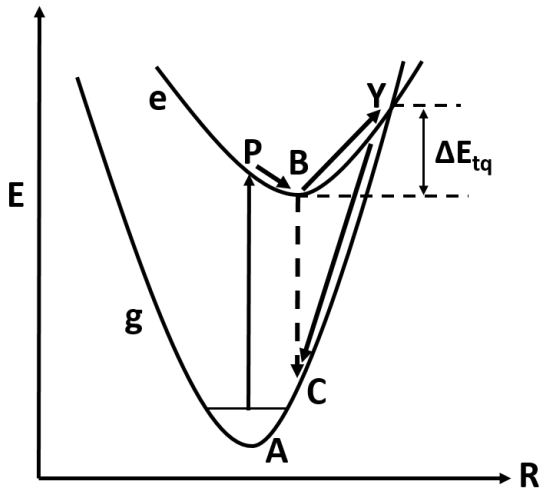

Figure 1.6: Configurational coordinate diagram for thermally activated non-radiative de-excitation process [3]

1.2.4.2. Thermally Activated Non-radiative De-excitation: Multiphonon emission occurs if the cross point Y is at an energy level below point P. If point Y is at an energy level higher than point P as shown in figure 1.6, the luminescent center after excitation reaches point P and then non-radiative relaxation occurs to point B. With the increase in temperature, the center gets thermally activated from point *B* to point Y and reaches the ground state via phonon states of excited state

(line YC) without emitting phonons thus quenching the luminescence. The energy gap between points B and Y decides the probability for thermally activated non-radiative de-excitation process.

1.2.5. Energy Transfer

Another possibility for the return from excited state to ground state is energy transfer. Here the excited luminescent center returns to ground state after transferring excitation energy to center A from excited center S^* as shown in figure 1.1 (b) and the process is given by equation 1.4.

$$S^* + A \rightarrow S + A^* \quad (1.4)$$

Sensitizer S transfers its energy to A exciting it to A^* and A* can also decay non-radiatively [2]. Energy transfer between two centers occurs only if there is certain interaction between the two centers. The probability for energy transfer is high for strong spectral overlap of donor emission and acceptor absorption. The coincidence of donor and acceptor energy levels lead to strong spectral overlap. It is called **resonant energy transfer** [6].

Interaction between donor-acceptor centers depend upon the distance between donor-acceptor centers and their wave functions nature. The donor-acceptor interaction is also called **Hamiltonian interaction** and it is of three types namely, multipolar electric interactions, multipolar magnetic interactions, and exchange interactions.

i. **Multipolar Electric Interactions:** Multipolar electric transitions depend upon the type of interactions between donor and acceptor. If R is the distance between acceptor and donor, then energy transfer probability from donor to acceptor depends upon R^{-n} where n = 6, 8 and 10 for three types of multipolar electric interactions: electric dipole-dipole interactions, electric dipole-quadrupole interactions, and quadrupole-quadrupole interactions respectively.
ii. **Multipolar Magnetic Interactions:** These interactions are similar to multipolar electric interactions and have same distance dependence for energy transfer probability as in multipolar electric interactions.
iii. **Exchange Interactions:** Such interactions take place when there is a direct overlap between electronic wave functions of acceptor and donor ions. There is an exponential

dependency of exchange interaction probability upon distance between acceptor and donor ions [6].

Non-radiative energy transfer process decreases the luminescence decay time of donor center and less decay time yields efficient phosphors. Thus, this process of non-radiative energy transfer is helpful in tuning the emission color, and in improving the efficiency of phosphors.

1.3. Luminescent Centers

So far, the physical processes of luminescent centers in a solid material are discussed. Luminescent centers are capable of creating new emission and absorption bands by introducing fresh energy levels within the energy gap of solid materials. Transition metal ions and rare earth ions are efficient luminescent centers.

1.3.1. Rare Earth Ions

Rare earth ions are frequently used as luminescent centers. Lanthanide ions in their divalent or trivalent state are doped in the crystals as luminescent centers in the phosphors. Lanthanide ions are created by the ionization of atoms in the periodic table after lanthanum. The electronic configurations for lanthanide ions are given in table 1.2. The lanthanide ions have partially filled 4f orbitals as seen in table 1.2. There are only three stable divalent lanthanide ions viz. Eu^{2+}, Sm^{2+}, and Yb^{2+}. Some of the 5d, 6s and 4f electrons in trivalent lanthanide ions are removed to obtain RE^{3+} ions whereas, divalent ions contain one extra f electron as compared to their trivalent counterpart. For example, Eu^{3+} has six 4f electrons and Eu^{2+} has seven 4f electrons. So, the trivalent lanthanide ions show 4f-4f interconfigurational optical transitions besides divalent lanthanide ions show 4f-5d interconfigurational optical transitions. That is why; both trivalent and divalent ions show different luminescent properties.

1.3.1.2. Trivalent Rare Earth Ions

The outer electronic configuration for trivalent lanthanide ions, in general, can be written as $5s^2\ 5p^6\ 4f^n$ where n varies from 1 to 13. Therefore, optical transitions of trivalent lanthanide ions are due to 4f electrons. Ligand ions in the host crystal do not affect much the 4f electrons as they are effectively shielded by 5s and 5p electrons. Therefore, 4f-4f interconfigurational optical transitions are involved in trivalent lanthanide ions. Whether the luminescence spectra is a broadband spectrum or sharp line spectra depends upon the type of rare earth ion. For all

trivalent lanthanide ions, sharp line luminescence spectrum is obtained owing to 4f-4f electronic transitions except Ce^{3+}, which shows a broadband luminescence spectra attributable to 4f-5d electronic transitions involved.

1.3.1.3. Divalent Rare Earth Ions

The only three divalent rare earth ions with 4f electronic configuration similar to Lu^{3+}, Eu^{3+} and Gd^{3+} are Yb^{2+}, Sm^{2+} and Eu^{2+} respectively. Divalent ions show broadband emission and excitation spectra because of the parity allowed $4f^n \rightarrow 4f^{n-1}$ 5d electronic transition. Emission and absorption characteristics of divalent rare earth ions are governed by its surroundings i.e. the host lattice. Thus, large variation is seen in the emission color for the same divalent rare earth ion but different host lattice.

Table 1.2: Electronic Configurations of trivalent and divalent lanthanide ions [3]

Trivalent Ions				**Divalent Ions**		
S.No.	**Ions**	**4f electrons**	**Ground State**	**Ions**	**4f electrons**	**Ground State**
1.	La^{3+}	0	$^1S_0$			
2.	Ce^{3+}	1	$^2F_{5/2}$			
3.	Pr^{3+}	2	$^3H_4$			
4.	Nd^{3+}	3	$^4I_{9/2}$			
5.	Pm^{3+}	4	$^5I_4$			
6.	Sm^{3+}	5	$^6H_{5/2}$	Sm^{2+}	6	$^7F_0$
7.	Eu^{3+}	6	$^7F_0$	Eu^{2+}	7	$^8S_{7/2}$
8.	Gd^{3+}	7	$^8S_{7/2}$			
9.	Tb^{3+}	8	$^7F_6$			
10.	Dy^{3+}	9	$^6H_{15/2}$			
11.	Ho^{3+}	10	$^5I_8$			
12.	Er^{3+}	11	$^4I_{15/2}$			
13.	Tm^{3+}	12	$^3H_6$			
14.	Yb^{3+}	13	$^2F_{7/2}$	Yb^{2+}	14	$^1S_0$
15.	Lu^{3+}	14	$^1S_0$			

1.4. Phosphors: Classification and Applications

Smart lighting and displays have immensely affected the lifestyle and architectural designs. They have become an important component of life in the modern world. Phosphors are required to generate visible light in both lighting and display technology. Therefore, the phosphors should have high reflectivity to visible light, high quantum efficiency and good color purity. Also, phosphor particle size distribution, shape and particle size are important physical requirements for phosphors.

1.4.1. Phosphor Classification

Phosphors are divided into different categories based on their emission color, chemical composition, and application. Here we are grouping the phosphors according to their emission color. So the phosphors can be divided into three groups corresponding to the basic primary emission colors namely:

i. **Red Phosphors:** For red phosphors, Eu^{3+} is the most commonly used activator in the conventional hosts such as Y_2O_3, Gd_2O_3, YVO_4, $LaBO_3$, $GdBO_3$ and YBO_3. These phosphors give sharp red emission near 595 nm, 611 nm, 615 nm and 619 due to $^5D_0 \geq {}^7F_2$ transition of Eu^{3+} ion and are used due to their high quantum efficiency, persistence characteristics and reduced saturation [7].

ii. **Blue Phosphors:** Blue phosphors use Eu^{2+} ion as activator. Eu^{2+} is doped in the hosts like $BaMgAl_{10}O_{17}$, $BaMg_2Al_{16}O_{27}$ and $Ba_{0.64}Al_{12}O_{18.64}$. The phosphors exhibit blue emission at 450 nm, 450 nm, and 435 nm respectively. The blue emission band corresponds to $4f^6$ 5d $\rightarrow$ $4f^7$ electronic transitions of Eu^{2+} ion.

iii. **Green Phosphors:** For green emission, Tb^{3+} is generally used as an activator and the hosts used as (La, Ce) $MgAl_{11}O_{19}$, (Ce, Gd) MgB_5O_{10} and (La, Ce) PO_4 [8]. Due to their high quantum efficiency and good thermal stability, they are widely studied and are applicable in plasma display panels. Other commonly used green phosphors are $BaAl_2O_4$:Mn^{2+} and $Li_2ZnGe_3O_8$:Mn, but Tb activated lanthanum phosphate and borate phosphors are superior in terms of their efficiency, stability and morphology.

Other different colors like yellow, orange, white etc. can be obtained with several combinations of hosts and rare earth ions but here we have discussed only the primary colors. In addition,

extensive research is going on to produce new phosphors, which are more efficient and stable than the common as well as commercially used red, blue and green phosphors.

1.4.2. Applications of Phosphors

Rare earth ions activated luminescent materials are of much interest and importance in technological applications like optoelectronic devices and flat panel displays. Principally the phosphors are capable of converting a type of energy into visible radiation; therefore, they are also termed as optical transducers. Rare earth ions have excellent luminescent characteristics because they have enormous allowed energy levels so the phosphors find huge applications in solid state lighting, imaging, radiation detecting, medical labeling etc. [9]. Figure 1.7 lists some of the applications of phosphors.

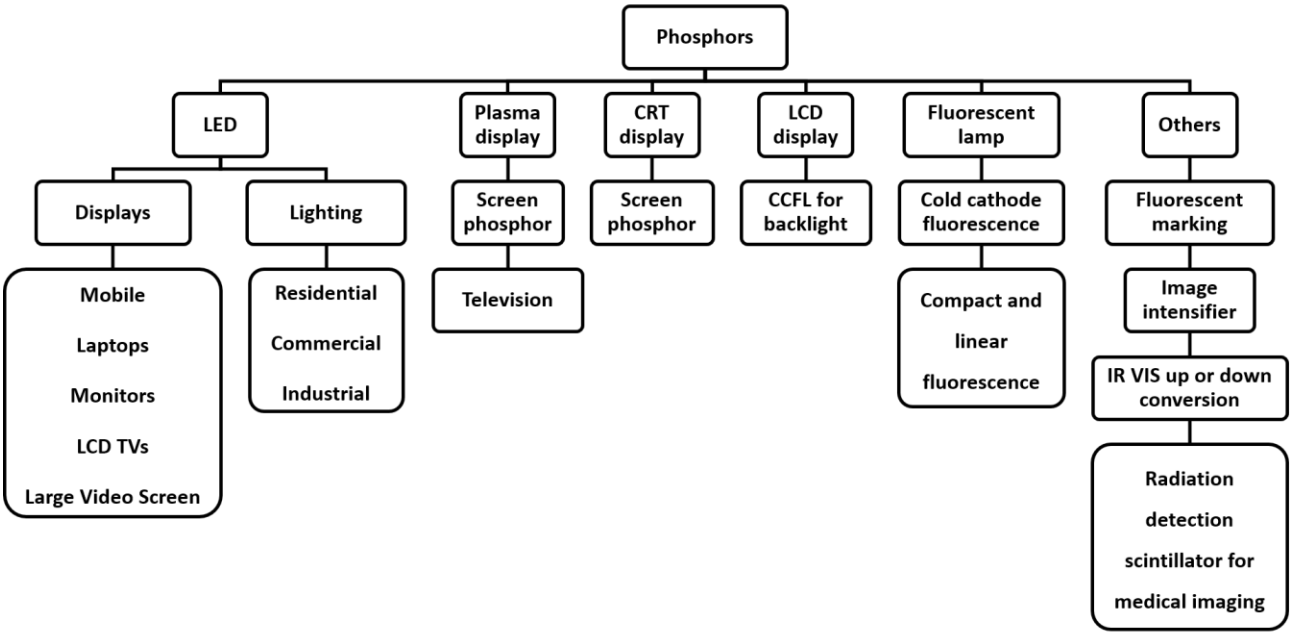

Figure 1.7: Various uses of phosphors [10]

1.5. Technological Importance of Blue Phosphors

Blue phosphor emerged as a most promising candidate for display technology. Blue light-emitting phosphors are useful for solid state lighting if a near UV LED (NUV LED) excites them. They convert radiation in 310 nm-410 nm range to blue light (420 nm-500 nm). Two activator ions of practical importance in the development of blue phosphors are Eu^{2+} and Ce^{3+}.

Luminescence bands of both the activators are due to 5d-4f transitions, which are very strong and show high quantum efficiency. Blue phosphors find wide applications in plasma display panels, mercury-free lamps, and fluorescent lamps. Plasma display panels were developed with Eu based blue phosphors. In recently developed white light-emitting diodes white emission was achieved by the partial conversion of blue light to lower energy emission. This conversion was possible by the use of phosphors, which were deposited on an LED chip as a thin layer. Phosphor converted LEDs obtain white light through the combination of blue, red and green LEDs. Separately using red, green and blue LEDs promises high efficiency. Therefore, intense and stable blue LEDs are of great help in generating white light from solid-state devices by combining the light from three LEDs (blue, red and green) or by color conversion of blue LEDs using phosphors [1]. Phosphors are also largely used in non-emissive displays as a backlight for example in solid-state lighting. The most important blue phosphor for this application is $BaMgAl_{10}O_{17}:Eu^{2+}$ ($BAM:Eu^{2+}$) phosphor. $BAM:Eu^{2+}$ is also of great importance for PDPs. $BAM:Eu^{2+}$ exhibits good quantum efficiency and high color purity with CIE chromaticity coordinates near ideal blue coordinates. The one drawback of $BAM:Eu^{2+}$ is its poor thermal stability and its shift towards green during panel fabrication. So the alternatives to $BAM:Eu^{2+}$ were developed such as $LaPO_4:Tm^{3+}$ [11], $CaMgSi_2O_6:Eu^{2+}$ [12], $Sr_3Al_{10}SiO_{20}Eu^{2+}$ [13], $(Ba,Mg)Al_2Si_2O_8:Eu^{2+}$ [14] etc. Although these new blue phosphors exhibited less degradation their luminescence efficiency was much lower than $BAM:Eu^{2+}$ making $BAM:Eu^{2+}$ an efficient blue light-emitting phosphor [15].

1.6. Introduction to $BAM:Eu^{2+}$

$BAM:Eu^{2+}$ is the most widely and commercially used blue phosphor. $BaMgAl_{10}O_{17}$ has hexagonal β-alumina structure which corresponds to space group P 63/m m c (figure 1.8). Its crystal structure is analogous to hexagonal β-alumina $NaAl_{11}O_{19}$. $BaMgAl_{10}O_{17}$ structure was obtained by the replacement of Na^+ with Ba^+ ions and through the partial replacement of Al^{3+} ions with Mg^{2+} ions. The structure consists of spinel blocks made up of $MgAl_{10}O_{16}$ separated by conduction planes or mirror planes of Ba – O. The oxide layer (Ba – O) comprises of barium ions and oxygen ions and is equivalent to Na – O layer in $NaAl_{11}O_{19}$. Whereas, $MgAl_{10}O_{16}$ spinel blocks have $MgAl_2O_4$ as spinel structures. So the $BaMgAl_{10}O_{17}$ structure comprises of two spinel blocks of $MgAl_{10}O_{16}$ divided by a conduction plane Ba – O (figure 1.8 (a)).

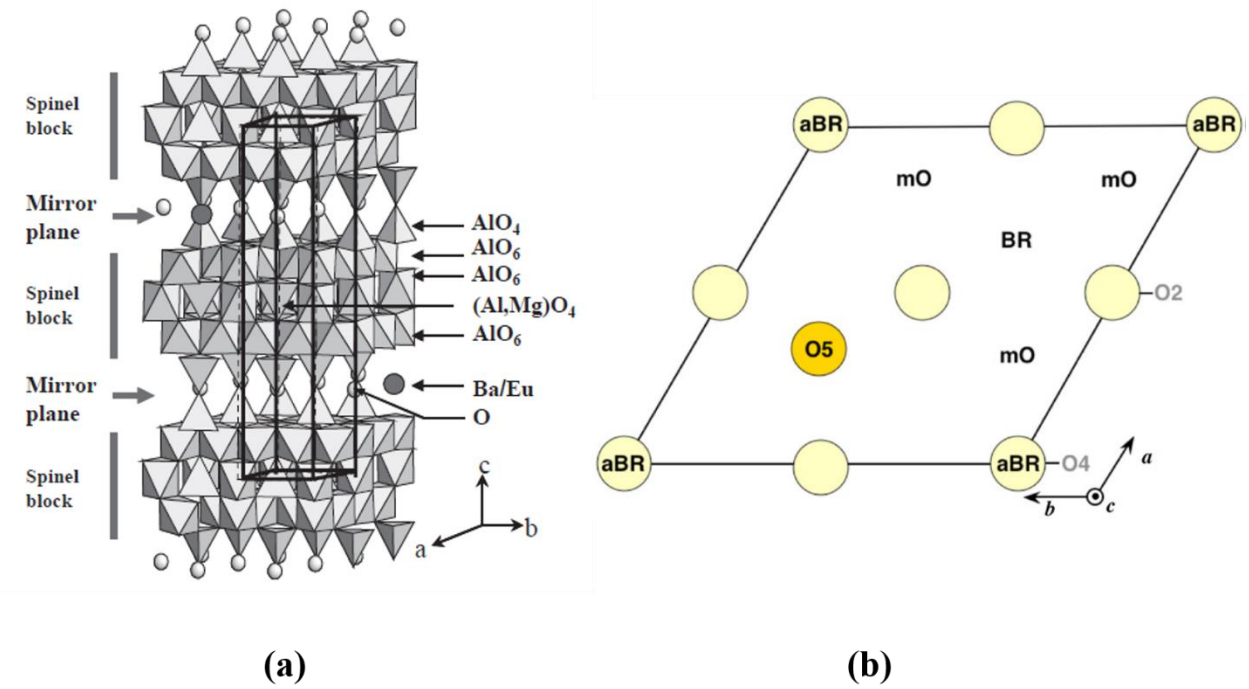

Figure 1.8: (a) Crystal structure of $Ba_{(1-x)}MgAl_{10}O_{17}:Eu_x^{2+}$ **(b)** BR, a-BR and mO sites for cations in z = ¼ plane [16, 17]

Eu^{2+} ions replace Ba ions in Ba – O conduction layer. On the substitution of Eu^{2+} ion in $BaMgAl_{10}O_{17}$ host lattice, Eu^{2+} ion can occupy three sites viz. Beevers Ross (BR), anti-Beevers Ross (a-BR) and mid oxygen (mO) sites within Ba – O layer as shown in figure 1.8 (b). BR site is substitutional site of Ba whereas mO and a-BR sites are the interstitial sites [18-22]. BR site is considered as the primary location for Eu^{2+} ion. The BAM:Eu^{2+} phosphor then shows broadband luminescence spectra around 450 nm corresponding to $4f^6\ 5d^1$ excited state to $4f^7$ ground state of divalent europium ion. BAM:Eu^{2+} phosphor displays high quantum efficiency of nearly 80%, good color purity and chromaticity [23]. It finds wide applications in display devices and lighting technology [9, 24-26].

References

[1] C.R. Ronda, Luminescence: from theory to applications, John Wiley & Sons, 2007.

[2] G. Blasse, B. Grabmaier, A general introduction to luminescent materials, in: Luminescent materials, Springer, 1994, pp. 1-9.

[3] R.-J. Xie, Y.Q. Li, N. Hirosaki, H. Yamamoto, Nitride phosphors and solid-state lighting, CRC Press, 2016.

[4] B. Henderson, G.F. Imbusch, Optical spectroscopy of inorganic solids, Oxford University Press, 2006.

[5] M. Gaft, L. Nagli, G. Waychunas, G. Panczer, The nature of red luminescence of natural benitoite $BaTiSi_3O_9$, Mineralogy and Petrology, 85 (2005) 33-44.

[6] J. Solé, L. Bausa, D. Jaque, An introduction to the optical spectroscopy of inorganic solids, John Wiley & Sons, 2005.

[7] S. Shionoya, W.M. Yen, H. Yamamoto, Phosphor handbook, CRC press, 2006.

[8] S. Ekambaram, K. Patil, M. Maaza, Synthesis of lamp phosphors: facile combustion approach, Journal of Alloys and Compounds, 393 (2005) 81-92.

[9] V. Pawade, H. Swart, S. Dhoble, Review of rare earth activated blue emission phosphors prepared by combustion synthesis, Renewable and Sustainable Energy Reviews, 52 (2015) 596-612.

[10] G. Balachandran, Extraction of Rare Earths for Advanced Applications, in: Treatise on Process Metallurgy: Industrial Processes, Elsevier, 2014, pp. 1291-1340.

[11] R. Rao, Tm^{3+} activated lanthanum phosphate: a blue PDP phosphor, Journal of luminescence, 113 (2005) 271-278.

[12] T. Kunimoto, S. Yamaguchi, K. Ohmi, H. Kobayashi, Luminescent and Aging Characteristics of Test-PDP Panel Using Gd-Codoped $CaMgSi_2O_6:Eu^{2+}$ Phosphors, in: Proc. IDW, 2004, pp. 1081-1084.

[13] S. Kubota, M. Shimada, $Sr_3Al_{10}SiO_{20}:Eu^{2+}$ as a blue luminescent material for plasma displays, Applied physics letters, 81 (2002) 2749-2751.

[14] W.B. Im, Y.-I. Kim, J.H. Kang, D.Y. Jeon, Luminescent and aging characteristics of blue emitting $(Ca_{1-x}, Mg_x)Al_2Si_2O_8:Eu^{2+}$ phosphor for PDPs application, Solid state communications, 134 (2005) 717-720.

[15] R.P. Rao, Recent developments in display phosphors, in: The 9th Asian Symposium on Information Display, 2006.

[16] K.Y. Jung, D.Y. Lee, Y.C. Kang, H.D. Park, Improved photoluminescence of $BaMgAl_{10}O_{17}$ blue phosphor prepared by spray pyrolysis, Journal of luminescence, 105 (2003) 127-133.

[17] J. Lambert, G. Wallez, M. Quarton, T. Le Mercier, W. van Beek, Searching for the dopant ion in Eu^{2+}-activated $BaMgAl_{10}O_{17}$ phosphor with synchrotron diffraction, Journal of luminescence, 128 (2008) 366-372.

[18] Y.-I. Kim, K.-B. Kim, M.-J. Jung, J.-S. Hong, Combined Rietveld refinement of $BaMgAl_{10}O_{17}:Eu^{2+}$ using X-ray and neutron powder diffraction data, Journal of luminescence, 99 (2002) 91-100.

[19] B. Howe, A.L. Diaz, Characterization of host-lattice emission and energy transfer in $BaMgAl_{10}O_{17}:Eu^{2+}$, Journal of luminescence, 109 (2004) 51-59.

[20] B. Dawson, M. Ferguson, G. Marking, A.L. Diaz, Mechanisms of VUV damage in $BaMgAl_{10}O_{17}:Eu^{2+}$, Chemistry of materials, 16 (2004) 5311-5317.

[21] K. Mishra, M. Raukas, A. Ellens, K. Johnson, A scattered wave model of electronic structure of Eu^{2+} in $BaMgAl_{10}O_{17}$ and associated excitation processes, Journal of luminescence, 96 (2002) 95-105.

[22] S.N. Manh, T.P.N. Thuy, Effects of Annealing on the Luminescence Properties of $BaMgAl_{10}O_{17}:Eu^{2+}$ Blue Emitting Phosphor, International Journal of Engineering and Innovative Technology, 3 (2013) 67-70.

[23] G. Bizarri, B. Moine, On $BaMgAl_{10}O_{17}:Eu^{2+}$ phosphor degradation mechanism: thermal treatment effects, Journal of luminescence, 113 (2005) 199-213.

[24] L.-J. Yin, J. Dong, Y. Wang, B. Zhang, Z.-Y. Zhou, X. Jian, M. Wu, X. Xu, J.R. van Ommen, H.T. Hintzen, Enhanced optical performance of $BaMgAl_{10}O_{17}:Eu^{2+}$ phosphor by a novel method of carbon coating, The Journal of Physical Chemistry C, 120 (2016) 2355-2361.

[25] N. Pradal, A. Potdevin, G. Chadeyron, P. Bonville, B. Caillier, R. Mahiou, Spectroscopic study and enhanced thermostability of combustion-derived $BaMgAl_{10}O_{17}:Eu^{2+}$ blue phosphors for solid-state lighting, Optical Materials, 64 (2017) 334-344.

[26] Q.Q. Zhu, X. Xu, L.Y. Hao, Synthesis of High-Performance $BaMgAl_{10}O_{17}:Eu^{2+}$ Phosphor Through a Facile Aqua-Suspension Method, International Journal of Applied Ceramic Technology, 12 (2015) 760-764.

CHAPTER 2

LITERATURE REVIEW

Overview

Extensive research is going on in the field of phosphors from the past many decades. Efforts are being made at research and industrial level to come up with more efficient and stable phosphors finding productive applications in display devices, lighting devices, sensors, energy saving applications etc. Therefore, it is important to study the literature and to learn more from the work of distinguished researchers. In the present chapter, earlier reported work is reviewed. The present chapter discusses the state-of-the-art of BAM phosphors along with different synthesis routes, effect of co-doping, alkali ion incorporation, polymer addition, theoretical assessment and degradation mechanism.

Divalent europium doped inorganic phosphors are very well known for their excellent optical properties like tunable emission wavelength from blue to red, high chemical stability, low toxicity and high brightness. Due to these excellent qualities, Eu^{2+} doped luminescent materials are potential candidates for various industrial and technological applications such as fluorescent lamps, sensors production, light-emitting diodes (LEDs) and emissive displays [1-7].

These days, to develop luminescent materials with improved performance, the surface conditioning of the phosphor is a major research area. Luminescent materials in field emission displays (FED) and plasma display panels (PDP) use high-energy side of UV spectrum, and vacuum ultraviolet (VUV) respectively. In fluorescent lamps for some applications and light-emitting diodes (LEDs, phosphors are excited by blue light or near UV light. The direct excitation of semiconductors by electrical current in LEDs and of inorganic/organic phosphor materials by inorganic/organic electroluminescence (EL) respectively, have been the most revolutionary aspect. Consequently, industry and university laboratories are indulged in vigorous search for the new materials in the area of luminescence [8-10].

2.1. Synthesis Techniques for the Phosphors

2.1.1. Combustion Synthesis

Mahakhode *et al.* [11] reported combustion synthesis of phosphors like $BaMgAl_{10}O_{17}:Eu^{2+}$, $SrMgAl_{10}O_{17}:Eu^{2+}$, $BaAl_{12}O_{19}:Mn^{2+}$, $SrAl_{12}O_{19}$:Ce, Gd, Mn, $GdCaAl_3O_7:Eu^{3+}$, etc. for plasma display panels (PDP). The synthesis is quick and can be carried out at the furnace temperature as low as 500 ^oC. It was confirmed from the XRD studies that all the aluminates have been formed in a single step except $Sr_3Al_{10}SiO_2$. Compound $CaAl_4O_7$ (CA4), $SrAl_4O_7$ (SA4), $CaAl_{12}O_{19}$ (CA12) and $SrAl_{12}O_{19}$ (SA12) were also prepared by single-step combustion synthesis method [12]. Monoclinic structure of $CaAl_4O_7$ and $SrAl_4O_7$ was confirmed with space group C2/c from XRD. $CaAl_{12}O_{19}$ and $SrAl_{12}O_{19}$ possessed a hexagonal structure with space group P63/mmc. For $CaAl_4O_7$, $SrAl_4O_7$, $CaAl_{12}O_{19}$ and $SrAl_{12}O_{19}$, the Eu^{2+} and Ce^{3+} ions preferentially occupy 12 and 7 coordinated Sr^{2+} and Ca^{2+} sites, respectively. Broadband emission with maxima at 330 nm and 355 nm could be seen for the Ce^{3+} doped $CaAl_4O_7$ and $SrAl_4O_7$ samples, respectively. Emission peak was observed at 429 nm, 460 nm, 413 nm and 406 nm for Eu^{2+} doped $CaAl_4O_7$, $SrAl_4O_7$, $CaAl_{12}O_{19}$ and $SrAl_{12}O_{19}$ phosphors, respectively. Verma *et al.* [13] prepared $SrMgAl_{10}O_{17}:Eu^{2+}$ via combustion process. They

varied the combustion temperature from 400°C to 700°C while varying the mixing and grinding time before and after combustion respectively. It was found that at low combustion temperature nanosized particles with low crystallinity were obtained whereas high combustion temperature produced highly crystallinity particles in nano to bulk range. Low temperature combustion process was found to be useful for blue light-emitting phosphors and high temperature combustion for red phosphors.

Chen *et al.*[14] prepared BAM:Eu^{2+} phosphors by novel solution combustion synthesis (SCS) technique. In order to control the morphology, polyethylene glycol (PEG) was used as an additive during preparation. Improvement in narrow particle size distribution, nearly spherical morphology, and strong blue emission under vacuum ultra violet (VUV) light excitation could be obtained with 5% PEG with MW 10,000. The same group [15] also used facile citrate sol-gel process to prepare BAM:Eu^{2+} blue phosphors. The results signified amorphous nature of the precursor. Additionally, a decrease of 300 °C in the synthesis temperature could be seen in comparison to BAM:Eu^{2+} prepared by solid-state method. In comparison to solid-state derived BAM:Eu^{2+} phosphors, sol-gel derived BAM:Eu^{2+} phosphors had pure phase with crystalline morphology, and high luminescent intensity. Zambar *et al.* [16] prepared Sm doped BAM phosphor (without citric acid) using combustion method. The phosphor doped with 2% Sm exhibited good emission with 254 nm wavelength. Pradal *et al.* [17] used microwave induced SCS technique to synthesize Eu^{2+}-doped barium magnesium aluminate phosphors. Urea and nitrates were used as fuel and oxidizer respectively. Fuel/oxidizer ratio was modified to control the purity of the as-synthesized particles. Fuel-rich reactions yielded pure phase whereas, stoichiometric fuel/oxidizer ratio resulted in impure phase. Another group reported synthesis of Eu^{2+} ion doped BAM blue phosphors with urea nitrate solution combustion synthesis technique at 590^{o}C [18]. The phosphors depicted hexagonal structure with the average particle size of nearly 50 nm. Broad emission spectra was obtained with emission maxima ta 455 nm.

2.1.2. Solid-State Reaction (SSR)

You *et al.* [19] synthesized Mn^{2+} doped x$BaO0.6Al_2O_3$ and $BaMgAl_{10}O_{17}$ phosphors using solid-state reaction method (SSR). It was suggested by the vacuum ultraviolet (VUV) excitation spectra, that 0.82$BaO0.6Al_2O_3$:Mn^{2+} and BAM:Mn^{2+} exhibited absorption at about 147 nm than the $BaO0.6Al_2O_3$:Mn^{2+} phosphor. It was also evident from the emission spectra under VUV excitation that the 0.82$BaOBa0.6Al_2O_3$:Mn^{2+} and BAM:Mn^{2+} tend to possess

higher luminescent intensity than $BaO0.6Al_2O_3:Mn^{2+}$. Similar decay times have been obtained from the lifetime analysis, indicating that $BAM:Mn^{2+}$ and $0.82BaOBa0.6Al_2O_3:Mn^{2+}$ could be the vital candidates as luminescent materials for plasma display panels (PDP). New green-emitting $Ba_2SiO_4:xEu^{2+},yGd^{3+}$, yR^+ (R = K, Na or Li) phosphors were synthesized through SSR method [20]. No significant influence of the Gd^{3+}, Eu^{2+} and R^+ ions doping on Ba_2SiO_4 phase could be seen. Green emission was obtained due to the $4f^6\,5d^1$ to $4f^7$ emission of Eu^{2+} ions. Inclusion of Li^+ ions in $(Ba, Gd)_2SiO_4$ host lattice, resulted in the highest photoluminescence (PL) emission intensity.

For $BaMg_2Al_6Si_9O_{30}:Eu^{2+}$ phosphors prepared by SSR method, the ultraviolet emission was initiated from the Eu^{2+}(I) replacing the Ba^{2+} sites and the blue emission was due to the substitution of the Eu^{2+}(II) at the Mg^{2+} sites [21]. With increasing europium content, blue emission band shifted towards longer wavelength. Additionally, the blue to ultraviolet emission PL intensity ratio also increased indicating that emission spectra could be tailored by altering Eu^{2+} concentration.

$BAM:Eu^{2+}$ blue phosphors and $CaAlSiN_3:Eu^{2+}$ red phosphors were prepared by SSR method [22]. These phosphors find application in plant growth LEDs through a dual emitting phosphor-in-glass plate (Dual-PiGP). Both phosphors showed high quantum efficiency and high stability. Dual-PiGP exhibited dual broad spectrum with full width at half maximum of 50 nm and 106 nm at 446 nm and 645 nm respectively. When used in indoor plant factory on Italian lettuce, it yielded good results with a 12.12% increase in biomass of Italian lettuce. So both the phosphors are potential options for next generation plant growth LEDs.

Ni *et al.* [23] synthesized blue-emitting phosphors $BAM:Eu^{2+}$ using high temperature SSR with different phases (α, β, and γ) of Al_2O_3 as preliminary materials. The phosphor synthesized using β - Al_2O_3 and γ - Al_2O_3 yielded greater surface area along with enhanced chemical activities. The decrease of the solid-state reactions starting temperature was observed for both these samples. For all the $BAM:Eu^{2+}$ samples, decay time was a single exponential giving almost same decay constant. Pure $BAM:Eu^{2+}$ phosphors were prepared using SSR with H_3BO_3 as a flux [24]. For the sintering duration of 2h at a temperature of 1100 ^oC, well-crystallized submicron $BAM:Eu^{2+}$ particles could be obtained. This approach yielded lower sintering temperature (almost by 400^oC), which could be acquired in smaller time duration as that of the conventional SSR method. The key factor affecting the sintering temperature for $BAM:Eu^{2+}$ was thought to be the reactivity of an intermediate $BaAl_2O_4$ phase. $BaCa_2MgSi_2O_8:Eu^{2+}$ phosphors were prepared using conventional SSR technique [25]. It was

inferred that Eu^{2+} ions occupy both Ba^{2+} and Ca^{2+} sites. Intense blue emission was obtained in comparison to the commercial BAM:Eu^{2+} phosphor.

2.1.3. Miscellaneous Synthesis Techniques and Coatings

Zhu *et al.* [26] prepared the BAM:Eu^{2+} phosphor using the sol–gel processes. The photoluminescence as well as the stability enhanced with the increasing firing temperature and Eu^{2+} concentration. The same group [27] coated nanometer SiO_2 on the BAM:Eu^{2+} phosphors to avoid the problems of thermal degradation during fabrication. An increase in luminescence intensity could be seen after coating, though no observable difference was seen for the VUV region. However, the thermal stability improved under both UV as well as VUV excitations. Carbon coated BAM:Eu^{2+} was synthesized by Yin *et al.* [28]. Annealing of the carbon-coated BAM:Eu^{2+} phosphor at temperatures ranging between 400°C to 1000°C reduced the carbon layers changing the phosphor color from black to white and increased PL intensity with increase in annealing temperature. Maximum photoluminescence intensity was obtained at annealing temperature 700°C because carbon reduced Eu^{3+} to Eu^{2+} hence increasing photoluminescence efficiency. Above this temperature, carbon disappeared completely and the oxidation of Eu^{2+} to Eu^{3+} started decreasing photoluminescence. The BAM:Eu^{2+} phosphors have also been coated with MgO via a precipitation route for the inhibition of surface oxidation [29]. The results implied enhanced thermal stability for these phosphors. BAM:Eu^{2+} phosphors were also surface modified by MgO coating with polyol method [30, 31]. MgO-coating on BAM:Eu^{2+} phosphors exhibited improved photoluminescence emission intensity in comparison to the unmodified ones. MgO-coated BAM:Eu^{2+} phosphors showed enhanced photoluminescence upon microwave irradiation. For mechanically ground phosphor powder, intensity of MgO coated BAM:Eu^{2+} increased with increase in MgO concentration. However, the purity was slightly disrupted due to an additional peak of $BaMg_3Al_{14}O_{25}$ at 470 nm. It was also observed that the blue-emitting phosphors exhibit better crystallinity and smoother surface after microwave irradiation in addition to the enhancement of intensity by six times.

A compact homogeneous MgF_2 coated BAM:Eu^{2+} particles were prepared an emulsion method [32]. Due to a decrease in non-radiative rate, fluorescence lifetimes was increased for MgF_2 coated BAM:Eu^{2+} phosphor. Hanging-bonds lead to better photoluminescent results for MgF_2 coated BAM:Eu^{2+}. SiO_2 nano-film was grown on BAM:Eu^{2+} phosphor through atomic

layer deposition technique to avoid the degradation problem [33]. The photoluminescence intensity for SiO_2-coated phosphors was higher than the pristine samples.

BAM:Eu^{2+} phosphors have also been prepared using simple nano-coating process [34]. The results indicated that the photoluminescence intensity of nano-coated phosphors was higher as compared to their solid-state derived counterparts. Microwave induced SCS method was used to synthesize BAM:Eu^{2+} nanophosphors [35]. These BAM:Eu^{2+} nanophosphors exhibited good crystallinity, spherical morphology and high blue emission when excited by vacuum ultraviolet (VUV) light in comparison the ones prepared by conventional SCS method. Ko *et al.* [36] implied aerosol flame deposition technique to develop BAM:Eu^{2+} particles with fine size and spherical shape. With an increase in precursor solution concentration and heat treatment, the particle size of the as-prepared powder increased. Photoluminescence spectrum could be seen at 450 nm and the photoluminescent intensity of the phosphor was 70% of that of the commercial phosphor.

2.2. Theoretical Assessment of Phosphors

Toyoshima *et al.* [37] performed first-principle calculations for 4f-5d absorption spectra on three emission centers of BAM:Eu^{2+}. The obtained results implied that BR site was the dominant site and formation of this additional band was due to the Eu^{2+} ions in mO site. Onuma *et al.* [38] by implying self-consistent charge tight-binding quantum chemistry method, carried out electronic structure calculations on BAM:Eu^{2+} phosphor. This model exhibited improvement in convergence for 4f orbitals. It was concluded from first-principles calculation that Beevers-Ross site is the most stable site for Eu atoms. Mishra *et al.* [39] used self-consistent field Xa scattered wave cluster molecular orbital approach theory to investigate the excitation spectrum of commercial BAM:Eu^{2+} phosphor. The comparison between the calculated and experimental excitation peak supported multiple site distribution of Eu^{2+} ions in BAME:u^{2+}.

Kajiyama *et al.* [40] studied the impact of plasma treatment on luminescence efficiency of BAM:Eu^{2+}. It was inferred from the results that the addition of hydrogen to the argon plasma markedly improved the lifetime of BAM:Eu^{2+}. The thermoluminescence and photoluminescence measurements showed that the hydrogen plasma reduced the electron traps concerned with degradation. It was also found from the PL measurements on BAM:Eu^{2+} that the hydrogen bridge formation somehow repaired the vacancies and/or defects in BAM crystal. Eu^{2+} emission has been investigated w.r.t. the pressure variable by Matysiak *et al.*

[41]. At high pressures, the resulting emission turned from blue to blue-green. The emission spectrum was fitted with three Gaussian, for which the positions and relative intensities were described as a function of pressure and excitation wavelength, respectively. The color shift and PL decrease of 500^{o}C annealed BAM:Eu^{2+} phosphors were investigated in UV and VUV regions by Zhang *et al.* [42]. Three important inferences which could be made from the results are as follows (1) both the migration/oxidation of Eu^{2+} contributed to the collective PL decrease, (2) a part of the energy is consumed by the new Eu^{2+} centers, which resulted in serious degradation under VUV excitation, and (3) the new formed Eu^{2+} centers emitting at long wavelength caused color shift.

Lambert *et al.* [43] used synchrotron powder diffraction to undertake extensive structural study related to europium ion in BAM:Eu^{2+} phosphor. It was observed that Eu^{2+} ions occupied three different locations viz. Beevers-Ross site, mid-oxygen site and interstitial site in the interblocks of Al-O-Al bridge. The major cause of the phosphor degradation was attributed to the vacancies produced at the Beevers–Ross sites caused by the migration of the activator ion.

Pentamodal distribution of Eu sites in the BAM:Eu^{2+} phosphor could be obtained from the ^{151}Eu Mössbauer spectroscopy with almost three site occupancy by Eu^{2+} [44]. The fourth and fifth site was most likely to be occupied by an Eu ion in a mixed-valence state and the trivalent europium ion, respectively. A sixth site could be observed upon oxidation, whose parameters were almost similar to those of Eu_{31} in EuF_3.

2.3. Doped/co-Doped Phosphors and Metal Ion Addition

Many groups have focused on the doping/co-doping of phosphors with europium, Dysprosium, manganese etc. [45-47]. Mn^{2+} and Eu^{2+} co-doped BAM phosphors were prepared using SSR method [48]. It was found that energy transfer between Mn^{2+} and Eu^{2+} was due to electric dipole-quadrupole interaction. Moist stability of the phosphor was enhanced upon addition of BaF_2 and AlF_3 fluxes. BaF_2 and CaF_2 were used as fluxes in flux assisted SSR method to prepare Ca doped BAM:Eu^{2+}, Mn^{2+} [49]. The inclusion of Ca ions decreased lattice constant and increased photoluminescence intensity of BAM:Eu^{2+}, Mn^{2+}. Xu *et al.* [50] investigated the influence of co-doping of Mg^{2+}, Si^{4+}, Na^{+}, and Li^{+} on photoluminescent properties of BAM:Mn^{4+} and α-Al_2O_3:Mn^{4+}. The addition of co-dopants enhanced the photoluminescence emission intensity by inducing energy levels and forming intrinsic defects. Mg^{2+} and Na^{+} ions created hole type defects whereas Li^{+} and Si^{4+} created both hole type defects and intrinsic

defects hence stabilizing Mn^{4+}. The effect of co-doping of Nd^{3+} and Er^{3+} on photoluminescent characteristics of BAM:Eu^{2+} was studied by Zhang *et al.* [51]. Upon excitation at 147 nm and 172 nm in VUV region BAM:Eu^{2+}, BAM:Eu^{2+}/Nd^{3+} and BAM:Eu^{2+}/Er^{3+} gave broadband emission peaking at 450 nm due to 4f-5d transition of Eu^{2+} ions. Photoluminescence intensity was increased with the doping of Nd^{3+} and Er^{3+} due to the increase in positive charge defects.

Photoluminescence characteristics of BAM:Gd^{3+} phosphor prepared by SCS method was studied by singh *et al.* [52]. BAM:Gd^{3+} phosphor exhibited narrowband UVB emission at 313 nm upon 272 nm excitation finding potential application in phototherapy lamps. Tigga *et al.* [53] investigated Ce doped BAM phosphor. The obtained phosphor related to β-alumina structure with P6 3/m m c space group same as that for BAM:Eu^{2+}. The BAM:Ce^{3+} phosphor exhibited two excitation peaks at 275 nm as well as at 330 nm and broadband emission at 440 nm located in blue region. The thermoluminescence (TL) properties were also studied to determine the nature of defects. From the TL glow curve four peaks were obtained indicating four trap levels. Linear TL response for low UV irradiation dose enabled its use for low-dose UV dosimetry. Fluorescence study of Sm doped BAM was performed by Zambare *et al.* [16]. BAM:Sm^{3+} phosphor emitted yellow light at 585 nm and was found good for applications in compact fluorescent lamps useful in protection from insects. Cho *et al.* [54] prepared green light-emitting Mn^{2+} doped BAM by flame spray pyrolysis. The powders with high crystallinity and good morphology were obtained. High photoluminescent intensity under 147 nm VUV light was observed for BAM:Mn^{2+}.

Shrivastava *et al.* [55] synthesized europium and dysprosium co-doped di-barium magnesium silicate phosphors under a weak reducing atmosphere. Uniform grain size distribution with regular surface was obtained. Green light-emitting $Ba_2MgSi_2O_7$:Eu^{2+}/Dy^{3+} phosphors when studied for phosphorescence decay properties with different Dy^{3+} concentration exhibited afterglow. Tunable $BaMg_2Al_6Si_9O_{30}$:Eu^{2+}/Tb^{3+}/Mn^{2+} was synthesized through SSR method by Lu *et al.* [56]. The obtained phosphor exhibited broadband excitation spectrum in the range 200 nm to 400 nm completely matching UV excitation light. Three emission colors were seen with a blue band peaking at 450 nm, green emission at 542 nm and red emission at 610 nm. Energy transfer occurred from Eu^{2+} to Tb^{3+} and from Eu^{2+} to Mn^{2+}. White color was achieved by tuning Mn^{2+} and Tb^{3+} relative ratio in $BaMg_2Al_6Si_9O_{30}$:Eu^{2+}/Tb^{3+}/Mn^{2+}.

Yerpude *et al.* [57] prepared europium and dysprosium doped $Ba_4Al_2O_7$ phosphors through combustion synthesis technique. $Ba_4Al_2O_7$: Eu^{2+} emitted blue light at 495 nm because

of $4f^6 5d^1$-$4f^7$ transition of Eu^{2+} ions. Whereas, $Ba_4Al_2O_7:Dy^{3+}$ emitted blue light at 478 nm and yellow light at 575 nm due to transitions of Dy^{3+} ions. The same group also synthesized $Sr_5SiO_4Cl_6:Dy^{3+}$ and $Sr_5SiO_4Cl_6:Sm^{3+}$ phosphors using modified solid-state method [58]. Here blue emission at 475 nm and yellow emission at 575 nm due to f-f transitions of Dy^{3+} ions in $Sr_5SiO_4Cl_6:Dy^{3+}$ phosphor was observed. $Sr_5SiO_4Cl_6:Sm^{3+}$ phosphor exhibited four emission peaks at 563 nm, 601 nm, 648 nm and 703 nm due to $^4G_{5/2}$ to $^6H_{5/2}$, $^6H_{7/2}$, $^6H_{9/2}$ and $^6H_{11/2}$ intra-4f shell electronic transitions respectively. However, emission at 601 nm gave intense orange color emission. Pawade *et al.* [59] reported Dy^{3+} luminescence in barium aluminosilicate phosphors prepared by combustion method at 600°C. When excitation was kept constant at 367nm, emission bands at 484 nm and 577 nm have been observed.

Various research groups investigated the effect of metal ions especially alkalis on luminescence properties of the phosphors. Wang *et al.* [60] studied the effect of metal ions by preparing BAM:Eu^{2+}/Mn^{2+} phosphors through flux assisted SSR reaction method. $(NH_4)_2CO_3$ and LiF were used as fluxes. Due to the incorporation of the fluxes the hexagonal shaped morphology of BAM:Eu^{2+}/Mn^{2+} transformed to spherical morphology. The spherical morphology increased the photoluminescence efficiency of BAM:Eu^{2+}, Mn^{2+} significantly. Rao [61] studied the effect of alkali halides and halides of ammonium and aluminum on morphological and optical properties of BAM:Eu^{2+} phosphor. The particles grown in the presence of LiCl were spherical whereas those in the presence of NaCl and KCl had plate like structure. Also the average particle size in the presence of fluxes was bigger in comparison to the ones grown without fluxes. It was inferred that the incorporation of alkali halides increased the photoluminescence and stability of BAM:Eu^{2+} for PDP applications.

The influence of the co-dopant concentration (K^+, Na^+ and Li^+) on optical properties of Y_2O_3 nanoparticles was investigated. It was found that the alkali metal ions incorporation improved the luminescence intensity. Zhu *et al.* [62] also studied the effect of Li^+ ion addition in $Y_2O_3:Eu^{3+}$ phosphors. It was found that the incorporation of Li^+ ions successfully enhanced the photoluminescence intensity of $Y_2O_3:Eu^{3+}$ phosphor. The smaller ionic radius of Li^+ ions shrinked the lattice and reduced the luminescence quenching OH^-group thereby increasing photoluminescence emission intensity of $Y_2O_3:Eu^{3+}$ phosphor.

Photoluminescence emission intensity of $Gd_2O_3:Eu^{3+}$ phosphor increased significantly with the addition of Na^+, Li^+ and K^+ ions [63]. Particularly, co-doping with Li^+ ions evidently improved the photoluminescence of $Gd_2O_3:Eu^{3+}$ nanophosphors as Li^+ ions have smaller ionic radius than Gd^{3+} ions.

2.4. Effect of Polymer Addition

Effect of polymer incorporation on morphology of phosphors was studied by various researchers. Zhou *et al.* [64] studied the effect of polyethylene glycol (PEG) and citric acid on the photoluminescence characteristics of BAM:Eu^{2+} synthesized by spray pyrolysis method. Submicron size (0.5 – 3 µm) and spherical shape particles were obtained. Morphology of phosphor particles was controlled by adding PEG of different molecular weights. The photoluminescence intensity was also increased with the addition of PEG. Spherical morphology and increased photoluminescence efficiency was obtained with PEG of 600 molecular weight. Zhang *et al.* [65] controlled the morphology of BAM:Eu^{2+} using PEG and β – cyclodextrin. The phosphor particles obtained rod-like morphology with PEG and flake-like morphology with β – cyclodextrin. The flake-like morphology exhibited stronger luminescence. Luminescent intensity for both the morphologies was stronger than the commercial BAM:Eu^{2+}.

Yang *et al.* [66] studied the effect of PEG2000, PEG10000, PEG20000, sodium dodecyl sulphonate and cetyltrimethylammonium bromide $CaMoO_4$:Eu^{3+} red phosphor. The addition of surfactants did not change the crystal structure but influenced the morphology of the phosphor particles which in turn affected the luminescence efficiency. Uniform sphere-like morphology and strongest luminescence intensity was obtained from PEG20000.

The morphology of the Y_2O_3:Eu^{3+} red phosphor prepared by spray pyrolysis was controlled by using polymeric precursor in spray solution by Sohn *et al.* [67]. Citric acid and ethylene glycol were used as polymeric precursors. Phosphor particles prepared without polymers had hollow and porous morphology. Whereas, spherical and dense morphology with high brightness was obtained by using polymers. Kumar *et al.* [68] used PVP and thioglycerol (TG) to control the morphology of Y_2O_3:Eu^{3+} red phosphor prepared via co-precipitation method. Particle size and morphology were greatly affected by TG and PVP addition.

Polymer/BAM:Eu^{2+} nanocomposite film was prepared from microwave-assisted combustion derived BAM:Eu^{2+} by Pradal *et al.* [69]. For the formation of films the phosphor powder was homogeneously dispersed in poly (N-vinylpyrrolidone) (PVP). Morphological and optical properties of BAM:Eu^{2+} phosphor powder did not change with the formation of nanocomposite film. Therefore the BAM:Eu^{2+} phosphor powder can be easily converted into a luminescent suspension and thus becomes a successful candidate for UV-LED based lighting

devices.

All the results indicated a vital role of surfactants in improving the photoluminescence intensity of phosphors by modifying their morphology.

2.5. Degradation Mechanism

The degradation of blue phosphor during the panel processing and operation is one of the most serious problem causing loss of efficiency as well as color purity [70, 71]. Many mechanisms are proposed for the thermal degradation as well as VUV degradation i.e. Eu^{2+} ion auto-ionization process, traps involvement during the fluorescence process, localized fluorescence quenching from the Eu^{2+} 5d bands at elevated temperatures and decrease in the fluorescence efficiency caused by the perturbation of the electron-hole pairs triggered by the VUV excitation via non-radiative transitions. The mechanism of the luminance decrease due to the baking process in BAM:Eu^{2+} phosphor was explained by Bizarri and Moine [72]. The annealing in the air caused the dopant oxidation, during which the decrease of Eu^{2+} ion concentration increased Eu^{3+} ion concentration, thereby leading to decrease in the traps concentration. Three different mechanisms for the degradation were proposed: diffusion of Eu^{2+} ions in the conduction layer of BAM:Eu^{2+}, surface adsorption of atmospheric oxygen into oxygen vacancies, oxidation of Eu^{2+} ions to Eu^{3+} ions.

Zhang *et al.* [73] studied the deterioration characteristics of the blue phosphors composed of 0.9BaO. 0.1EuO. MgO. mAl_2O_3 (m = 3.5 to 8.0). It was observed that the source alumina content significantly influenced the deterioration characteristics. Baking and VUV irradiation yielded different deterioration behavior. However, a small decrease in emission intensity of phosphor was obtained for the alumina content with m varying from 5.5 to 8.0.

Thermal degradation mechanism of BAM-Ba-hexaaluminate in context of its phase relation was discussed by Yokota *et al.* [74]. The thermal degradation of the BAM:Eu^{2+} was mainly attributed to the movement of oxygen ion in and out of the mirror plane of BAM crystal. ^{151}Eu Mössbauer spectroscopy results for the BAM:Eu^{2+} phosphor clearly established that the oxidation of activator i.e. Eu^{2+} ions mainly cause thermal degradation [44]. The Eu^{2+} at the three divalent sites act differently under the thermal degradation. Additionally, the Eu^{2+} populations at these sites decrease with the increasing thermal treatment time in the air. YiFei *et al.* [75] proposed that the thermal stability of BAM:Eu^{2+} was improved by substituting Si–N bonds in place of Al–O bonds in host lattice. Si–N doping showed increased emission intensity after heating at 600°C for 1 hour in air atmosphere. This increase in thermal stability

could be due to lower nitrogen electronegativity and stable local structure around Eu^{2+} ions. Wang *et al.* [76] explained the luminance degradation of BAM:Eu^{2+} due to baking at 600^{o}C. Reduction in lattice parameters was caused by dissolution of Si–N into BAM:Eu^{2+} lattice. Si–N codoping increased 110% for the pristine phosphors, under UV excitation. For the phosphors baked at 600 ^{o}C for 1 hour, the luminescent intensity increased by 122%, attributed to the lower nitrogen electronegativity and stable local structure around Eu^{2+}.

2.6. Gaps in the Study

From the literature survey it was observed that the synthesis approach to nano-scale BAM:Eu^{2+} ultra-fine powder of high luminous efficiency has not been achieved successfully.

- A simple synthesis technique to obtain pure BAM:Eu^{2+} phosphor with particle size in nanometer range is required.
- Effect of dopants on morphological and optical properties of BAM:Eu^{2+} phosphor needs to be studied in detail.
- Morphology control of combustion derived BAM:Eu^{2+} phosphor particles is still unclear.
- A detailed study related to the effect of alkali metal ions on morphological and photoluminescence properties of BAM:Eu^{2+} is required.
- BAM:Eu^{2+} with high luminescence efficiency and less degradation is desirable.

Considering these aspects, the following objectives were set for this work.

2.7. Objectives

1. Synthesis of BAM nanophosphor materials.

2. Doping of Eu^{2+} in the above material following combustion method.

3. To characterize the synthesized nanomaterials with X-ray diffraction (XRD), Transmission electron microscopy (TEM), and Scanning electron microscopy (SEM) for morphological studies and with UV-Visible spectroscopy and Photoluminescence spectroscopy (PL) for optical studies.

4. To study the luminescence properties of BAM and its substituted complexes.

References

[1] G. Blasse, B. Grabmaier, A general introduction to luminescent materials, in: Luminescent materials, Springer, 1994, pp. 1-9.

[2] P. Dorenbos, Energy of the first $4f^7 \rightarrow 4f^6 5d$ transition of Eu^{2+} in inorganic compounds, Journal of luminescence, 104 (2003) 239-260.

[3] D. Vollath, W.-V.V.G. KGaA, Co, An introduction to synthesis, properties and application, and Management, 7 (2008) 865-870.

[4] H. Terraschke, C. Wickleder, UV, blue, green, yellow, red, and small: newest developments on Eu^{2+}-doped nanophosphors, Chemical reviews, 115 (2015) 11352-11378.

[5] C. Ronda, Enlightenment on Luminescent Materials, in: Spectroscopy and Dynamics of Collective Excitations in Solids, Springer, 1997, pp. 339-373.

[6] J. Alarcon, D. Van der Voort, G. Blasse, Efficient Eu^{3+} luminescence in non-lanthanide host lattices, Materials Research Bulletin, 27 (1992) 467-472.

[7] S.T. Aruna, A.S. Mukasyan, Combustion synthesis and nanomaterials, Current opinion in solid state and materials science, 12 (2008) 44-50.

[8] T. Jüstel, H. Nikol, C. Ronda, New developments in the field of luminescent materials for lighting and displays, Angewandte Chemie International Edition, 37 (1998) 3084-3103.

[9] A. Srivastava, D. Doughty, W. Beers, Photon Cascade Luminescence of Pr^{3+} in $LaMgB_5O_{10}$, Journal of the Electrochemical Society, 143 (1996) 4113-4116.

[10] J. Felsche, The alkali problem in the crystal structure of beta alumina, Zeitschrift für Kristallographie-Crystalline Materials, 127 (1968) 94-100.

[11] J. Mahakhode, S. Dhoble, C. Joshi, S. Moharil, Combustion synthesis of phosphors for plasma display panels, Journal of alloys and compounds, 438 (2007) 293-297.

[12] K. Gedekar, S. Wankhede, S. Moharil, R. Belekar, Ce^{3+} and Eu^{2+} luminescence in calcium and strontium aluminates, Journal of Materials Science: Materials in Electronics, 29 (2018) 4466-4477.

[13] A. Verma, A. Verma, G. Bramhe, Shifting and enhanced photoluminescence performance of the $Sr_{1-x}Eu_xMgAl_{10}O_{17}$ phosphor, Journal of Alloys and Compounds, 774 (2019) 1168-1180.

[14] Z. Chen, Y. Yan, Morphology control and VUV photoluminescence characteristics of $BaMgAl_{10}O_{17}:Eu^{2+}$ phosphors, Physica B: Condensed Matter, 392 (2007) 1-6.

[15] Z. Chen, Y. Yan, Crystallinity and luminescent properties of citrate sol–gel derived BAM phosphor, Materials Letters, 61 (2007) 3927-3930.

[16] A. Zambare, C. Dighavkar, K. Murthy, Fluorescence Study of Sm Doped Barium Magnesium Aluminate Phosphor, (2011).

[17] N. Pradal, A. Potdevin, G. Chadeyron, R. Mahiou, Structural, morphological and optical investigations on $BaMgAl_{10}O_{17}:Eu^{2+}$ elaborated by a microwave induced solution combustion synthesis, Materials Research Bulletin, 46 (2011) 563-568.

[18] N.M. Sơn, P.N.T. Trang, Synthesis of $BaMgAl_{10}O_{17}:Eu^{2+}$ blue phosphor by combustion method, Hue University Journal of Science (HU JOS), 69 (2013).

[19] H. You, J. Zhang, G. Hong, H. Zhang, Luminescent properties of Mn^{2+} in hexagonal aluminates under ultraviolet and vacuum ultraviolet excitation, The Journal of Physical Chemistry C, 111 (2007) 10657-10661.

[20] B. Zhang, J.-W. Zhang, H. Zhong, L.-Y. Hao, X. Xu, S. Agathopoulos, C. Wang, L.-J. Yin, Highly stable modified phosphors of $Ba_2SiO_4:Eu^{2+}$ by forming a robust hydrophobic inorganic surface layer of silicon-oxy-imide-carbide, The Journal of Physical Chemistry C, 121 (2017) 11616-11622.

[21] W. Lü, Y. Luo, Z. Hao, X. Zhang, X. Wang, J. Zhang, Spectral tuning and energy transfer in a potential fluorescent lamp phosphor $BaMg_2Al_6Si_9O_{30}:Eu^{2+}$, Journal of luminescence, 132 (2012) 2439-2442.

[22] M. Li, X. Zhang, H. Zhang, W. Chen, L. Ma, X. Wang, Y. Liu, B. Lei, Highly efficient and dual broad emitting light convertor: an option for next-generation plant growth LEDs, Journal of Materials Chemistry C, 7 (2019) 3617-3622.

[23] H. Ni, H. Liang, Q. Su, Y. Tao, Y. Huang, Z. Gao, Luminescence and morphology of $BaMgAl_{10}O_{17}:Eu^{2+}$ phosphors prepared from different phases of Al_2O_3, Journal of the American Ceramic Society, 95 (2012) 3197-3201.

[24] W. Zhang, D. He, G. Ma, S. Cui, G. Li, H. Jiao, Low-temperature synthesis of $BaMgAl_{10}O_{17}:Eu^{2+}$ blue phosphors, Journal of Physics and Chemistry of Solids, 75 (2014) 163-167.

[25] D. Hou, C. Liu, X. Ding, X. Kuang, H. Liang, S. Sun, Y. Huang, Y. Tao, A high efficiency blue phosphor $BaCa_2MgSi_2O_8:Eu^{2+}$ under VUV and UV excitation, Journal of Materials Chemistry C, 1 (2013) 493-499.

[26] P. Zhu, W. Di, Q. Zhu, B. Chen, H. Zhu, H. Zhao, Y. Yang, X. Wang, Luminescent properties and thermal stability of $BaMgAl_{10}O_{17}:Eu^{2+}$ synthesized by sol–gel route, Journal of Alloys and Compounds, 454 (2008) 245-249.

[27] P. Zhu, Q. Zhu, H. Zhu, H. Zhao, B. Chen, Y. Zhang, X. Wang, W. Di, Effect of SiO_2 coating on photoluminescence and thermal stability of $BaMgAl_{10}O_{17}:Eu^{2+}$ under VUV and UV excitation, Optical Materials, 30 (2008) 930-934.

[28] L.-J. Yin, W.-J. Xie, M. Wang, W. Tian, S.-H. Zhang, Y.-L. Liang, M.-H. Lee, M.-z. Liu, X. Jian, L.-J. Deng, Insight into the evolution mechanism of carbon film and Eu valence in carbon coated $BaMgAl_{10}O_{17}:Eu^{2+}$ phosphor annealed in air, Ceramics International, 44 (2018) 8898-8903.

[29] H. Zhu, H. Yang, W. Fu, P. Zhu, M. Li, Y. Li, Y. Sui, S. Liu, G. Zou, The improvement of thermal stability of $BaMgAl_{10}O_{17}:Eu^{2+}$ coated with MgO, Materials Letters, 62 (2008) 784-786.

[30] K.-T. Kuo, S.-P. Lee, S.-Y. Chen, B.-M. Cheng, H.-C. Lu, D.-M. Liu, C.-C. Ting, $BaMgAl_{10}O_{17}:Eu$ blue phosphors with MgO coating and microwave irradiation, Journal of Physics and Chemistry of Solids, 69 (2008) 446-450.

[31] K.-T. Kuo, S.-P. Lee, S.-Y. Chen, B.-M. Cheng, H.-C. Lu, C.-C. Ting, Effect of microwave irradiation on surface characteristics and luminescent properties of $BaMgAl_{10}O_{17}:Eu$ blue phosphor, Journal of Physics and Chemistry of Solids, 69 (2008) 362-365.

[32] Z. Chen, Y. Yan, J.-M. Liu, Y. Yin, H. Wen, G. Liao, C. Wu, J. Zao, D. Liu, H. Tian, Microstructure and luminescence of surface-coated nano-$BaMgAl_{10}O_{17}:Eu^{2+}$ blue phosphor, Journal of Alloys and Compounds, 478 (2009) 679-683.

[33] Y.K. Jeong, H.-J. Kim, H.G. Kim, B.-H. Choi, Luminescent properties of $BaMgAl_{10}O_{17}:Eu^{2+}$ blue phosphor grown with SiO_2 using atomic layer deposition, Current Applied Physics, 9 (2009) S249-S251.

[34] J. Wang, G. Ning, W. Pan, X. Yang, Y. Lin, A novel route to $BaMgAl_{10}O_{17}:Eu$ blue phosphor by nano-coating method, Materials Science and Engineering: B, 147 (2008) 43-46.

[35] Z. Chen, Y. Yan, J. Liu, Y. Yin, H. Wen, J. Zao, D. Liu, H. Tian, C. Zhang, S. Li, Microwave induced solution combustion synthesis of nano-sized phosphors, Journal of Alloys and Compounds, 473 (2009) L13-L16.

[36] S.W. Ko, D. Shin, Morphology and luminescence properties of $BaMgAl_{10}O_{17}:Eu^{2+}$ blue phosphors by Aerosol Flame Deposition, Journal of electroceramics, 23 (2009) 410.

[37] H. Toyoshima, S. Watanabe, K. Ogasawara, H. Yoshida, First-principles calculations of 4f–5d optical absorption spectra in $BaMgAl_{10}O_{17}:Eu$, Journal of luminescence, 122 (2007) 104-106.

[38] H. Onuma, H. Tsuboi, M. Koyama, A. Endou, H. Takaba, M. Kubo, C.A. Del Carpio, P. Selvam, A. Miyamoto, Large-scale electronic structure calculation on blue phosphor $BaMgAl_{10}O_{17}:Eu^{2+}$ using tight-binding quantum chemistry method implemented for rare-earth elements, Japanese journal of applied physics, 46 (2007) 2534.

[39] K. Mishra, M. Raukas, A. Ellens, K. Johnson, A scattered wave model of electronic structure of Eu^{2+} in $BaMgAl_{10}O_{17}$ and associated excitation processes, Journal of luminescence, 96 (2002) 95-105.

[40] H. Kajiyama, H. Tanno, T. Shinoda, T. Fukasawa, R. Ramasamy, G. Shanmugavelayutham, T. Yasuda, 38.2: Lifetime Improvement of Eu-doped BAM by Plasma Treatment, in: SID Symposium Digest of Technical Papers, Wiley Online Library, 2007, pp. 1321-1324.

[41] R. Turos-Matysiak, M. Grinberg, J. Wang, W. Yen, R. Meltzer, Luminescence of BAM under high pressure: the Eu^{2+} sites, Journal of luminescence, 122 (2007) 107-109.

[42] Z.H. Zhang, Y.H. Wang, X.X. Li, Y.K. Du, W.J. Liu, Photoluminescence degradation and color shift studies of annealed $BaMgAl_{10}O_{17}:Eu^{2+}$ phosphor, Journal of luminescence, 122 (2007) 1003-1005.

[43] J. Lambert, G. Wallez, M. Quarton, T. Le Mercier, W. van Beek, Searching for the dopant ion in Eu^{2+}-activated $BaMgAl_{10}O_{17}$ phosphor with synchrotron diffraction, Journal of luminescence, 128 (2008) 366-372.

[44] P. Boolchand, K. Mishra, M. Raukas, A. Ellens, P. Schmidt, Occupancy and site distribution of europium in barium magnesium aluminate by ^{151}Eu Mössbauer spectroscopy, Physical Review B, 66 (2002) 134429.

[45] W. Lü, X. Zhang, Y. Wang, Z. Hao, Y. Liu, Y. Luo, X. Wang, J. Zhang, Luminescence investigation and thermal stability study of Eu^{2+} and Eu^{2+}–Mn^{2+} codoped (Ba, Sr)$Mg_2Al_6Si_9O_{30}$ phosphor, Journal of Alloys and Compounds, 513 (2012) 430-435.

[46] A. Jain, A. Kumar, S. Dhoble, D. Peshwe, Persistent luminescence: An insight, Renewable and Sustainable Energy Reviews, 65 (2016) 135-153.

[47] K. Binnemans, Lanthanide-based luminescent hybrid materials, Chemical reviews, 109 (2009) 4283-4374.

[48] W.-C. Ke, C.C. Lin, R.-S. Liu, M.-C. Kuo, Energy transfer and significant improvement moist stability of $BaMgAl_{10}O_{17}:Eu^{2+}$, Mn^{2+} as a phosphor for white light-emitting diodes, Journal of the Electrochemical Society, 157 (2010) J307-J309.

[49] Y. Linqin, P. Xingping, S. Zhang, W. Yuhua, W. Chang, Photoluminescence properties of Ca-doped $BaMgAl_{10}O_{17}:Eu^{2+}$, Mn^{2+} blue phosphor using BaF_2 and CaF_2 as co-flux, Journal of Rare Earths, 32 (2014) 1109-1113.

[50] Y. Xu, L. Wang, B. Qu, D. Li, J. Lu, R. Zhou, The role of co-dopants on the luminescent properties of α-$Al_2O_3:Mn^{4+}$ and $BaMgAl_{10}O_{17}:Mn^{4+}$, Journal of the American Ceramic Society, 102 (2019) 2737-2744.

[51] J. Zhang, Z. Zhang, Z. Tang, Y. Tao, X. Long, Luminescent properties of the $BaMgAl_{10}O_{17}:Eu^{2+}$, M^{3+} (M= Nd, Er) phosphor in the VUV region, Chemistry of materials, 14 (2002) 3005-3008.

[52] V. Singh, N. Singh, M. Pathak, S. Watanabe, T.G. Rao, N.A. Jadhav, Y.-W. Kwon, PL and ESR Study on UVB-Emitting Gadolinium-Doped $BaMgAl_{10}O_{17}$ Hexagonal Phase Obtained by Combustion Synthesis, Journal of Electronic Materials, 47 (2018) 7365-7371.

[53] S. Tigga, N. Brahme, D. Bisen, Investigations on luminescence behaviour of Ce-activated $BaMgAl_{10}O_{17}$ phosphor, Luminescence, 31 (2016) 1306-1312.

[54] J.S. Cho, D.S. Jung, S.H. Lee, Y.C. Kang, Morphological and optical characteristics of $BaMg_{0.9}Al_{10}O_{19}:Mn^{2+}$ phosphor powders prepared by flame spray pyrolysis, Journal of Ceramic Processing Research, 9 (2008) 83.

[55] R. Shrivastava, J. Kaur, Studies on long lasting optical properties of Eu^{2+} and Dy^{3+} doped di-barium magnesium silicate phosphors, Chinese Chemical Letters, 26 (2015) 1187-1190.

[56] W. Lü, Z. Hao, X. Zhang, Y. Luo, X. Wang, J. Zhang, Tunable full-color emitting $BaMg_2Al_6Si_9O_{30}:Eu^{2+}$, Tb^{3+}, Mn^{2+} phosphors based on energy transfer, Inorganic chemistry, 50 (2011) 7846-7851.

[57] A. Yerpude, S. Dhoble, Luminescent properties of Eu^{2+} and Dy^{3+} ions in $Ba_4Al_2O_7$ phosphor for solid state lighting, Journal of luminescence, 132 (2012) 1781-1785.

[58] A. Yerpude, S. Dhoble, Synthesis and photoluminescence properties of Dy^{3+}, Sm^{3+} activated $Sr_5SiO_4Cl_6$ phosphor, Journal of luminescence, 132 (2012) 2975-2978.

[59] V. Pawade, S. Dhoble, Trap depth and Dy^{3+} luminescence in $BaAl_2Si_2O_8$ phosphor, Journal of luminescence, 145 (2014) 626-630.

[60] W. Wang, B. Liu, Y. Wang, Z. Zhang, Y. Chen, L. Wei, Morphology control and photoluminescence of $BaMgAl_{10}O_{17}:Eu^{2+},Mn^{2+}$ phosphors prepared by flux method, Materials Letters, 65 (2011) 3580-3582.

[61] R. Rao, Morphology and stability of flux grown blue emitting BAM phosphors for plasma display panels applications, Journal of the Electrochemical Society, 152 (2005) H115-H119.

[62] Y. Zhu, G. Zheng, X. Xin, R. Zhuang, L. Zhang, Strong luminescence enhancement of Li doped Y_2O_3:5%Eu^{3+} phosphors, Journal of Materials Science: Materials in Electronics, 28 (2017) 1485-1488.

[63] N. Dhananjaya, H. Nagabhushana, B. Nagabhushana, B. Rudraswamy, C. Shivakumara, K. Narahari, R. Chakradhar, Enhanced photoluminescence of $Gd_2O_3:Eu^{3+}$ nanophosphors with alkali (M= Li^+, Na^+, K^+) metal ion co-doping, Spectrochimica Acta Part A: Molecular and Biomolecular Spectroscopy, 86 (2012) 8-14.

[64] Y. Zhou, J. Lin, Morphology control and luminescence properties of $BaMgAl_{10}O_{17}:Eu^{2+}$ phosphors prepared by spray pyrolysis, Journal of Solid State Chemistry, 178 (2005) 441-447.

[65] Z.H. Zhang, L. Chen, Q.H. Gan, Q. Tian, C.L. Chen, Z.L. Huang, Morphology and luminescent properties of $BaMgAl_{10}O_{17}:Eu^{2+}$ phosphor synthesized by a hydrothermal homogeneous precipitation method, physica status solidi (a), 210 (2013) 378-382.

[66] Y. Yang, X. Li, W. Feng, W. Yang, W. Li, C. Tao, Effect of surfactants on morphology and luminescent properties of $CaMoO_4:Eu^{3+}$ red phosphors, Journal of Alloys and Compounds, 509 (2011) 845-848.

[67] J.R. Sohn, Y.C. Kang, H.D. Park, Morphological control of Y_2O_3:Eu phosphor particles by adding polymeric precursors in spray pyrolysis, Japanese journal of applied physics, 41 (2002) 3006.

[68] D. Kumar, M. Sharma, O. Pandey, Morphology controlled $Y_2O_3:Eu^{3+}$ nanophosphors with enhanced photoluminescence properties, Journal of luminescence, 158 (2015) 268-274.

[69] N. Pradal, G. Chadeyron, S. Thérias, A. Potdevin, C.V. Santilli, R. Mahiou, Investigation on combustion derived $BaMgAl_{10}O_{17}:Eu^{2+}$ phosphor powder and its corresponding PVP/$BaMgAl_{10}O_{17}:Eu^{2+}$ nanocomposite, Dalton Transactions, 43 (2014) 1072-1081.

[70] B. Moine, G. Bizarri, Rare-earth doped phosphors: oldies or goldies?, Materials Science and Engineering: B, 105 (2003) 2-7.

[71] C. Okazaki, Thermal degradation of PDP blue phosphor in paste baking process, Proc. of IDW'00, (2000).

[72] G. Bizarri, B. Moine, On $BaMgAl_{10}O_{17}:Eu^{2+}$ phosphor degradation mechanism: thermal treatment effects, Journal of luminescence, 113 (2005) 199-213.

[73] S. Zhang, Y. Hou, H. Fujii, T. Onishi, M. Kokubu, M. Obata, H. Tanno, T. Kono, H. Uchiike, Effect of nonstoichiometry on the deterioration of Eu^{2+}-doped hexagonal aluminate

phosphor for plasma display applications, Japanese journal of applied physics, 42 (2003) 477.

[74] K. Yokota, S.-X. Zhang, K. Kimura, A. Sakamoto, Eu^{2+}-activated barium magnesium aluminate phosphor for plasma displays–Phase relation and mechanism of thermal degradation, Journal of luminescence, 92 (2001) 223-227.

[75] W. YiFei, X. Xin, Q. Han, Y. Liangjun, H. Luyuan, Optimization of $BaMgAl_{10}O_{17}:Eu^{2+}$ phosphors by the substitution of Si-N bonds for Al-O bonds, Journal of Rare Earths, 28 (2010) 281-284.

[76] Y. Wang, X. Xu, L. Yin, L. Hao, High thermal stability and photoluminescence of Si–N-codoped $BaMgAl_{10}O_{17}:Eu^{2+}$ phosphors, Journal of the American Ceramic Society, 93 (2010) 1534-1536.

CHAPTER 3

EXPERIMENTAL TECHNIQUES

Overview

The experimental detail followed for the preparation of the phosphors and their characterization is presented herewith in this chapter. The BAM:Eu^{2+} phosphors were prepared using solution combustion synthesis method (SCS). Complete procedure along with different molar concentrations of different dopants, co-dopants and capping agents has been given. The details of the various characterization techniques adopted to characterize the prepared samples has been given in terms of the instrument names, their model number, working and operating conditions. Name of the samples prepared and their sample codes are given in tabulated form. Whole scheme of events leading to successful completion of the experimental work as conclusion is presented in a flowchart to have more visibility.

3.1. Raw Materials

In present study, raw materials used for the preparation of samples were Barium Nitrate ($Ba(NO_3)_2$, 99%, HiMedia); Magnesium Nitrate ($Mg(NO_3)_2.6H_2O$, 99%, HiMedia); Aluminium Nitrate ($Al(NO_3)_3.9H_2O$,98%, HiMedia); Europium Nitrate ($Eu(NO_3)_3.6H_2O$, 99.9% Alfa Aesar); Dysprosium Nitrate ($Dy(NO_3)_3.5H_2O$, 99.9%, Alfa Aesar); Lithium Nitrate ($LiNO_3$, 99.99%, Sigma Aldrich); Sodium Nitrate ($NaNO_3$, 99.99%, Sigma Aldrich); Potassium Nitrate (KNO_3, 99.99%, Sigma Aldrich); Calcium Nitrate ($Ca(NO_3)_2.4H_2O$, 99%, Himedia); β-cyclodextrin (β-CD, 98%, HiMedia); Thioglycerol (TG, 99%, Sigma Aldrich); Urea (CH_4N_2O, 99%, HiMedia); Nitric Acid (HNo_3, 69%, Loba Chemie); Ethanol (Merck) and double distilled water. All these materials were used without any further purification.

3.2. Sample Preparation

Phosphor samples were prepared by solution combustion synthesis (SCS) method. For any combustion to take place oxidizer and fuel are required. In the present work, metal nitrates were used as oxidizers and urea as fuel. The stoichiometry of oxidizer and fuel is determined by oxidizer to fuel ratio (O/F ratio) and expressed by elemental stoichiometry coefficient (Φ_e) as given in equation (3.1)

$$\boldsymbol{\Phi_e} = \frac{\Sigma(\boldsymbol{coefficient\ of\ oxidising\ elements\ in\ specific\ formula})\ \boldsymbol{X\ valency}}{(-)\Sigma(\boldsymbol{coefficient\ of\ reducing\ elements\ in\ specific\ formula})\ \boldsymbol{X\ valency}} \quad (3.1)$$

The mixture is stoichiometric with a maximum heat of combustion at $\Phi_e = 1$ [1]. The stoichiometric ratio of oxidizer to fuel was calculated based upon propellant chemistry, where reducing elements have positive valencies whereas oxidizing elements have negative valencies. Metals are considered as reducing elements hence positive valency of the metal in that compound is considered. Valency of elements C and H is taken as 4+ and 1+ respectively, oxygen is considered as an oxidizer with valency 2- and valency of nitrogen is taken as zero as it converts to molecular nitrogen during combustion [2]. Therefore, reducing and oxidizing valencies for $M(NO_3)_2$, $M(NO_3)_3$ and urea (CH_4N_2O) was calculated as follows:

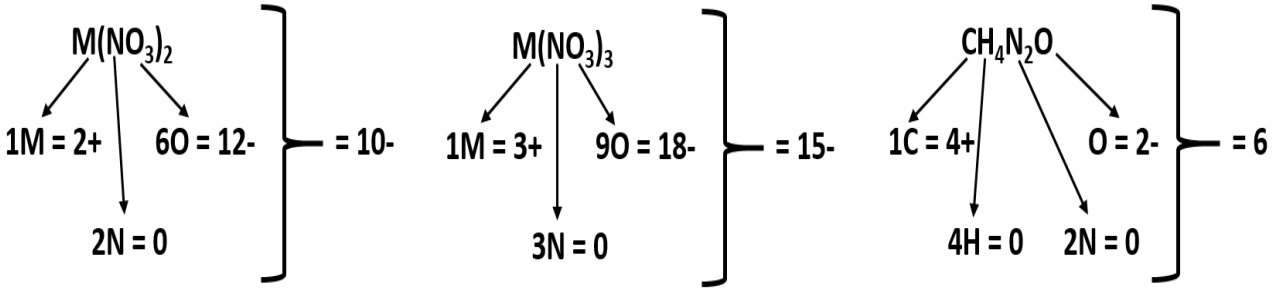

Accordingly, the mol ratio for $M(NO_3)_2$: urea is 10/6 and for $M(NO_3)_3$: urea is 15/6. Hence, the amount of urea required for the formation of $Ba_{0.9}MgAl_{10}O_{17}:Eu_{0.1}$ through combustion was calculated as

(0.9 x (10/6)) + (10/6) + (10 x (15/6)) + (0.1 x (15/6)) = 28.42

Thus, the chemical equation for the reaction is

$0.9Ba(NO_3)_2 + 0.1Eu(NO_3)_3 + Mg(NO_3)_2 + 10Al(NO_3)_3 + 28.42CH_4N_2O \rightarrow Ba_{0.9}MgAl_{10}O_{17}:Eu_{0.1}$ + by products (3.2)

The samples were prepared according to the formula $Ba_{(1-x)}MgAl_{10}O_{17}:Eu_x$. Various compositions prepared with their labels are given in table 3.1. The required quantity of raw materials was taken as per the stoichiometry ratio.

Table 3.1: Prepared samples with their sample codes

S.No.	Sample Name	Concentration (mol %)	Sample Code
1.	BAM:Eu^{2+} (Combusted)	Eu (10)	C
2.	BAM:Eu^{2+} (Combusted + Annealed)	Eu (10)	CA
3.	BAM:Eu^{2+} (Combusted + Acid Leached)	Eu (10)	CL
4.	BAM:Eu^{2+} (Combusted+ Acid Leached + Annealed)	Eu (10)	E10
5.	BAM:Eu^{2+}/Dy^{3+}	Eu (10) / Dy (0.5, 1, 2, 3, 4)	ED0.5, ED1, ED2, ED3, ED4
6.	BAM:Eu^{2+}/Li^{+}	Eu (10) / Li (0.005, 0.01, 0.02, 0.03)	EL05, EL1, EL2, EL3
7.	BAM:Eu^{2+}/Na^{+}	Eu (10) / Na (0.01, 0.02, 0.03, 0.04)	EN1, EN2, EN3, EN4
8.	BAM:Eu^{2+}/K^{+}	Eu(10) / K (0.01, 0.02, 0.03, 0.04)	EK1, EK2, EK3, EK4
9.	BAM:Eu^{2+}/β-CD	Eu (10) / β-CD (0.001, 0.003, 0.005, 0.007)	ECD1, ECD3, ECD5, ECD7
10.	BAM:Eu^{2+}/TG	Eu (10) / TG (0.01, 0.02, 0.04, 0.06)	ETG1, ETG2, ETG4, ETG6
11.	CaBAM:Eu^{2+}	Eu (10) / Ca (2, 4, 6, 8)	EC2, EC4, EC6, EC8

The sample synthesis comprised of three steps.

Step I : Combustion

The stoichiometric amount of the required nitrates and urea were taken. The chemiclas were weighed on the digital (Sartorius make) weighing balance. The reagents were dissolved in minimum amount (11 ml) of distilled water in a beaker with continuous stirring at 60℃ for approximately an hour resulting in a clear transparent solution. This solution was then transferred to a silica crucible and was placed in a furnace preheated and maintained at 550℃ ± 5℃. Solution upon heating; boiled, foamed and combusted into flames liberating large amount

of gases like NH_3 and NO_2. The process was highly exothermic and the flame persisted for about 30 seconds. Combustion resulted in white voluminous ash. The crucible was then removed from the furnace and obtained white foamy ash was physically crushed into a fine powder.

Step II : Acid Leaching

The obtained white powder was acid leached to achieve monophasic phosphor powder by the removal of the impure phase during leaching. For acid leaching a solution of HNO_3 and distilled water with pH ≈ 2 was prepared. The pH of the solution was measured with pH meter (EUTECH, CyberScan pH Tutor meter). The white powder obtained after combustion was placed in a funnel lined with Whatman-40 filter paper and was washed several times with acid solution of pH ≈ 2 followed by a final wash with ethanol.

Step III : Annealing

The wet powder obtained after acid leaching was dried in an oven at 60 ℃ for 24 hours. The dried powder was then annealed in an argon atmosphere at 600 ℃ for 4 hours. The powders obtained after annealing were the final samples. The complete synthesis process is depicted by a flow chart given in figure 3.1.

To study the thermal stability of the phosphors, the prepared samples were heated at 600°C for 30 minutes in ambient air.

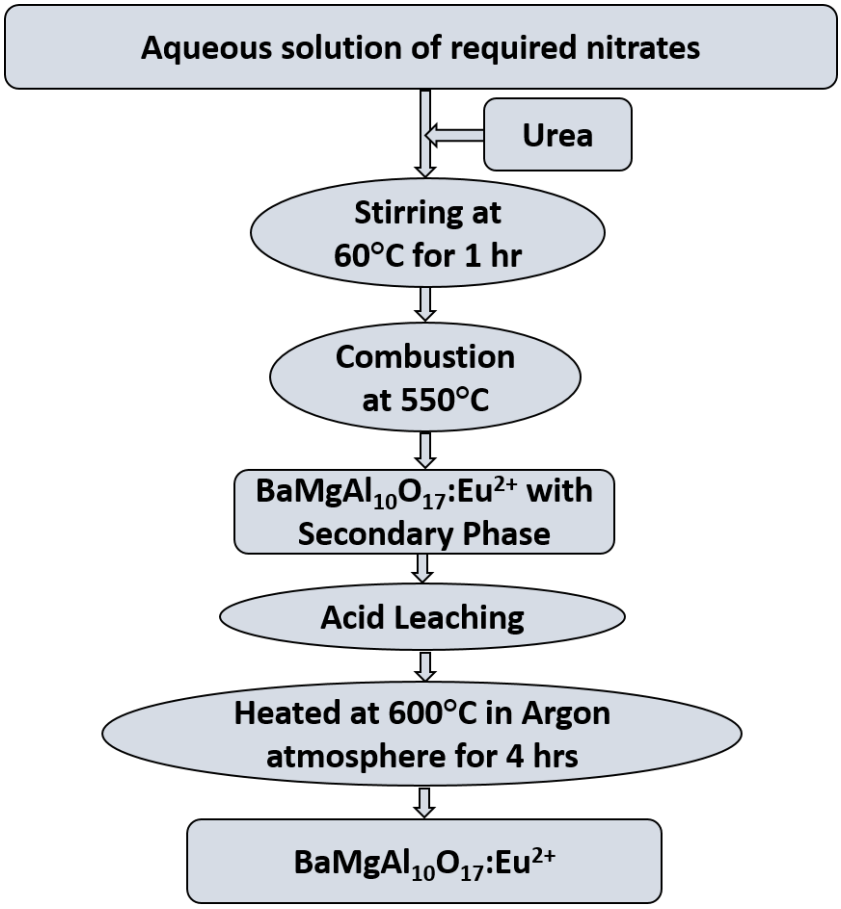

Figure 3.1: Flowchart depicting synthesis scheme of $BaMgAl_{10}O_{17}:Eu^{2+}$ phosphors

3.3. Characterization Techniques

The as prepared phosphor powders were characterized using various instruments and techniques to study their morphological and optical properties.

3.3.1. Phase Analysis

The information about the crystalline phase of BAM:Eu^{2+} phosphors was revealed by the X-ray diffraction (XRD) characterization technique. The XRD patterns of the prepared samples were recorded at room temperature using PANalytical X'pert Pro X-ray Diffractometer with Ni filtered Cu Kα radiation in the Bragg's angle range of $15^{o} \leq 2\theta \leq 70^{o}$. The obtained data from the XRD was indexed using standard powder diffraction files issued by International Centre for Diffraction Data (ICDD).

3.3.2. Structural and Morphological Study

The morphological properties of the prepared samples was studied using field emission scanning electron microscopy (FESEM) and transmission electron microscopy (TEM).

3.3.2.1. Field Emission Scanning Electron Microscopy

The morphological features of the particle surface were visualized with field emission scanning electron microscope (FESEM) which uses a high-energy electron beam. Therefore, the material should be conductive for the current. So, a thin layer of gold was sputtered on the sample material and was then kept in the sample holder. FESEM images for the samples were recorded on Hitachi SU8010 FESEM.

3.3.2.2. Transmission Electron Microscopy

Transmission electron microscope (TEM) is used to study the structural features of the samples. A high-energy beam of electrons is transmitted through a thin layer of the sample and the interactions between the electrons and the atoms of the sample are used to record the TEM images. As a thin layer of sample is required for TEM analysis. For it, the prepared sample powder was dispersed in ethanol followed by ultra-sonication for 15 minutes. Then a drop of the liquid containing dispersed particles was put on a carbon-coated Cu grid. After a few minutes ethanol evaporated and the grid, containing sample was then mounted inside the sample holder. For the present samples, TEM images were taken from Tecnai G2 20 TEM.

3.3.2.3. Fourier Transform Infrared Spectroscopy

Fourier transform infrared spectroscopy (FTIR) is an analytical technique used to study the inorganic, polymeric, and organic materials. It also probes the bonds of the sample. It uses infrared (IR) radiation to test the sample. When IR radiation is passed through the sample, some of the radiation is transmitted and some radiation is absorbed by the sample. The wavelength of light absorbed is the characteristic of the chemical bond. The resulting spectrum thus gives a molecular fingerprint of the sample. For the synthesized samples Perkin Elmer – Spectrum RX – IFTIR instrument in the wavenumber range 4000 cm^{-1} – 400 cm^{-1} was used to record FTIR spectra at room temperature.

3.3.3. Optical Study

3.3.3.1. UV-Visible Spectroscopy

Ultraviolet-visible spectroscopy (UV-Vis) is used to measure the reflection, transmission, and absorption of ultraviolet and visible light by a sample. It uses light in visible region and adjacent range (near UV (NUV) and near-infrared (NIR)). The UV region ranges from 190 nm to 400 nm whereas; visible region is in the range of 400 nm to 800 nm. In present work, optical reflectance spectra of the prepared samples were recorded at room temperature using Perkin Elmer lambda 950 UV-VIS-NIR spectrophotometer in the wavelength range 200 nm to 700 nm.

3.3.3.2. Photoluminescence Spectroscopy

Electronic structure of a material is probed by photoluminescence spectroscopy (PL). When light is incident on the sample, it gets absorbed by the sample. Thereafter, the material gets excited to a higher electronic state where it relaxes releasing the excess of energy in the form of photons and returns to a lower energy level. Emission of photons through this process is photoluminescence. The energy of this emitted light corresponds to the energy difference between equilibrium state and excited state involved in an electronic transition. The quantity of emitted light is decided by the relative contribution of this radiative process. The PL spectra and calculation of Commission Internationale de l'Eclairage (CIE) color coordinates of the synthesized phosphors prepared in the present work were recorded through Agilent technologies spectrometer, Model Cary Eclipse equipped with Xenon lamp. Slit width for all the photoluminescence measurements was kept at 2.5 nm. All the measurements were performed at room temperature.

3.3.3.3. Thermoluminescence Spectroscopy

Thermoluminescence is a form of luminescence in which light emission is caused by moderate heating of the material previously exposed to some ionizing radiation or UV rays. Electrons after absorbing energy from UV rays or ionizing radiation (alpha, beta, gamma or cosmic rays) become free and move in the crystal lattice. Some of the electrons get trapped in the crystal lattice imperfections. Upon heating of the crystal, these trapped electrons are released with associated light emission and this emission is recorded as TL spectra. TL spectrum is an intensity vs temperature curve and is called a glow curve. Intensity of the glow curve is

related to the activation energy of the trap level and thus, trap depth can be determined. For the samples in the present study, the TL spectra were recorded through Harshaw Q TLD reader 3500 model. Linear heating rate of 5°C s^{-1} was used. The samples were irradiated by gamma radiation from Co-60 source in Gamma chamber GC – 1200, at Inter University Accelerator Center (IUAC), New Delhi, India.

References

[1] M. Lackner, Combustion synthesis: novel routes to novel materials, Bentham Science Publishers, 2010.
[2] S. Ekambaram, K. Patil, M. Maaza, Synthesis of lamp phosphors: facile combustion approach, Journal of Alloys and Compounds, 393 (2005) 81-92.

CHAPTER 4

RESULTS AND DISCUSSION-I

Overview

This chapter discusses the structural and optical properties of $BaMgAl_{10}O_{17}:Eu^{2+}$ ($BAM:Eu^{2+}$) nanophosphors and also the effect of pure phase on the structural and luminescence properties of $BAM:Eu^{2+}$ nanophosphors. In this chapter, major focus is on the procurement of pure phase of $BAM:Eu^{2+}$ nanophosphor synthesized by SCS technique. For this, the synthesized samples prepared by combustion synthesis were post treated through acid leaching and annealing. The role of acid leaching and annealing in obtaining the pure phase of $BAM:Eu^{2+}$ nanophosphor was studied. The structural, morphological and optical properties of the samples were investigated using X-ray diffraction (XRD), field emission scanning electron microscopy (FESEM), transmission electron microscopy (TEM), Fourier transform infrared spectroscopy (FTIR), and photoluminescence spectroscopy (PL).

4.1. Structural and Optical Properties of BAM:Eu^{2+}

BAM:Eu^{2+} nanophosphors were prepared by SCS method. The details of synthesis route has been described in previous chapter (section 3.2). The molar concentration of Europium was varied from 4 mol% to 11 mol%. The effect of europium ion on the structural and optical properties of BAM was studied. The results of the characterized samples are presented below.

4.1.1. XRD Study

Existence of different phases in the prepared samples was identified through XRD study. XRD patterns of BAM:Eu^{2+} with concentration of Eu^{2+} ions varying from 4 mol% to 11 mol% are given in figure 4.1 (a, b, c, d & e). The peaks are labeled with their corresponding (hkl) values. The peaks were identified and indexed as per JCPDS card no. 00-026-0163. All the peaks matched well with JCPDS card no. 00-026-0163 confirming hexagonal β-alumina structure with P 63/m m c space group. No secondary peak was observed confirming pure phase formation. Absence of any additional peak due to dopant ion suggested well incorporation of dopant ion in the host lattice. Doping of Eu^{2+} ion did not induce any notable change in the crystal structure. The average crystallite size was estimated using Debye-Scherrer equation [1] from the three most intense peaks corresponding to planes (110), (107) and (114). The average crystallite size was around 65 nm for all the prepared samples suggesting that the crystallite size was not disturbed by the insertion of Eu^{2+} ions in the BAM lattice.

4.1.2. FTIR Study

Figure 4.2 exhibits the FTIR spectrum of the sample BAM:Eu^{2+} (10 mol%). The broad peak observed at 3445 cm^{-1} is due to the O-H stretching vibration indicating the presence of adsorbed water. The peaks at 1638 cm^{-1} and 1407 cm^{-1} are the nitrate stretching frequencies as nitrate precursors were used for the synthesis of the samples [2]. The IR region ranging from 1000 cm^{-1} – 400 cm^{-1} corresponds to the metal – oxygen stretching frequencies [3]. BAM:Eu^{2+} has β-alumina structure which consist of spinel block $MgAl_{10}O_{16}$ composed of AlO_4 tetrahedrons and AlO_6 octahedrons [4]. The peaks obtained at 1004 cm^{-1} and 556 cm^{-1} are due to AlO_6 aluminate group whereas the peaks at 772 cm^{-1} and 704 cm^{-1} are of AlO_4 aluminate group. A small peak obtained at 662 cm^{-1} corresponds to Al – O vibrations [5, 6].

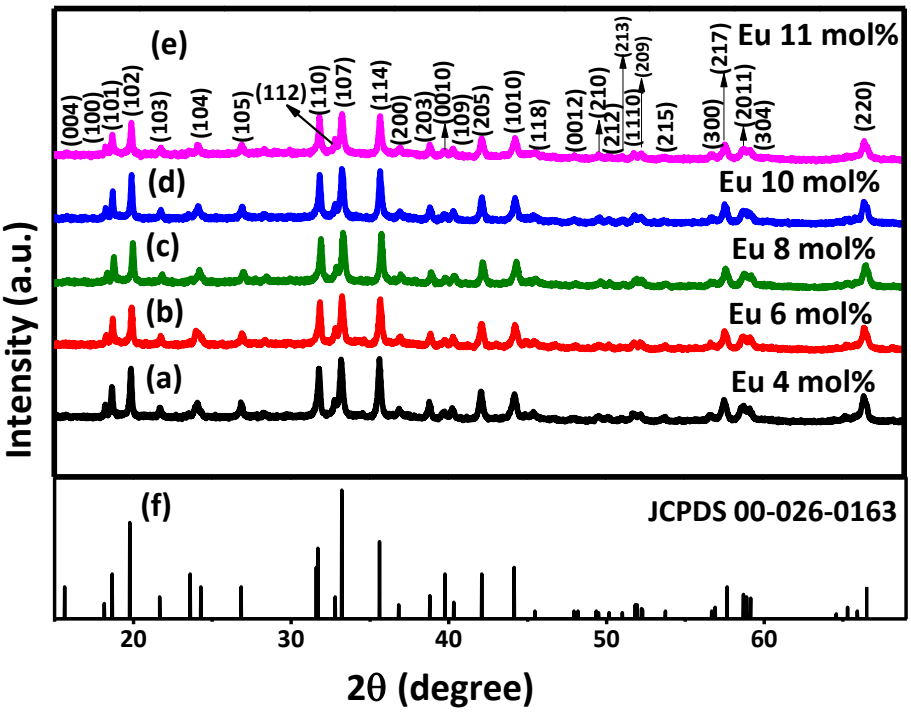

Figure 4.1: XRD pattern of **(a, b, c, d & e)** BAM:Eu^{2+} with concentration of Eu^{2+} varying from 4 mol% to 11 mol% and compared with **(f)** JCPDS card no. 00-026-0163

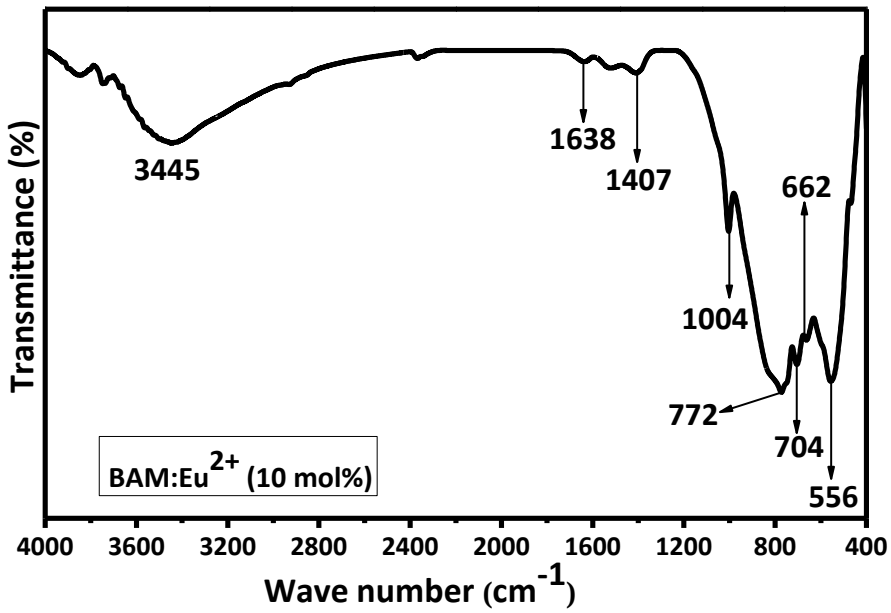

Figure 4.2: FTIR spectrum for BAM:Eu^{2+} (10 mol%)

4.1.3. UV-Visible Spectroscopic Analysis

The bandgap has been calculated using Kubelka-Munk method which is given by the following equation [7, 8]

$$\boldsymbol{F(R) = \frac{(1-R)^{1/n}}{2R}} \quad (4.1)$$

where F(R) is Kubelka-Munk function and R is absolute reflectance of the sample. The value of n depends upon the type of transition. Transitions can be of four types namely, allowed direct, allowed indirect, forbidden direct and forbidden indirect corresponding to values ½, 2, 3/2 and 3 respectively. Figure 4.3 shows the plot of $[h\upsilon F(R)]^2$ versus photon energy ($h\upsilon$) for BAM:Eu^{2+} (10 mol%). The value of bandgap was determined by extrapolating the rising part of Kubelka-Munk plot to abscissa at zero. The bandgap energy value for BAM:Eu^{2+} (10 mol%) was found to be 5.3 eV.

4.1.4. Photoluminescence Study

Photoluminescence excitation and emission spectra for BAM:Eu^{2+} with varying concentration of Eu^{2+} are depicted in figure 4.4 (a & b). Photoluminescence excitation spectra monitored at 450 nm, absorbed in the wavelength range from 280 nm to 420 nm with maximum absorption at approximately 330 nm is shown in figure 4.4 (a). This wide range of absorption gave a broad excitation band corresponding to $4f^7$-$4f^6 5d^1$ transition of Eu^{2+} ion. The photoluminescence emission spectra in figure 4.4 (b) recorded at 330 nm excitation wavelength illustrated several broad bands covering the spectral range from 400 nm to 540 nm for varying concentration of Eu^{2+} ions. The broad bands obtained from $4f^6 5d^1$-$4f^7$ transition of Eu^{2+} ion peak at 450 nm ascribe blue color to the nanophosphor. The varying concentration of Eu^{2+} ions did not change the maxima peak location at 450 nm. The maximum photoluminescence intensity was obtained for 10 mol% Eu^{2+} ion concentration. The photoluminescence intensity increased with the increase in Eu^{2+} ion concentration till 10 mol% Eu^{2+} ion concentration. After this, the increase in ion concentration decreased the photoluminescence intensity due to concentration quenching [9].

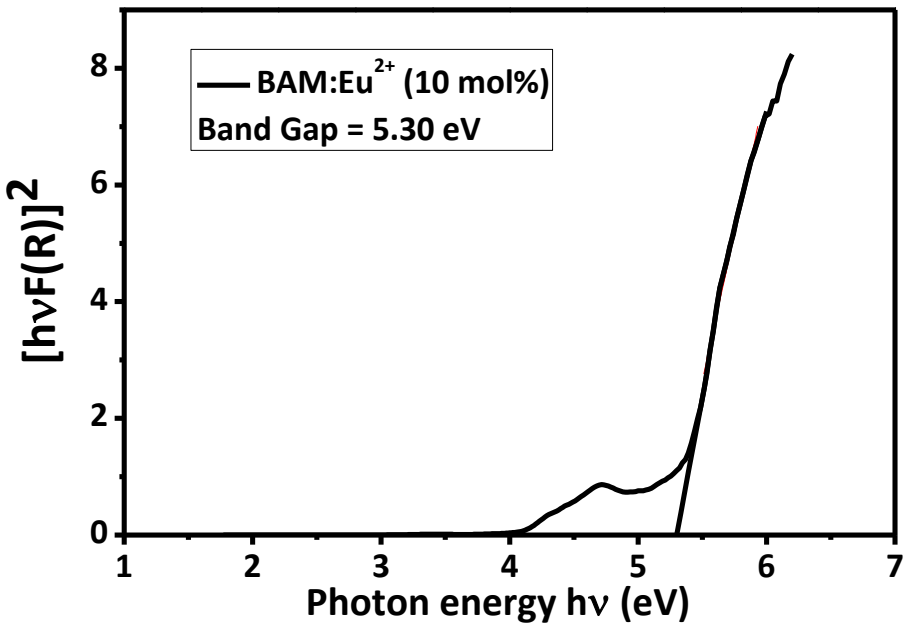

Figure 4.3: Kubelka-Munk plot for band gap calculation of sample BAM:Eu^{2+} (10 mol%)

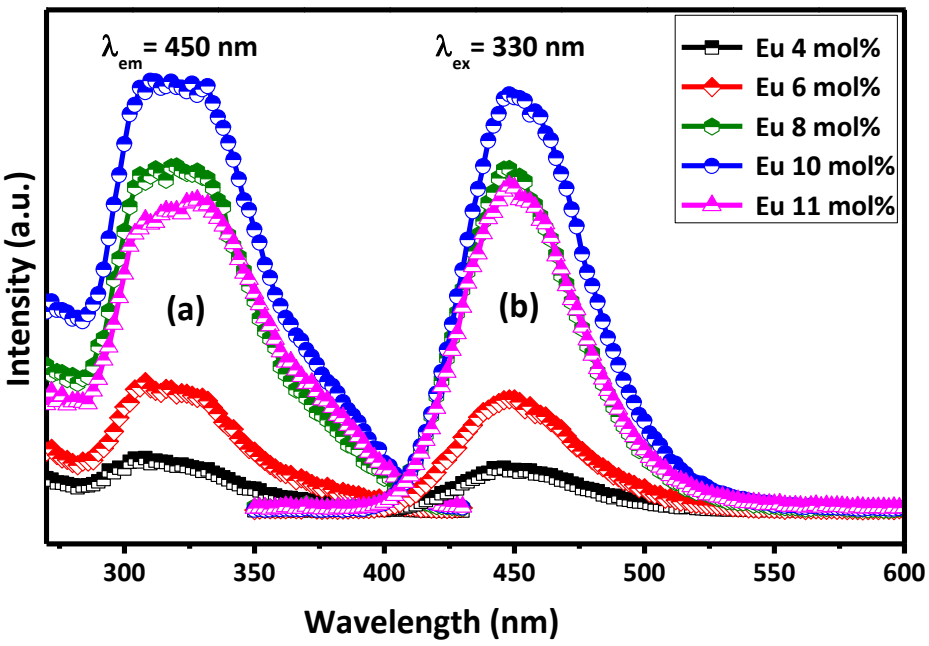

Figure 4.4: Photoluminescence **(a)** excitation spectra **(b)** emission spectra for BAM:$Eu^{2+}$with varying concentration of Eu^{2+} ion

4.2. Effect of Pure Phase on Optical Properties of BAM:Eu^{2+}

Phase purity is an essential parameter required for high luminescence intensity of a phosphor. Small particle size with narrow particle distribution, phase purity and uniform morphology are effective in the enhancement of luminescence efficiency [10]. The luminescence efficiency of phosphor is highly dependent upon purity of phase. The present section studies how the pure phase affected the luminescence properties of BAM:Eu^{2+}. To procure pure BAM:Eu^{2+} phase, the additional steps of acid leaching and annealing after combustion were performed as already mentioned in chapter 3 (Experimental techniques (section 3.2)). For simplification, a brief description is given below. The synthesized combusted powder (C) was treated in three different ways.

1. The combusted powder (C) annealed at 600°C for 4 hours in argon atmosphere, was named CA.
2. The combusted powder (C) acid leached with nitric acid (pH ≈ 2) followed by ethanol washing and dried in an oven at 60°C for 24 hours, was named CL.
3. The combusted powder (C), acid leached as mentioned above in point no. 2 and annealed at 600°C for 4 hours in argon atmosphere, was named E10.

Details of the prepared samples are tabulated in table 4.1.

Table 4.1: Samples with their corresponding name

S.No.	Sample	Sample Name
1.	BAM:Eu^{2+} (Combusted)	C
2.	BAM:Eu^{2+} (Combusted + Annealed)	CA
3.	BAM:Eu^{2+} (Combusted + Acid Leached)	CL
4.	BAM:Eu^{2+} (Combusted+ Acid Leached + Annealed)	E10

The prepared samples were studied for their structural and optical properties.

4.2.1. XRD Study

Figure 4.5 (a, b, c & d) shows the XRD patterns of combusted and treated samples. The XRD patterns were indexed according to the JCPDS card no. 00-026-0163. Additional peaks at

(2θ) 28° and 34.3° corresponding to the secondary phase $BaAl_2O_4$ [JCPDS card no. 01-082-2001] were observed for samples C and CA (figure 4.5 (a & b)). For the sample CA, where the combusted sample was only annealed without acid leaching, the additional peaks corresponding to $BaAl_2O_4$ phase became more sharp and intense indicating an increasing effect of impure phase. As reported in literature [11], $BaAl_2O_4:Eu^{2+}$ gives bluish green emission at 500 nm, negatively affecting the luminescence emission of $BAM:Eu^{2+}$. Therefore, to obtain good photoluminescence efficiency for $BAM:Eu^{2+}$, it becomes quite essential to eliminate the impure phase. The additional peaks of $BaAl_2O_4$ phase disappear from the acid leached sample CL as seen in figure 4.5(c). The disappearance of $BaAl_2O_4$ phase was due to the transformation of $BaAl_2O_4$ to $Ba(NO_3)_2$ in the presence of water and to γ-alumina in the presence of HNO_3 [12]. Hence, this secondary phase was eliminated after acid wash. Figure 4.5(d) also illustrates that $BaAl_2O_4$ phase does not reappear upon annealing the acid washed sample. Instead, more intense and sharp peaks of BAM were obtained. As annealing after combustion did not affect the phase purity, so our study incorporates three samples, namely, C, CL and E10.

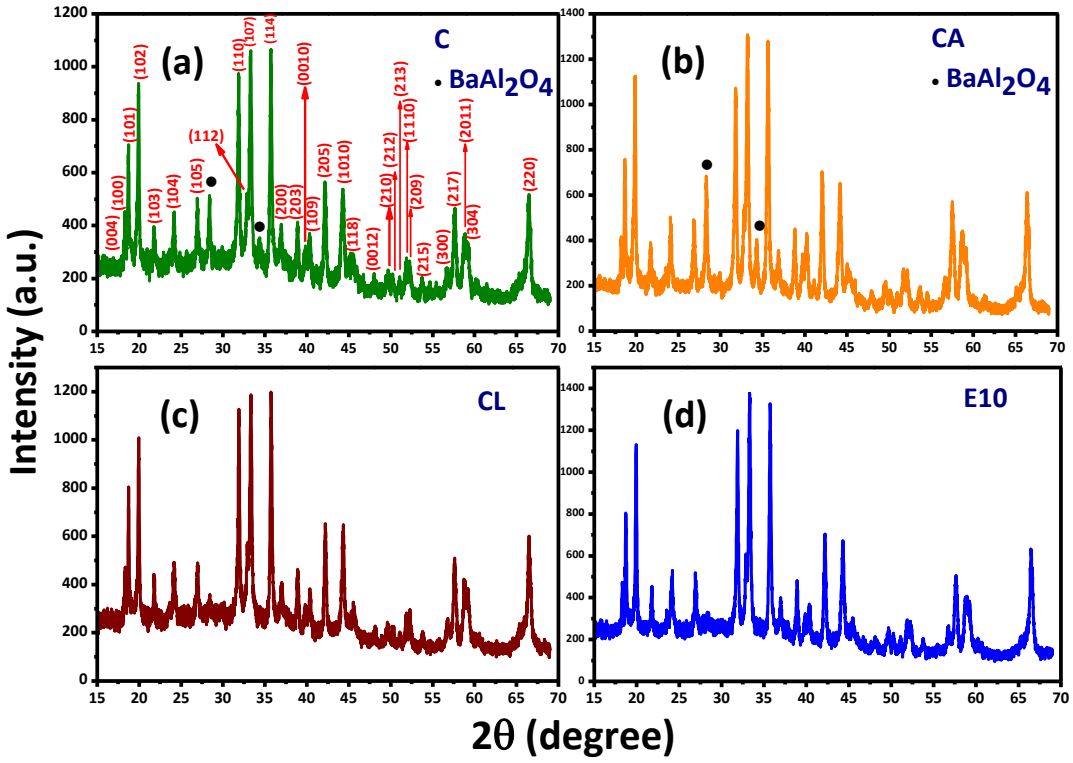

Figure 4.5: XRD pattern for $BAM:Eu^{2+}$ **(a)** combusted (C) **(b)** combusted and annealed (CA) **(c)** combusted and acid leached (CL) **(d)** combusted, acid leached and annealed (E10)

To further study the effect of acid leaching and annealing on XRD, the highest intensity peak corresponding to plane (107) for the three samples was studied. The peak parameters are tabulated in table 4.2.

Table 4.2: Peak parameters for highest intense peak corresponding to plane (107) (scanned at same XRD parameters)

Sample Name	Peak Intensity (a.u.)	FWHM (degree)	Crystallite size (nm)
C	1068.60	0.2734	30
CL	1197.82	0.2571	32
E10	1392.50	0.2570	32

The peak intensity for acid leached and annealed samples increased thus increasing the crystallinity of the synthesized powders. The maximum peak intensity was obtained for sample E10 in comparison to other samples. A slight decrement in the full width at half maximum (FWHM) of the peak was also observed. The decrease in FWHM resulted in an increase of crystallite size by 2 nm. A similar trend was seen for the other peaks as well. As evident from the literature [13-16], if there is an increase in peak intensity, crystallinity and crystallite size then the photoluminescence efficiency for that sample increased. With the increase of crystallite size, the number of atoms on the surface and in the grain boundary decreases, which in turn decreases the non-radiative recombination, thus, increasing the photoluminescence emission intensity. In the present case, the final obtained sample E10 is more crystalline with pure phase, therefore, its photoluminescence efficiency should be more. Also annealing at high temperature (600°C) removes defect centers, which would otherwise have served as non-radiative relaxation centers and would have quenched photoluminescence efficiency. Therefore, the decrease in defect centers favors photoluminescence emission intensity enhancement. The average crystallite size of the particles was around 65 nm which was estimated from three diffraction peaks corresponding to planes (110), (107) and (114) using Debye-Scherrer equation [17]. The peak broadening of major diffraction peaks indicated that nano size particles were formed.

4.2.1.1. Rietveld Refinement

To determine the structural parameters of BAM:Eu^{2+}, Rietveld refinement was performed through Fullprof program using x-ray powder diffraction data. Structural refinement pattern for

sample E10 shown in figure 4.6., illustrates good agreement in the observed and the calculated results. It confirmed β-alumina structure of BAM:Eu^{2+} with space group P 63/m m c and lattice cell parameters, a = b = 5.6332 Å and c = 22.6779 Å. The final weighted R factors were R_{wp} = 11.4 and R_{exp} = 6.25. The positional atomic parameters obtained from the refinement are tabulated in table 4.3.

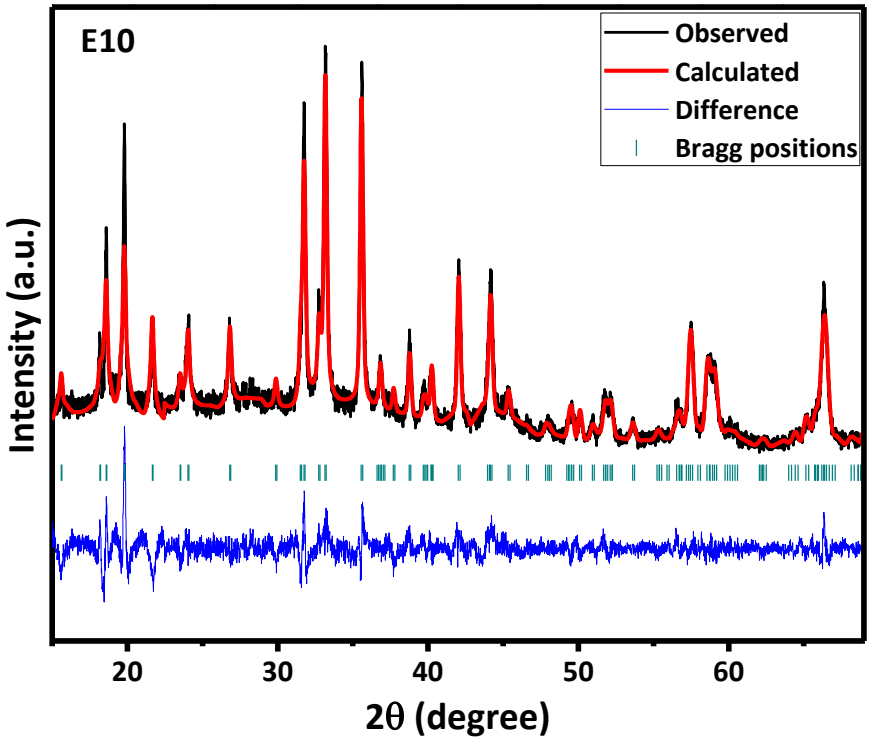

Figure 4.6: Rietveld analysis pattern for x-ray powder diffraction pattern of BAM:Eu^{2+}. Red solid line is the calculated intensity, black line is observed intensity, blue line is the difference between observed and calculated intensities, green lines show Bragg's position

It is observed from the occupation factor in table 4.3 that there was partial replacement of Ba atoms by Eu atoms and also the Al atoms by Mg atoms by occupying the tetrahedral site of the spinel block. The unity occupancy sum of Ba and Eu sites as well as Mg and Al sites confirmed this replacement. The partial replacement of Al atoms with Mg atoms at the tetrahedral site of spinel block was reported as one of the reason for the blue emission from BAM:Eu^{2+} [18-20]. The structural refinement data quality was checked by the goodness of fit parameter (GOF), given as GOF = R_{wp}/R_{exp} where R_{wp} is weighted profile residual and R_{exp} is expected profile residual [21,

22]. For the best fitted data GOF should approach unity. GOF for sample E10 was found to be 1.8. Secondary phases of $BaAl_2O_4$ and $BaAl_2O_4:Eu^{2+}$ were not found.

Table 4.3: Positional atomic parameters of BAM:Eu^{2+} where G is the occupation factor

Atom	Site	x/a	y/b	z/c	G
Ba	2d	1/3	2/3	¾	0.978
Eu	2d	1/3	2/3	¾	0.022
Al (1)	12k	0.16894	0.33805	-0.11598	1.0
Al (2)	4f	1/3	2/3	0.02668	0.474
Mg	4f	1/3	2/3	0.02668	0.526
Al(3)	4f	1/3	2/3	0.17643	1.0
Al (4)	2a	0	0	0	1.0
O (1)	12k	0.11952	0.23916	0.09909	1.0
O (2)	12k	0.54686	1.09364	0.15258	1.0
O (3)	4f	1/3	2/3	-0.08227	1.0
O (4)	4e	0	0	0.11197	1.0
O (5)	2c	1/3	2/3	¼	1.0

4.2.2. FESEM Study

FESEM images for samples C, CL and E10 are given in figure 4.7 (a, b, c & d). The dimensions of the obtained morphology were measured using ZEISS AxioVision software (microscope software for materials microscopy & industrial applications). As observed from figure 4.7 (a & b) the samples C and CL both exhibit irregular and non-homogeneous multifaceted plate like morphology. The plate length for combusted sample C was in the range 350 nm to 420 nm and plate thickness in the range 70 nm to 80 nm. Whereas, for combusted and acid leached sample CL, the plate length varied from 200 nm to 300 nm and plate thickness from 50 nm to 70 nm. After annealing, for sample E10 as seen in figure 4.7 (c & d), the multifaceted plate like morphology transformed into a mixture of multifaceted plates and rods. The plate length varied between 200 nm - 350 nm and plate thickness between 60 nm – 70 nm, whereas the rod length was in the range 300 nm – 500 nm with rod thickness between 50 nm – 60 nm.

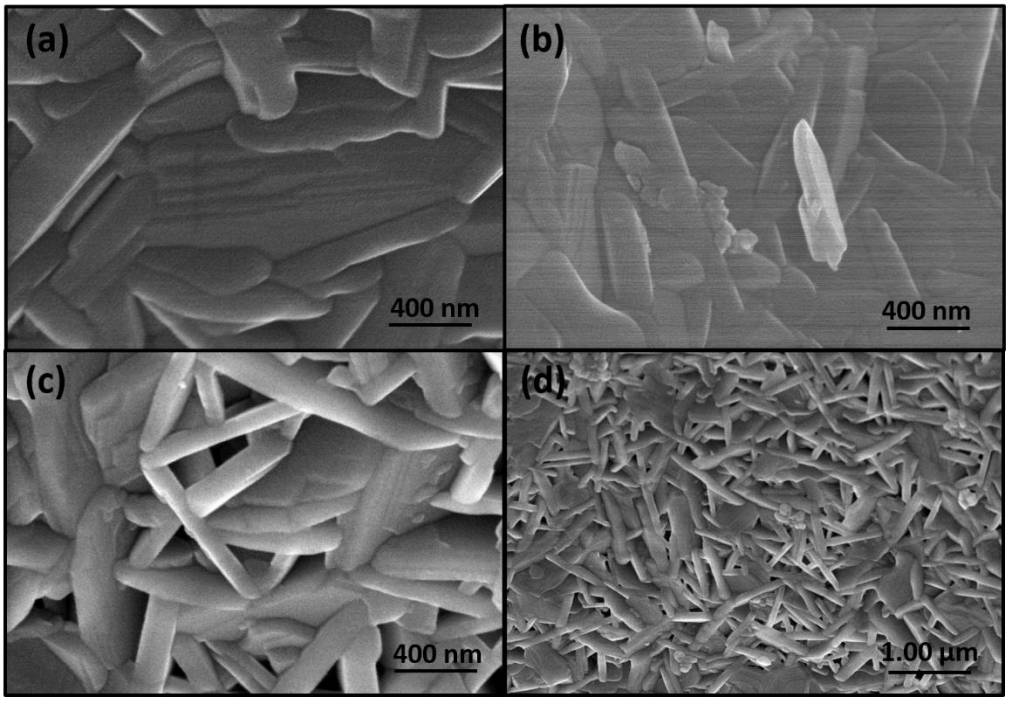

Figure 4.7: FESEM images for BAM:Eu^{2+} **(a)** combusted (C), **(b)** combusted and acid leached (CL) and **(c & d)** combusted, acid leached and annealed (E10)

4.2.3. TEM Study

TEM micrographs of samples C and E10 are shown in figure 4.8. The micrograph for the sample C given in figure 4.8 (a) illustrate non-uniform and multifaceted particles. The spacing between fringes 0.44 nm and 0.56 nm as shown in figure 4.8 (b) correspond to the interplanar spacing of (102) and (004) planes respectively. Annealing transformed the multifaceted and non-uniform morphology to a mix of multifaceted plates and rod-like morphology as shown in Figure 4.8 (e) and inset figure 4.8 (f). The average particle size calculated from TEM micrographs as shown in figure 4.8 (d) was approximately 65 nm, close to that estimated from Debye Scherrer formula [17]. As evident from literature, small particle size lead to larger specific surface area increasing the scattering of light [23]. Whereas, rod-like morphology had smaller specific surface area exhibiting less scattering as compared to the granular sample. Also, rods absorb light along both length and breadth hence improving the optical properties [24]. Thus, rod morphology facilitates better luminescence efficiency than any other morphology. Figure 4.8 (g) shows 0.28 nm and 0.33 nm lattice fringing corresponding to the interplanar spacing of (110) and (105) plane respectively.

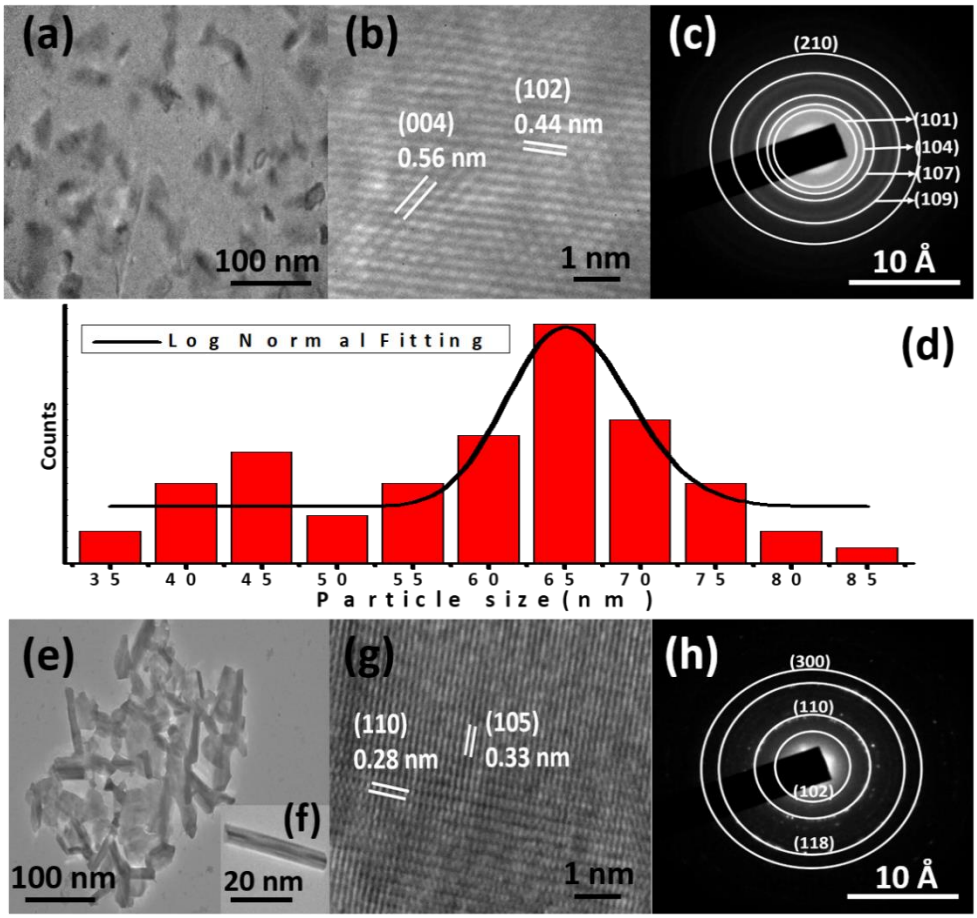

Figure 4.8: (a, b & c) TEM images of sample C **(d)** histogram showing distribution of particles for sample E10 and **(e, g & h)** TEM images of sample E10

4.2.4. FTIR Study

Figure 4.9 (a-c) shows the FTIR spectra of E10, CL and C respectively. The broad bands obtained at 3446 cm^{-1}, 3462 cm^{-1}, and 3445 cm^{-1} represented the O-H stretch, which became stronger for CL and then decreased significantly for E10. This may be due to the attachment of OH group with the particles during acid leaching. Whereas, annealing reduced the OH group resulting in a smaller band for E10. N=O stretch gave peaks at 1641 cm^{-1}, 1638 cm^{-1}, and 1511 cm^{-1} and N=O bend at 1407 cm^{-1}, 1385 cm^{-1} and 1384 cm^{-1}. These peaks indicate the presence of unreacted nitrates in the prepared samples with maximum amount for acid leached sample CL as acid leaching was performed with a mix of HNO_3 and H_2O. $BaAl_2O_4$ phase disassociated into $Ba(NO_3)_2$ in the presence of water which might have increased the concentration of nitro group for sample CL, that decreased after annealing for sample E10. O-H and nitro group decreased on subsequent annealing of the sample at 600˚C in argon atmosphere. The O-H group is known for

quenching the rare earth ions (Eu^{2+}) and hence reducing the luminescence intensity [25]. NO_3^- is also a PL quenching entity. It increases the non-radiative transition probability and therefore, reduces photoluminescence efficiency [26]. As there is a reduction in O-H and nitro group for sample E10, so the photoluminescence emission intensity for sample E10 should be higher than samples C and CL. Hence, these results favor the role of acid leaching and annealing in the preparation of BAM:Eu^{2+} nanophosphor with high luminescence efficiency.

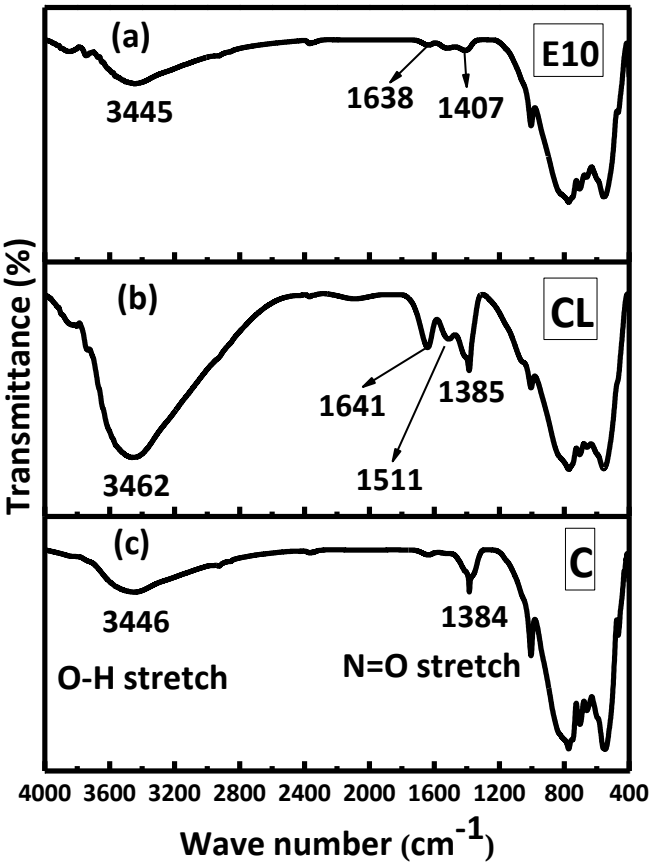

Figure 4.9: FTIR spectra for BAM:Eu^{2+} **(a)** combusted, acid leached and annealed (E10) **(b)** combusted and acid leached (CL) and **(c)** combusted (C)

4.2.5. Photoluminescence Study

Figure 4.10 (a & b) represents the photoluminescence excitation and emission spectra for samples C, CL and E10. Strong absorption from 280 nm to 420 nm range, peaking at about 330 nm was seen in the photoluminescence excitation (PLE) spectra. The broadband between 280 nm and 420 nm corresponded to $4f^7 \rightarrow 4f^6 5d^1$ transition of Eu^{2+} ions. The broad excitation band

(280 nm to 420 nm) matched well with NUV LED chip range (380 nm to 420 nm) making the phosphor applicable for NUV LED chips.

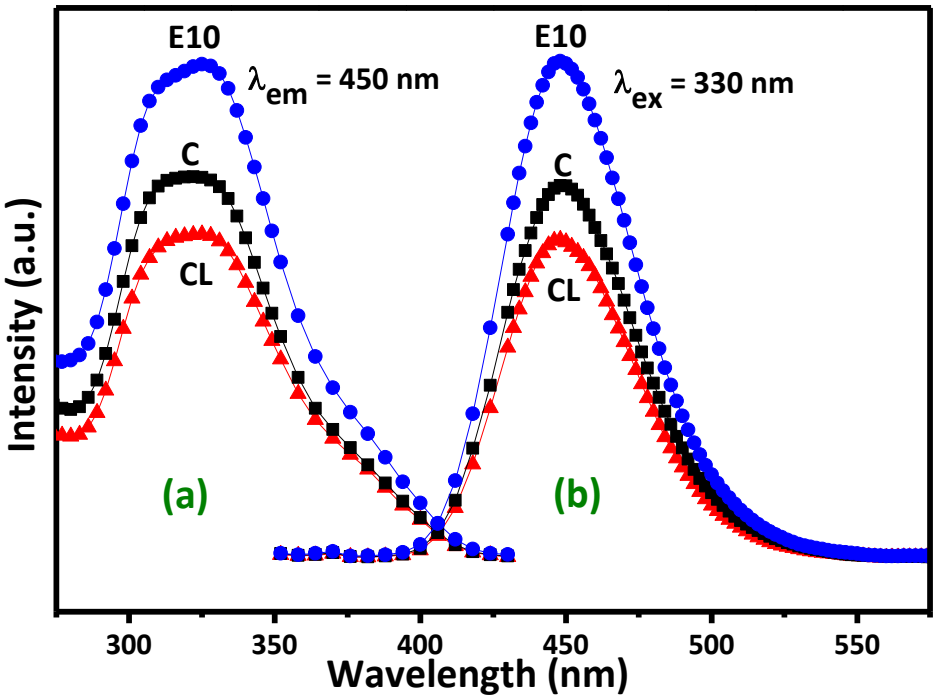

Figure 4.10: (a) Photoluminescence excitation spectra for samples C, CL and E10 **(b)** photoluminescence emission spectra for samples C, CL and E10

A broadband from 430 nm to 540 nm with highest intensity at 450 nm ascribing blue color to the phosphor was illustrated in the emission spectra. There was no shift in the peak maxima after acid leaching and annealing. As observed from the emission spectra, sample E10 had maximum photoluminescence intensity followed by samples C and CL. There was an increase in the photoluminescence intensity after annealing in the inert atmosphere as annealing improved crystallization of the particles and reduced Eu^{3+} to Eu^{2+}. Figure 4.11 shows the formation of long wavelength tail at approximately 510 nm. It is reported that $BaAl_2O_4:Eu^{2+}$ gives bluish green light at nearly 500 nm [11, 27]. Therefore, the additional green emission that resulted in the emission spectrum broadening at low energy edge could be due to the secondary $BaAl_2O_4:Eu^{2+}$ phase formation. The result shows good agreement with the XRD and FTIR results. XRD confirmed the phase purity and improved crystallinity of sample E10 hence increasing its photoluminescence intensity. This enhancement was due to the increase in crystallite size with better crystallization

and high temperature (600°C) annealing, which reduces defect centers. The decrease in number of defect centers reduces non-radiative relaxation centers that are unfavorable for photoluminescence thus enhancing photoluminescence emission intensity. FTIR study revealed the reduction of O-H and NO_3^- groups (PL quenching entities) for sample E10 thus, increasing its photoluminescence. Whereas, considerable increase in O-H and NO_3^- groups for sample CL increased the non-radiative transitions and decreased its photoluminescence.

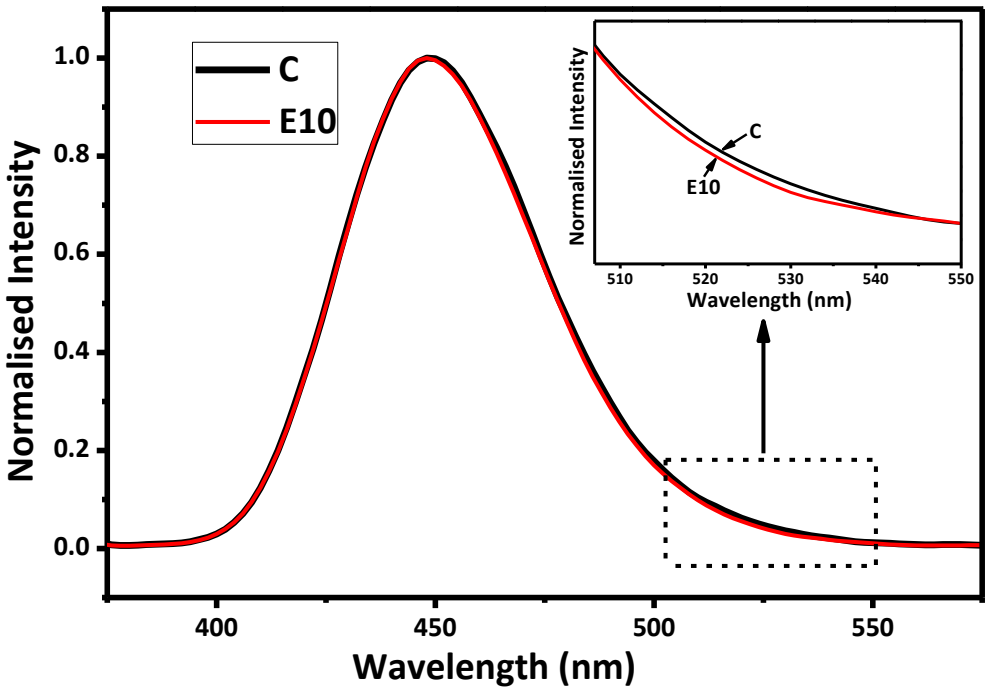

Figure 4.11: Normalised emission intensity for samples C and E10. The inset shows the long wavelength tail from 500 nm to 550 nm

The asymmetrical nature of the emission band relates to the three possible sites Eu^{2+} ions can occupy in a BAM matrix. These sites are namely, Beevers Ross (BR), anti Beevers Ross (a-BR) and mid-oxygen (mO) [28]. Therefore, the emission spectra was decomposed into three Gausians as shown in figure 4.12. Note that x-axis is presented on an energy scale. The Gaussian fitting of the emission spectrum for sample E10 resulted in three peaks at 21764 cm^{-1} (459 nm), 22650 cm^{-1} (441 nm) and 20291 cm^{-1} (492 nm) corresponding to the Eu^{2+} ions occupancy at a-BR, BR and mO sites respectively. This distribution of Eu^{2+} ions at different sites give variation in full width at half maximum (FWHM) leading to different chromaticity coordinates.

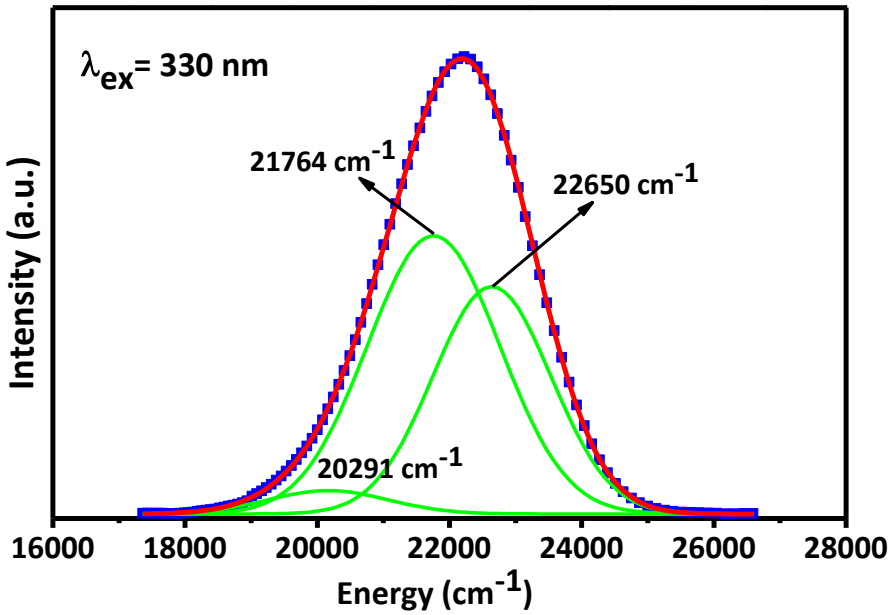

Figure 4.12: Gaussian fitted photoluminescence emission curve for sample E10

4.2.5.1. Chromaticity Coordinates with Color Purity

To study the chromaticity coordinates and color purity of BAM:Eu^{2+} nanophosphor, the Commission Internationale de I'Eclairage (CIE) chromaticity coordinate diagram was plotted as shown in figure 4.13. The obtained CIE coordinates and color purity values are tabulated in table 4.4. The x and y chromaticity coordinates for C lied in the blue region with values 0.152 and 0.06 respectively. Acid leaching (sample CL) altered the coordinates to 0.148 and 0.068, which further changed to 0.149 and 0.057 upon annealing (E10). The obtained CIE coordinates were near to the ideal CIE color coordinates of pure blue color (0.15, 0.06) [29]. The variation in the CIE coordinates was due to the variation in the FWHM of the emission spectrum composed of three emission bands corresponding to the three different sites of Eu^{2+} in BAM:Eu^{2+} (figure 4.12). As the occupancy of Eu^{2+} at the three sites varies the color coordinates and the FWHM changes accordingly.

The color purity of synthesised samples was calculated using equation (4.2):

$$\textbf{Color Purity}\ (\%) = \frac{\sqrt{(x-x_i)^2 + (y-y_i)^2}}{\sqrt{(x_d-x_i)^2+(y_d-y_i)^2}}\ \textbf{X 100} \qquad (4.2)$$

where, (x, y) are the chromaticity coordinates of the sample, (x_i, y_i) represent coordinates of white light in CIE diagram and are equal to (0.3333, 0.3333) and (x_d, y_d) are the coordinates of the dominant wavelength point [30]. Color purity of the samples was calculated by substituting the coordinates of (x, y), (x_d, y_d) and (x_i, y_i) to Eq. (4.2). For the final sample E10, color purity increased to 94%. Therefore, significant increase in photoluminescence intensity and improvement in color purity advocates the modification in the synthesis process.

Table 4.4: Color coordinates, FWHM and color purity of samples C, CL and E10

Sample	CIEx	CIEy	FWHM (nm)	Color Purity
C	0.152	0.06	54	93 %
CL	0.148	0.068	53.5	92%
E10	0.149	0.057	53	94%

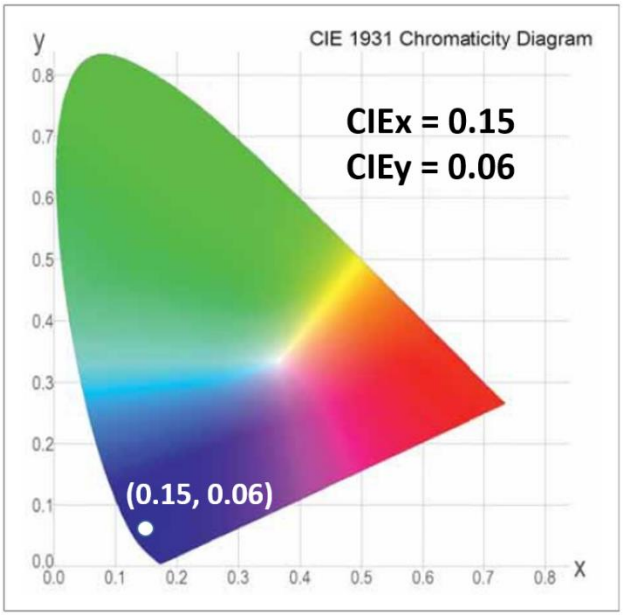

Figure 4.13: CIE color coordinate diagram for sample E10

References

[1] S. Som, S. Sharma, S. Lochab, Swift heavy ion induced structural and optical properties of Y_2O_3:Eu^{3+} nanophosphor, Materials Research Bulletin, 48 (2013) 844-851.

[2] M. Chroma, J. Pinkas, I. Pakutinskiene, A. Beganskiene, A. Kareiva, Processing and characterization of sol–gel fabricated mixed metal aluminates, Ceramics International, 31 (2005) 1123-1130.

[3] B.C. Jamalaiah, Y.R. Babu, Near UV excited $SrAl_2O_4$:Dy^{3+} phosphors for white LED applications, Materials Chemistry and Physics, 211 (2018) 181-191.

[4] B. Howe, A.L. Diaz, Characterization of host-lattice emission and energy transfer in $BaMgAl_{10}O_{17}$:Eu^{2+}, Journal of luminescence, 109 (2004) 51-59.

[5] X. Tian, Z. Weidong, C. Xiangzhong, Z. Chunlei, T. Xiaoming, H. Xiaowei, Low temperature luminescence properties of Tm^{3+} doped aluminate phosphor, Journal of Rare Earths, 24 (2006) 141-144.

[6] J. Chen, F. Gu, C. Li, Influence of precalcination and boron-doping on the initial photoluminescent properties of $SrAl_2O_4$:Eu, Dy phosphors, Crystal Growth and Design, 8 (2008) 3175-3179.

[7] L. Yang, B. Kruse, Revised Kubelka–Munk theory. I. Theory and application, JOSA A, 21 (2004) 1933-1941.

[8] A.E. Morales, E.S. Mora, U. Pal, Use of diffuse reflectance spectroscopy for optical characterization of un-supported nanostructures, Revista mexicana de física, 53 (2007) 18-22.

[9] C.R. Ronda, Luminescence: from theory to applications, John Wiley & Sons, 2007.

[10] Y. Zhou, J. Lin, Morphology control and luminescence properties of $BaMgAl_{10}O_{17}$:Eu^{2+} phosphors prepared by spray pyrolysis, Journal of Solid State Chemistry, 178 (2005) 441-447.

[11] S. Oshio, K. Kitamura, T. Shigeta, S. Horii, T. Matsuoka, S. Tanaka, H. Kobayashi, Firing Technique for Preparing a $BaMgAl_{10}O_{17}$:Eu^{2+} Phosphor with Controlled Particle Shape and Size, Journal of the Electrochemical Society, 146 (1999) 392-399.

[12] M. Casapu, J.-D. Grunwaldt, M. Maciejewski, M. Wittrock, U. Göbel, A. Baiker, Formation and stability of barium aluminate and cerate in NO_x storage-reduction catalysts, Applied Catalysis B: Environmental, 63 (2006) 232-242.

[13] T.K. Anh, P.T.M. Chau, N.T.Q. Hai, L.Q. Minh, Cathodo-, Thermo-, and Photo-luminescent Properties of Nano Y_2O_3:Eu^{3+} Fabricated by Controlled Combustion Synthesis.

[14] N. Lakshminarasimhan, U. Varadaraju, Role of crystallite size on the photoluminescence properties of $SrIn_2O_4$:Eu^{3+} phosphor synthesized by different methods, Journal of Solid State Chemistry, 181 (2008) 2418-2423.

[15] H. Li, X. Pu, J. Yin, X. Wang, S. Yao, H.M. Noh, J.H. Jeong, Effect of crystallite size and crystallinity on photoluminescence properties and energy transfer of Y_6MoO_{12}:Eu, Journal of the American Ceramic Society, 99 (2016) 954-961.

[16] W.-N. Wang, W. Widiyastuti, T. Ogi, I.W. Lenggoro, K. Okuyama, Correlations between crystallite/particle size and photoluminescence properties of submicrometer phosphors, Chemistry of materials, 19 (2007) 1723-1730.

[17] S. Som, S. Sharma, S. Lochab, Swift heavy ion induced structural and optical properties of Y_2O_3:Eu^{3+} nanophosphor, Materials Research Bulletin, 48 (2013) 844-851.

[18] G. Collin, R. Comes, J. Boilot, P. Colomban, Crystal structure and ion-ion correlation of ion-rich β alumina type compounds I. Magnesium doped potassium rich β alumina, Solid State Ionics, 1 (1980) 59-68.

[19] J. Sommerdijk, A. Stevels, Behavior of phosphors with aluminate host lattices, Philips Technical Review, 37 (1977) 221-233.
[20] K.-B. Kim, Y.-I. Kim, H.-G. Chun, T.-Y. Cho, J.-S. Jung, J.-G. Kang, Structural and optical properties of $BaMgAl_{10}O_{17}:Eu^{2+}$ phosphor, Chemistry of materials, 14 (2002) 5045-5052.
[21] L. McCusker, R. Von Dreele, D. Cox, D. Louër, P. Scardi, Rietveld refinement guidelines, Journal of Applied Crystallography, 32 (1999) 36-50.
[22] Y.-I. Kim, K.-B. Kim, M.-J. Jung, J.-S. Hong, Combined Rietveld refinement of $BaMgAl_{10}O_{17}:Eu^{2+}$ using X-ray and neutron powder diffraction data, Journal of luminescence, 99 (2002) 91-100.
[23] Z.H. Zhang, L. Chen, Q.H. Gan, Q. Tian, C.L. Chen, Z.L. Huang, Morphology and luminescent properties of $BaMgAl_{10}O_{17}:Eu^{2+}$ phosphor synthesized by a hydrothermal homogeneous precipitation method, physica status solidi (a), 210 (2013) 378-382.
[24] C.J. Murphy, N.R. Jana, Controlling the aspect ratio of inorganic nanorods and nanowires, Advanced Materials, 14 (2002) 80.
[25] S. Som, S. Sharma, Eu^{3+}/Tb^{3+}-codoped Y_2O_3 nanophosphors: Rietveld refinement, bandgap and photoluminescence optimization, Journal of Physics D: Applied Physics, 45 (2012) 415102.
[26] A. Singh, S. Singh, S. Rai, Role of Li^+ ion in the luminescence enhancement of lanthanide ions: favorable modifications in host matrices, RSC advances, 4 (2014) 27039-27061.
[27] S. Feilong, Z. Junwu, Blue-green $BaAl_2O_4:Eu^{2+}$, Dy^{3+} phosphors synthesized via combustion synthesis method assisted by microwave irradiation, Journal of Rare Earths, 29 (2011) 326-329.
[28] K. Mishra, M. Raukas, A. Ellens, K. Johnson, A scattered wave model of electronic structure of Eu^{2+} in $BaMgAl_{10}O_{17}$ and associated excitation processes, Journal of luminescence, 96 (2002) 95-105.
[29] C.S. McCamy, Correlated color temperature as an explicit function of chromaticity coordinates, Color Research & Application, 17 (1992) 142-144.
[30] E.F. Schubert, Light-emitting diodes Cambridge University Press, New York, (2006) 35-40.

CHAPTER 5

RESULTS AND DISCUSSION-II

Overview

Effect of morphology on the optical properties of BAM:Eu^{2+} nanophosphor is dicussed in this chapter. Phase purity and morphology are essential parameters to get high luminescence efficiency of phosphors. In chapter 4, pure phase BAM:Eu^{2+} was obtained without using any surfactant. In this chapter the role of different template agents in order to control the morphology hence to get better luminescence properties of BAM:Eu^{2+} nanophosphor is described. Water-soluble β-cyclodextrin and thioglycerol were used as template agents in the synthesis process to modify the morphology of the BAM:Eu^{2+} nanophosphor prepared through solution combustion synthesis technique. The structural, morphological and optical properties of the samples were studied. Also, the CIE color coordinates and thermal stability of the prepared nanophosphors was analyzed to check their efficiency and applicability.

5.1. Effect of Morphology on the Optical Properties of BAM:Eu^{2+} Nanophosphor

Morphology is an essential parameter for achieving phosphors with high brightness. Morphology can be modified by the incorporation of the template agents. The inclusion of template agents in the precursor is an efficient technique to control its morphology for achieving better photoluminescence efficiency. The properties of the phosphors can be tailored by modifying the characteristics of the precursor. Water-soluble soft templates help in modifying the morphology by preventing agglomeration and thus controlling the growth of particles through micelle formation [1, 2]. In the present study, BAM:Eu^{2+} nanophosphors were prepard through solution combustion synthesis technique using β-cyclodextrin (β-CD) and thioglycerol (TG) as template agents. In all the prepared samples, the Eu^{2+} molar concentration was fixed at 10 mol% as the maximum photoluminescence emission for BAM:Eu^{2+} was obtained at 10 mol% concentration of Eu^{2+}. Whereas, the molar concentration of β-CD was varied from 0.001 mol% to 0.007 mol% and that of TG was varied from 0.01 mol% to 0.06 mol%. The details for the samples and their corresponding sample codes are already given in chapter 3 (Experimental techniques (table 3.1)) but for simplicity, details of prepared samples and their codes for the present chapter are tabulated in table 5.1.

Table 5.1: Samples with their corresponding codes

S.No.	Sample Name	Concentration (mol %)	Sample Code
1.	BAM:Eu^{2+}	Eu (10%)	E10
2.	BAM:Eu^{2+}/β-CD	Eu (10), β-CD (0.001, 0.003, 0.005, 0.007)	ECD1, ECD3, ECD5, ECD7
3.	BAM:Eu^{2+}/TG	Eu (10), TG (0.01, 0.02, 0.04, 0.06)	ETG1, ETG2, ETG4, ETG6

The outcome for the characterizations of the samples is discussed below.

5.1.1. XRD Study

XRD patterns of samples ECD3, ETG2 and E10 are shown in figure 5.1 (a-c) respectively. The obtained XRD patterns were in good agreement with the JCPDS card number 00-026-0163 having β- alumina structure with P 63/m m c space group. All the diffraction peaks were well indexed with (hkl) values. Addition of β-CD and TG templates had no significant influence on the

host. The absence of any additional peak indicated the formation of pure phase of BAM. The average crystallite size was calculated corresponding for the peaks (110), (107) and (114) using Debye-Scherrer equation (5.1)

$$\boldsymbol{D = \frac{k\lambda}{\beta\, Cos\, \theta}} \tag{5.1}$$

where D is the crystallite size, k is a constant (taken as 0.9), λ is wavelength of incident X-rays (0.154 nm), θ is the Bragg diffraction angle and β is FWHM of peak in radians [3].

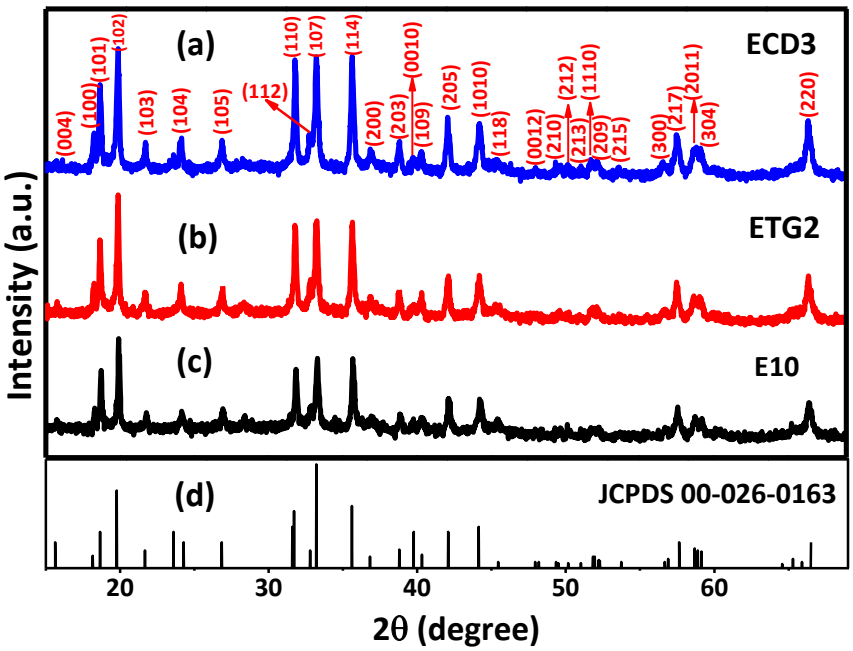

Figure 5.1: XRD patterns of samples **(a)** ECD3 **(b)** ETG2 **(c)** E10 compared with **(d)** JCPDS card no. 00-026-0163

The average crystallite size and the unit cell parameters for samples E10, ETG2 and ECD3 are tabulated in table 5.2. The average crystallite size increased with the addition of TG and β-CD as observed from table 5.2. Whereas, the unit cell parameters for the three samples remain approximately the same. The highest average crystallite size was obtained for ECD3 as compared to E10 and ETG2. From the literature, it is evident that increase in crystallite size enhanced the photoluminescence emission [4, 5]. With the increase in crystallite size, number of atoms on the surface and in the grain boundary decreases, which in turn decreases the non-radiative recombination, thus, increasing the photoluminescence emission intensity [6-8]. Here ECD3 had

maximum average crystallite size so its photoluminescence efficiency should be more followed by ETG2 and E10.

Table 5.2: Peak parameters for the plane (107) of E10, ETG2 and ECD3 samples

S. No.	Sample Name	Crystallite size (nm)	a = b (Å)	c (Å)
1.	**E10**	65	5.63	22.68
2.	**ETG2**	73	5.63	22.68
3.	**ECD3**	83	5.62	22.67

5.1.2. FESEM Study

Morphology of the as-prepared samples was studied by FESEM. Figure 5.2 (a - d) illustrates the FESEM images of (a & b) E10 (c) ETG2 (d) ECD3 samples respectively. The dimensions of the obtained morphology was measured using ZEISS AxioVision software (microscope software for materials microscopy & industrial applications).

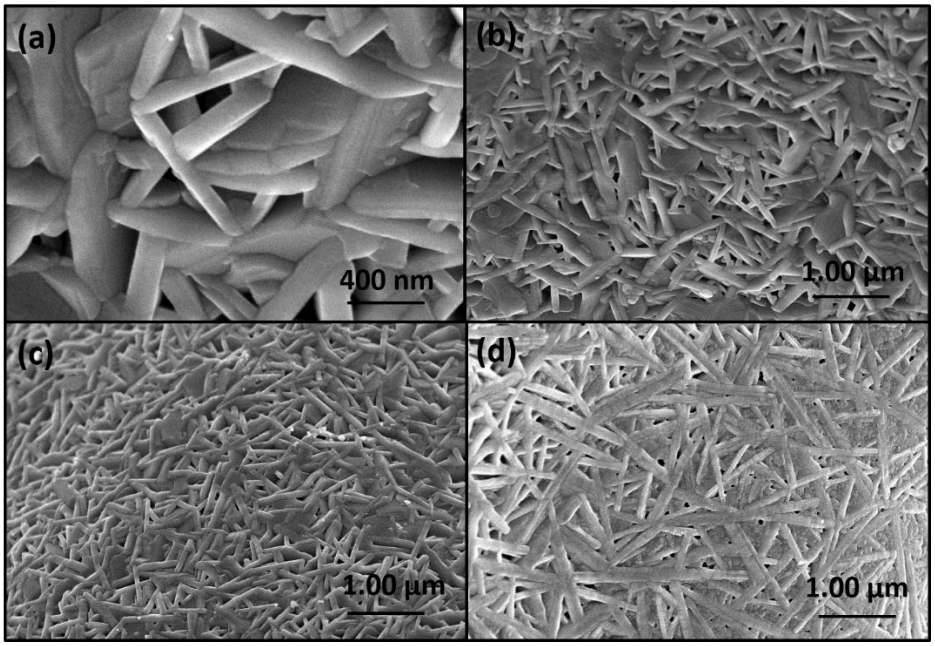

Figure 5.2: FESEM images of **(a & b)** E10 **(c)** ETG2 **(d)** ECD3

As observed from figure 5.2 (a & b), the E10 nanophosphor had an irregular non-homogeneous morphology with a mixture of multifaceted plate and rod-like morphology. The plate length varied between 200 nm - 350 nm and plate thickness between 60 nm – 70 nm, whereas the rod length was in the range 300 nm – 500 nm with rod thickness between 50 nm – 60 nm. The addition of TG (figure 5.2 (c)) transformed the plate-like morphology to rod-like morphology with length in the range 500 nm – 600 nm and diameter in the range 80 nm - 90 nm. Incorporation of β-CD also gave rod-like morphology but here the rods with larger length lying in the range 600 nm - 800 nm and diameter between 40 nm - 60 nm range were obtained (figure 5.2(d)). In the present study, water-soluble polymers β-CD and TG were used to control the growth morphology of the particles. These polymers induce micelle formation due to the vander Waals attraction of the hydrophobic groups. As shown in figure 5.3 (a - b), TG has a chain type structure whereas β-CD has a cyclic structure [9, 10]. Upon addition of TG to the solution, micelles were formed due to the stretching of linear chain resulting in the formation of rods. β-CD has a cyclic structure with hydrophobic in the inside and hydrophilic on the outside thus forming cylindrical micelles facilitating rod formation [11]. Therefore β-CD and TG had led to the growth of rod-like morphology of BAM:Eu^{2+}. Also, β-CD and TG resulted in homogeneous morphology hence increasing the crystallinity of the samples with β-CD and TG.

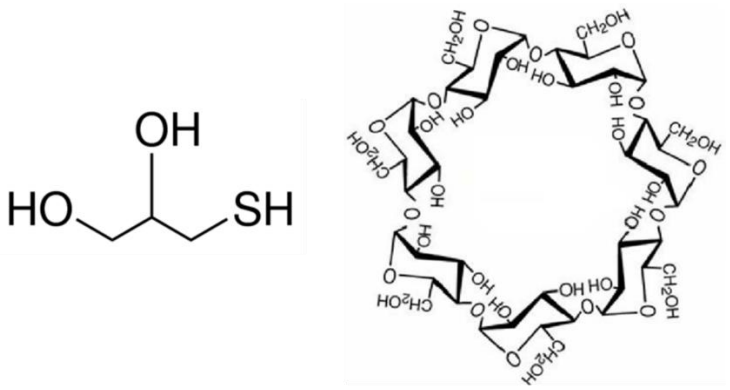

Figure 5.3: Structure of **(a)** TG **(b)** β-CD

5.1.3. FTIR Study

The FTIR spectra for samples E10, ETG2 and ECD3 are given in figure 5.4 (a, b & c) respectively. The broad peaks at 3445 cm^{-1}, 3600 cm^{-1} and 3100 cm^{-1} are due to the O-H stretching vibration indicating the presence of adsorbed water. The peaks at 1638 cm^{-1} and 1407 cm^{-1} for sample E10 (figure 5.4 (a)) are the nitrate stretching frequencies and the peak at 1520 cm^{-1} and 1523 cm^{-1} for samples with TG and β-CD are due to N-O asymmetric stretch. These peaks corresponding to nitro group are due to the nitrate precursors used for the synthesis of the samples [12]. The peaks at approximately 1188 cm^{-1} for samples with TG and β-CD are due to C-O stretch. The peaks obtained at 1004 cm^{-1} and 556 cm^{-1} are due to AlO_6 aluminate group whereas the peaks at 772 cm^{-1} and 704 cm^{-1} are of AlO_4 aluminate group. A small peak obtained at 662 cm^{-1} corresponds to Al – O vibrations [13, 14]. The peaks from 1000 cm^{-1} – 500 cm^{-1} correspond to the spinel block $MgAl_{10}O_{16}$ of β-alumina structure composed of AlO_4 tetrahedrons and AlO_6 octahedrons [15].

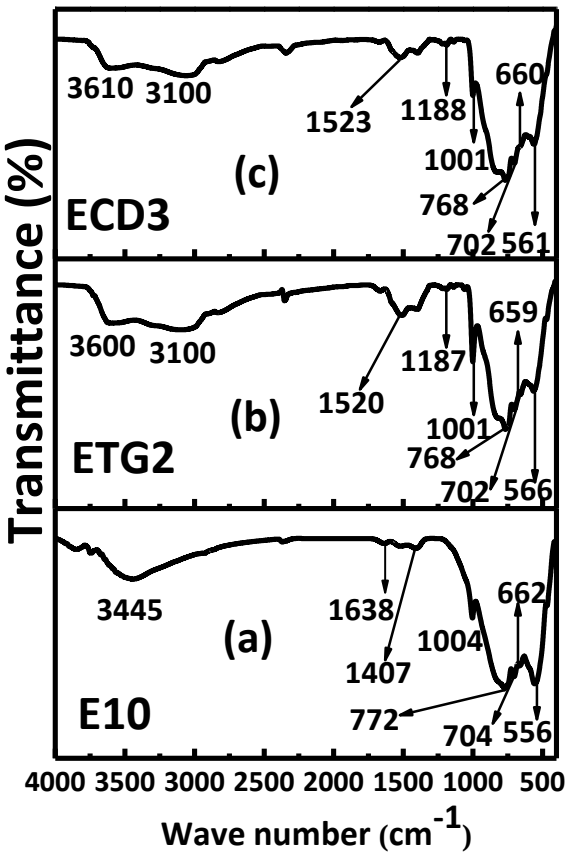

Figure 5.4: FTIR spectra for samples **(a)** E10 **(b)** ETG2 and **(c)** ECD3

5.1.4. Photoluminescence Study

Photoluminescence excitation spectra of E10, ETG2 and ECD3 samples are exhibited in figure 5.5 (a). The excitation spectra were recorded while monitoring emission at 450 nm giving strong excitation peak at the wavelength of 330 nm and a weak excitation peak at approximately 250 nm. These peaks were due to the $4f^7$- $4f^65d^1$ electronic transitions of Eu^{2+} ions. The addition of TG and β-CD did not alter the peak maximum at 330 nm. For optimizing the concentration of TG and β-CD to obtain maximum photoluminescence emission, BAM:Eu^{2+} was synthesized with varying molar concentrations of TG and β-CD. As shown in figure 5.6 (a & b), 0.02 mol% concentration of TG and 0.003 mol% concentration of β-CD gives maximum photoluminescence output.

Photoluminescence emission spectra of E10, ETG2 and ECD3 samples recorded under 330 nm excitation are given in figure 5.5 (b). A broadband emission spectra peaking at 450 nm was observed for the as-prepared nanophosphors. The peak maxima at 450 nm is due to the $4f^65d^1$ – $4f^7$ electronic transitions of Eu^{2+} ions. The highest photoluminescence efficiency was obtained with β-CD followed by TG. As observed from XRD and FESEM study, inclusion of β-CD and TG helped in obtaining increased crystallinity, crystallite size and homogeneous morphology of the phosphor particles. Photoluminescence efficiency of the phosphors strongly depends upon their crystallinity, crystallite size and morphology [16, 17]. It is already reported in the literature that the large crystallite size had a small specific surface area thus decreasing the scattering of light [18]. In comparison to TG, the increase in crystallite size and crystallinity with β-CD was more hence enhancing its photoluminescence efficiency. Also, the rod-like morphology of CD3 and TG2 added has increased the photoluminescence emission as the rod-like morphology has smaller specific surface area and exhibit less scattering of light. Rods absorb light along both length and breadth of the rod resulting in the increase of photoluminescence emission [19]. Whereas E10 had non homogeneous morphology with a mixture of both rod and multifaceted plate like morphology. The scattering of light for plate like morphology was more due to the large specific surface area thus providing resistance to its photoluminescence emission efficiency. The approximate percentage increase with β-CD is 30% and with TG is 13%. Thus maximum photoluminescence emission was obtained with the addition of β-CD in BAM:Eu^{2+} nanophosphor. The results are in good agreement with the XRD and FESEM studies.

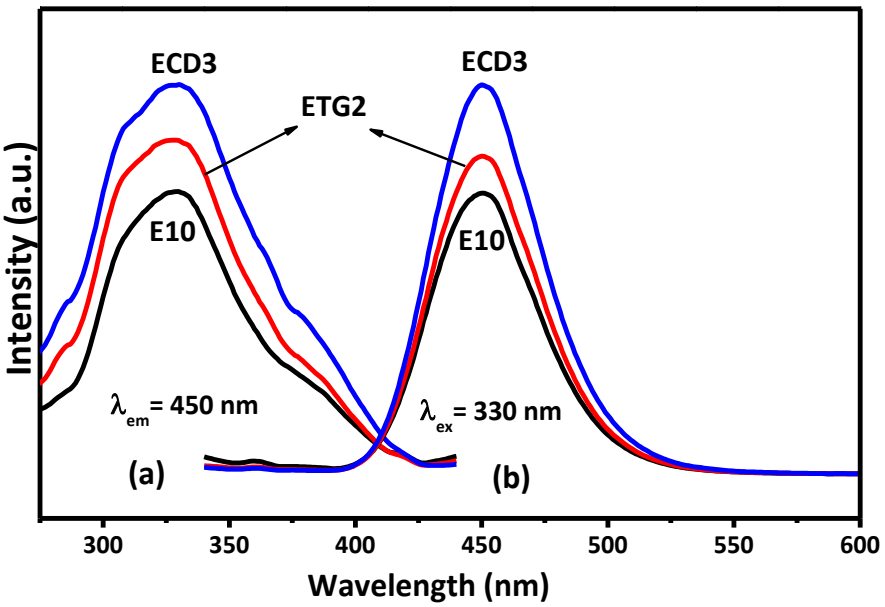

Figure 5.5: Photoluminescence **(a)** excitation spectra and **(b)** emission spectra of E10, ETG2 and ECD3 samples

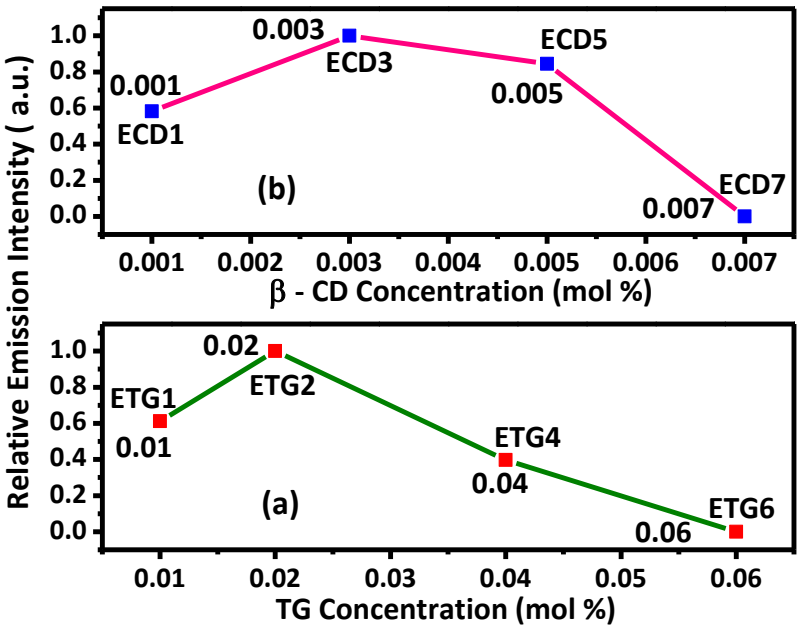

Figure 5.6: Relative emission intensity of **(a)** TG in E10 **(b)** β-CD in E10 powders

5.1.4.1. CIE Coordinates with Color Purity

The photometric characteristics of the as-prepared nanophosphors has been studied by calculating the Commission Internationale de l'Eclairage (CIE) color coordinates and color purity [20]. CIE chromaticity coordinate diagram of samples E10, ETG2 and ECD3 are illustrated in figure 5.7 (a, b & c) respectively. It was noted that the color coordinates did not change much with the addition of β-CD and TG. The color coordinates lie in the blue region of the CIE chromaticity coordinate diagram and are near to the ideal blue coordinates (0.15, 0.06) [20].

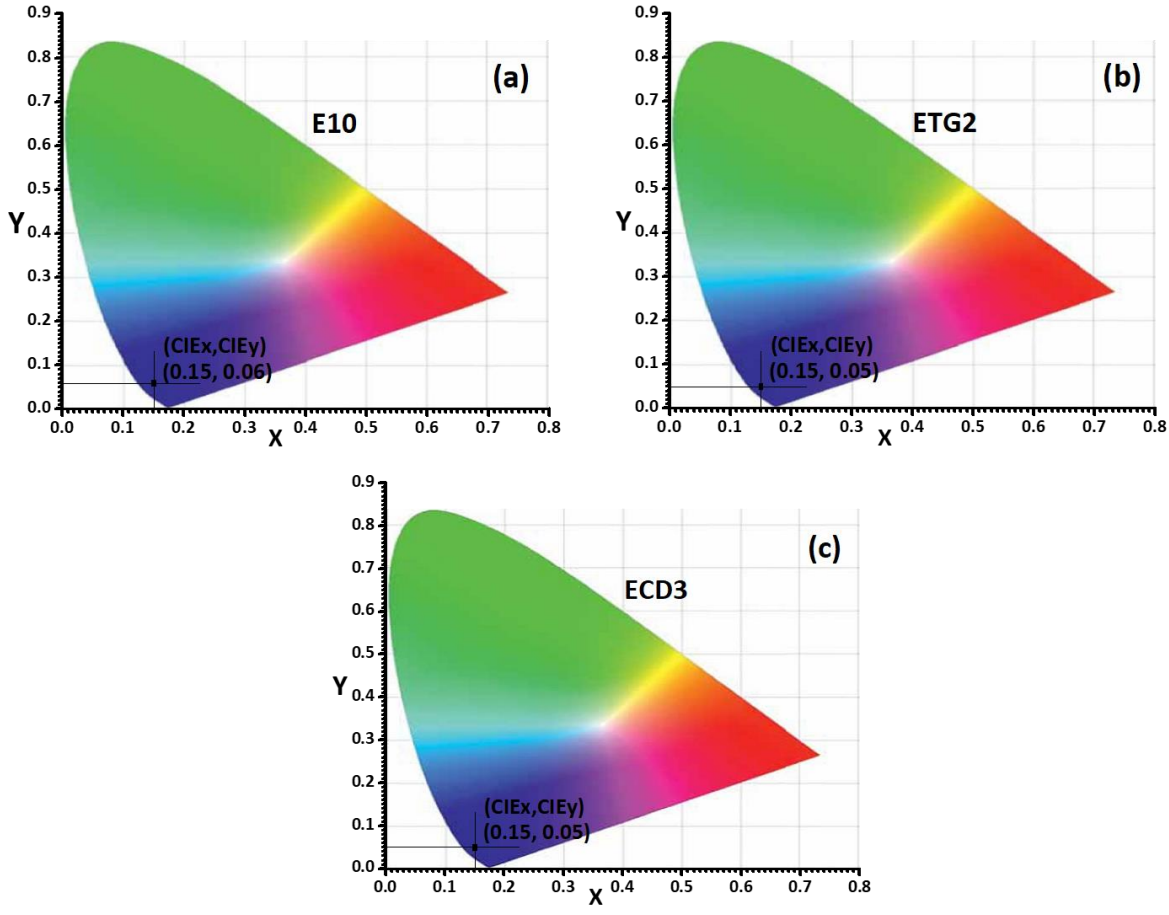

Figure 5.7: CIE chromaticity coordinate diagram of **(a)** E10 **(b)** ETG2 and **(c)** ECD3 phosphors

The color purity of synthesized sample was calculated using equation (5.2):

$$\textbf{Color Purity}\ (\%) = \frac{\sqrt{(x-x_i)^2+(y-y_i)^2}}{\sqrt{(x_d-x_i)^2+(y_d-y_i)^2}} \times 100 \qquad (5.2)$$

where, (x, y) are the chromaticity coordinates of the sample, (x_d, y_d) represent coordinates of dominant-wavelength point and (x_i, y_i) are the coordinates of white light in CIE diagram which are taken as (0.3333, 0.3333) [21, 22]. Color purity was determined by substituting the values of (x, y), (xi, yi) and (x_d, y_d) in equation (5.2). The values of CIE color coordinates and color purity are summarized in table 5.3. The obtained nanophosphors exhibited good color purity of approximately 94%. Therefore, efficient blue phosphors were obtained with β-CD and TG without affecting the color coordinates and color purity.

Table 5.3: The CIE coordinates and color purity of E10, ETG2 and ECD3 samples

Sample Name	CIEx	CIEy	Color Purity
E10	0.149	0.057	94.2%
ETG2	0.147	0.052	93.9%
ECD3	0.146	0.052	93.9%

5.1.5. Thermal Stability Study

Thermal stability of phosphors is of much importance as the phosphors have to undergo high-temperature processing steps in the temperature range of 500°C to 600°C in air during the fabrication of the displays. BAM:Eu^{2+} is the most vulnerable material w. r. t. panel processing. This high temperature deteriorates the brightness and color quality of the BAM:Eu^{2+} phosphor and is a major shortcoming of BAM:Eu^{2+} phosphor [5]. To check the thermal stability, the as-prepared nanophosphors were baked at 600°C for 30 minutes in ambient air [23-25]. The photoluminescence spectra of the baked samples w. r. t. their corresponding unbaked samples is given in figure 5.8 (a - c) and the relative luminescence intensity of the baked samples in comparison to unbaked BAM:Eu^{2+} sample is given in figure 5.9. A decrement in the photoluminescence efficiency for all the samples have been observed after the heat treatment. However, the maximum decrease of 29% was observed for the no template added BAM:Eu^{2+} (E10) and the minimum of 10% for BAM:Eu^{2+}/TG (ETG2) as noted from figure 5.8. It was observed from figure 5.9 that the photoluminescence efficiency of baked ECD3 and baked ETG2 samples was still higher than the unbaked E10 sample with the maximum photoluminescence of ECD3 sample.

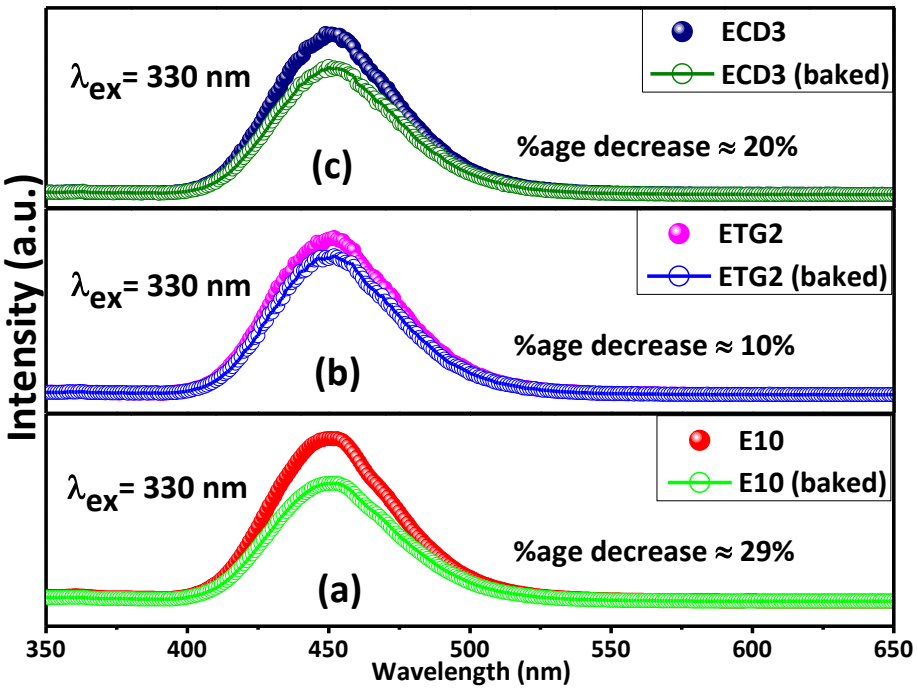

Figure 5.8: Photoluminescence emission spectra of **(a)** baked and unbaked E10 **(b)** baked and unbaked ETG2 **(c)** baked and unbaked ECD3 samples

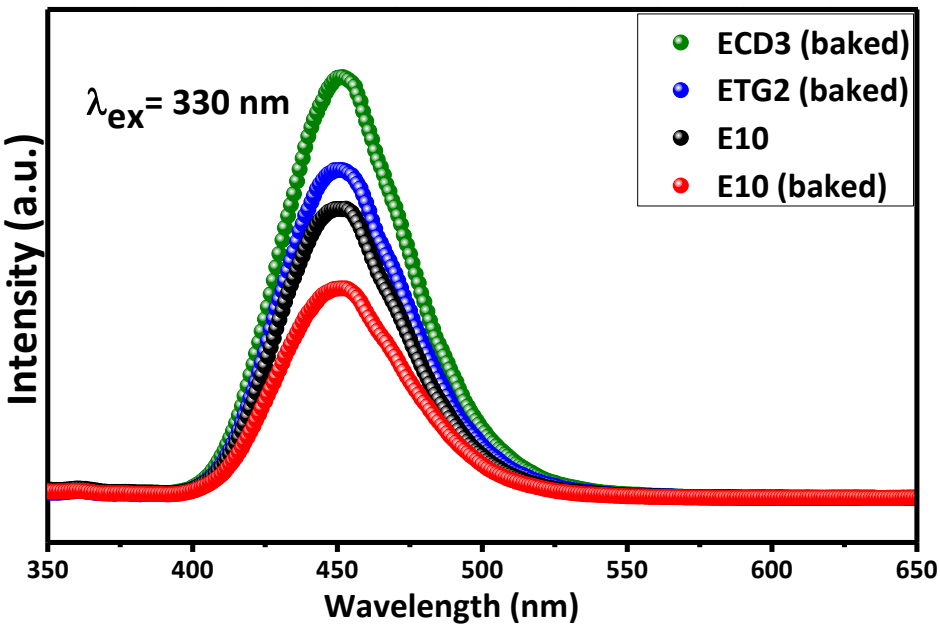

Figure 5.9: Comparison of photoluminescence emission of baked samples with unbaked E10

BAM:Eu^{2+} has hexagonal β-alumina structure with $MgAl_{10}O_{16}$ as spinel block and BaO as conduction plane. It has high ion mobility for cations in its conduction layer. According to the various reported researches there are two main causes of thermal degradation in BAM:Eu^{2+} phosphor. Firstly, oxidation of Eu^{2+} to Eu^{3+}, secondly, diffusion of cations (Ba^{2+}, Eu^{2+}, Mg^{2+}, Al^{3+}) in the inter slabs of the β-alumina structure and the creation of the oxygen vacancies [24, 26-28]. Template agents act as binding agents, which bind the metal ions forming chelates and reduce the oxygen vacancies which in turn decreases the cation diffusion hence arresting the thermal degradation [29, 30]. Also with the decrease of oxygen vacancies there is a decrease in the adsorption of oxygen atoms preventing the oxidation of Eu^{2+} to Eu^{3+}. Therefore, β-CD and TG proved to be helpful in increasing the thermal stability of BAM:Eu^{2+} nanophosphor. Although there was a slight decrease in the photoluminescence emission of BAM:Eu^{2+}/β-CD and BAM:Eu^{2+}/TG after baking still the emission was higher than the unbaked BAM :Eu^{2+} nanophosphor ensuring good thermal stability and quality of the BAM :Eu^{2+} nanophosphor prepared with β-CD and TG. β-CD gave the better result as template agent.

References

[1] M.-P. Pileni, The role of soft colloidal templates in controlling the size and shape of inorganic nanocrystals, Nature materials, 2 (2003) 145.

[2] M. Pileni, Control of the size and shape of inorganic nanocrystals at various scales from nano to macrodomains, The Journal of Physical Chemistry C, 111 (2007) 9019-9038.

[3] B.D. Cullity, S.R. Stock, Elements of X-ray Diffraction, Pearson Education, 2014.

[4] S. Som, S. Sharma, S. Lochab, Swift heavy ion induced structural and optical properties of Y_2O_3:Eu^{3+} nanophosphor, Materials Research Bulletin, 48 (2013) 844-851.

[5] T.K. Anh, P.T.M. Chau, N.T.Q. Hai, L.Q. Minh, Cathodo-, Thermo-, and Photo-luminescent Properties of Nano Y_2O_3:Eu^{3+} Fabricated by Controlled Combustion Synthesis.

[6] N. Lakshminarasimhan, U. Varadaraju, Role of crystallite size on the photoluminescence properties of $SrIn_2O_4$:Eu^{3+} phosphor synthesized by different methods, Journal of Solid State Chemistry, 181 (2008) 2418-2423.

[7] H. Li, X. Pu, J. Yin, X. Wang, S. Yao, H.M. Noh, J.H. Jeong, Effect of crystallite size and crystallinity on photoluminescence properties and energy transfer of Y_6MoO_{12}:Eu, Journal of the American Ceramic Society, 99 (2016) 954-961.

[8] W.-N. Wang, W. Widiyastuti, T. Ogi, I.W. Lenggoro, K. Okuyama, Correlations between crystallite/particle size and photoluminescence properties of submicrometer phosphors, Chemistry of materials, 19 (2007) 1723-1730.

[9] M. Goodman, W. Weigle, Nonspecific activation of murine lymphocytes. I. Proliferation and polyclonal activation induced by 2-mercaptoethanol and alpha-thioglycerol, Journal of Experimental Medicine, 145 (1977) 473-489.

[10] R.D. Haynes, Using cyclodextrin to stabilize and control colloidal microstickies to improve paper machine runnability, in: TAPPI Engineering, Pulping and Environmental Conference, Memphis, TN, 2009.

[11] L. Tan, A. Lim, Z. Chee, Y. Wong, Y. Huang, H. Ong, Q. Wee, J. Ho, R. Steeman, S. Chua, Hierarchical nano/microstructures on silicon surface with ultra low reflectance for photovoltaic applications, physica status solidi (c), 9 (2012) 1873-1877.

[12] M. Chroma, J. Pinkas, I. Pakutinskiene, A. Beganskiene, A. Kareiva, Processing and characterization of sol–gel fabricated mixed metal aluminates, Ceramics International, 31 (2005) 1123-1130.

[13] X. Tian, Z. Weidong, C. Xiangzhong, Z. Chunlei, T. Xiaoming, H. Xiaowei, Low temperature luminescence properties of Tm^{3+} doped aluminate phosphor, Journal of Rare Earths, 24 (2006) 141-144.

[14] J. Chen, F. Gu, C. Li, Influence of precalcination and boron-doping on the initial photoluminescent properties of $SrAl_2O_4$:Eu, Dy phosphors, Crystal Growth and Design, 8 (2008) 3175-3179.

[15] B. Howe, A.L. Diaz, Characterization of host-lattice emission and energy transfer in $BaMgAl_{10}O_{17}$:Eu^{2+}, Journal of luminescence, 109 (2004) 51-59.

[16] K.Y. Jung, D.Y. Lee, Y.C. Kang, H.D. Park, Improved photoluminescence of $BaMgAl_{10}O_{17}$ blue phosphor prepared by spray pyrolysis, Journal of luminescence, 105 (2003) 127-133.

[17] R. Rao, Morphology and stability of flux grown blue emitting BAM phosphors for plasma display panels applications, Journal of the Electrochemical Society, 152 (2005) H115-H119.

[18] Z.H. Zhang, L. Chen, Q.H. Gan, Q. Tian, C.L. Chen, Z.L. Huang, Morphology and luminescent properties of $BaMgAl_{10}O_{17}$:Eu^{2+} phosphor synthesized by a hydrothermal homogeneous precipitation method, physica status solidi (a), 210 (2013) 378-382.

[19] C.J. Murphy, N.R. Jana, Controlling the aspect ratio of inorganic nanorods and nanowires, Advanced Materials, 14 (2002) 80.
[20] C.S. McCamy, Correlated color temperature as an explicit function of chromaticity coordinates, Color Research & Application, 17 (1992) 142-144.
[21] E.F. Schubert, Light-emitting diodes Cambridge University Press, New York, (2006) 35-40.
[22] J. Schanda, Colorimetry: understanding the CIE system, John Wiley & Sons, 2007.
[23] B. Howe, A.L. Diaz, Characterization of host-lattice emission and energy transfer in $BaMgAl_{10}O_{17}:Eu^{2+}$, Journal of luminescence, 109 (2004) 51-59.
[24] G. Bizarri, B. Moine, On $BaMgAl_{10}O_{17}:Eu^{2+}$ phosphor degradation mechanism: thermal treatment effects, Journal of Luminescence, 113 (2005) 199-213.
[25] Y.F. Wang, Q.Q. Zhu, L.Y. Hao, X. Xu, R.J. Xie, S. Agathopoulos, Luminescence and Structural Properties of High Stable Si–N-Doped $BaMgAl_{10}O_{17}:Eu^{2+}$ Phosphors Synthesized by a Mechanochemical Activation Route, Journal of the American Ceramic Society, 96 (2013) 2562-2569.
[26] A. Lacanilao, G. Wallez, L. Mazerolles, P. Dubot, L. Binet, B. Pavageau, L. Servant, V. Buissette, T. Le Mercier, Structural analysis of thermal degradation and regeneration in blue phosphor $BaMgAl_{10}O_{17}:Eu^{2+}$ based upon cation diffusion, Solid State Ionics, 253 (2013) 32-38.
[27] Y.H. Wang, Z.H. Zhang, Luminescence thermal degradation mechanism in $BaMgAl_{10}O_{17}:Eu^{2+}$ phosphor, Electrochemical and Solid-State Letters, 8 (2005) H97-H99.
[28] K. Yokota, S.-X. Zhang, K. Kimura, A. Sakamoto, Eu^{2+}-activated barium magnesium aluminate phosphor for plasma displays–Phase relation and mechanism of thermal degradation, Journal of Luminescence, 92 (2001) 223-227.
[29] A.P. Jadhav, A. Pawar, C.W. Kim, H.G. Cha, U. Pal, Y.S. Kang, Effect of different additives on the size control and emission properties of $Y_2O_3:Eu^{3+}$ nanoparticles prepared through the coprecipitation method, The Journal of Physical Chemistry C, 113 (2009) 16652-16657.
[30] D. Burshtain, D. Mandler, The effect of surface attachment on ligand binding: studying the association of Mg^{2+}, Ca^{2+} and Sr^{2+} by 1-thioglycerol and 1, 4-dithiothreitol monolayers, Physical Chemistry Chemical Physics, 8 (2006) 158-164.

CHAPTER 6

RESULTS AND DISCUSSION-III

Overview

The present chapter studies the effect of co-dopants Dy^{3+}, Li^{+}, Na^{+}, K^{+} and Ca^{2+} on the morphological and optical properties of BAM:Eu^{2+} nanophosphor prepared by solution combustion synthesis method. The chapter has three sections. In the first section, the effect of trivalent rare earth ion Dy^{3+}, was studied on the morphological and optical properties of BAM:Eu^{2+} nanophosphor. The second part gives the effect of alkali metal ions whereas, the third part studies the effect of Ca^{2+} ions co-doping on the morphological and optical properties of BAM:Eu^{2+} nanophosphor. It is observed that although the morphology of all the prepared samples did not change prior to co-doping but there was an enhancement in the optical properties of the prepared nanophosphor powders. In order to measure the usefulness and applicability of the prepared phosphors, the CIE chromaticity coordinates were calculated and thermal stability was studied for all the prepared samples.

6.1. Introduction

Currently, there is an increasing interest in the rare earth ion activated aluminates owing to their excellent optical properties. BAM:Eu^{2+} is considered as the most promising blue light emitting phosphor for various display devices, W-LEDs, NUV-LEDs and lighting technology etc. but due to the poor stability of BAM:Eu^{2+} many new blue light emitting phosphors are being searched for by various researchers either by discovering new hosts or by modifying the existing phosphors through doping or co-doping. In the present chapter, the influence of co-doping or substitution of ions on the optical properties of BAM:Eu^{2+} nanophosphor is described. Co-doping is an efficient method for improving the brightness and efficiency of the phosphors with Eu^{2+} ion as an activator because Eu^{2+} emission is sensitive to the surrounding environment in the host lattice. Eu^{2+} has parity allowed $4f^6 5d^1 \rightarrow 4f^7$ electronic transition. The 5d electrons in the excited state are not properly shielded as 4f electrons in the ground state hence 5d electrons in the excited state are environment sensitive. Therefore, substitution of the ions in BAM:Eu^{2+} nanophosphor could lead to interesting optical properties.

6.2. Investigation of Dy^{3+} Sensitized BAM:Eu^{2+} Nanophosphors

In chapter 4, monophasic BAM:Eu^{2+} nanophosphors were obtained and also Eu^{2+} ion concentration in BAM was optimized for maximum photoluminescence intensity. The optimum concentration of Eu^{2+} ions in BAM host for maximum photoluminescence intensity was found to be 10 mol%. Beyond this concentration, photoluminescence intensity decreased due to concentration quenching process. In this chapter BAM:Eu^{2+} (10 mol%) was codoped with Dy^{3+} ions and its effect on the structural and optical characteristics of BAM:Eu^{2+} nanophosphor was studied. The concentration of Dy^{3+} ions was varied to obtain optimum concentration for maximum photoluminescence intensity from BAM:Eu^{2+} nanophosphors. The Dy^{3+} ion concentration was varied from 0.5 mol% to 4.0 mol%. The details of sample code have already been discussed in chapter 3 (Experimental techniques (table 3.1)). However, for simplicity, the samples with their codes are tabulated in table 6.1.

Table 6.1: Samples with their corresponding codes

S.No.	Sample	Sample Code
1.	BAM:Eu^{2+} (10%)	E10
2.	BAM:Eu^{2+} (10%) / Dy^{3+} (0.5%)	ED0.5
3.	BAM:Eu^{2+} (10%) / Dy^{3+} (1%)	ED1
4.	BAM:Eu^{2+} (10%) / Dy^{3+} (2%)	ED2
5.	BAM:Eu^{2+} (10%) / Dy^{3+} (3%)	ED3
6.	BAM:Eu^{2+} (10%) / Dy^{3+} (4%)	ED4

The results of the characterized samples are discussed below.

6.2.1. XRD Study

The phase identification and phase purity of the as-prepared samples was studied by XRD analysis. Figure 6.1 reveals the XRD patterns of samples ED2 and E10 compared with JCPDS Card No. 00-026-0163. The peaks in the patterns were indexed with JCPDS Card No. 00-026-0163 where no significant additional peaks were found indicating pure phase formation. The intense peaks of the diffraction pattern suggested that the prepared phosphors have a high degree of crystallinity. The doping and co-doping of Eu^{2+} and Dy^{3+} ions respectively did not produce any notable change in the host structure. The average crystallite size was estimated using the Debye-Scherrer equation [1]. The estimated average crystallite size for sample E10 was around 65 nm and for ED2 was nearly 58 nm. The unit cell parameters of samples E10 and ED2 nanophosphors tabulated in table 6.2 confirmed the hexagonal β-alumina structure, which crystallizes in the P 63/m m c space group. A slight decrease in the a, b and c values of ED2 phosphor was observed. This may be due to the replacement of Ba^{2+} ions (r_{Ba}^{2+} = 1.36 Å) with Dy^{3+} ions (r_{Dy}^{3+} = 0.912 Å). The decrease of unit cell parameters justifies the decrease of the crystallite size [2].

Table 6.2: Crystallite size and unit cell parameters for samples E10 and ED2

Sample Name	Crystallite Size (nm)	a (Å)	b (Å)	c (Å)
E10	65	5.63	5.63	22.68
ED2	58	5.62	5.62	22.63

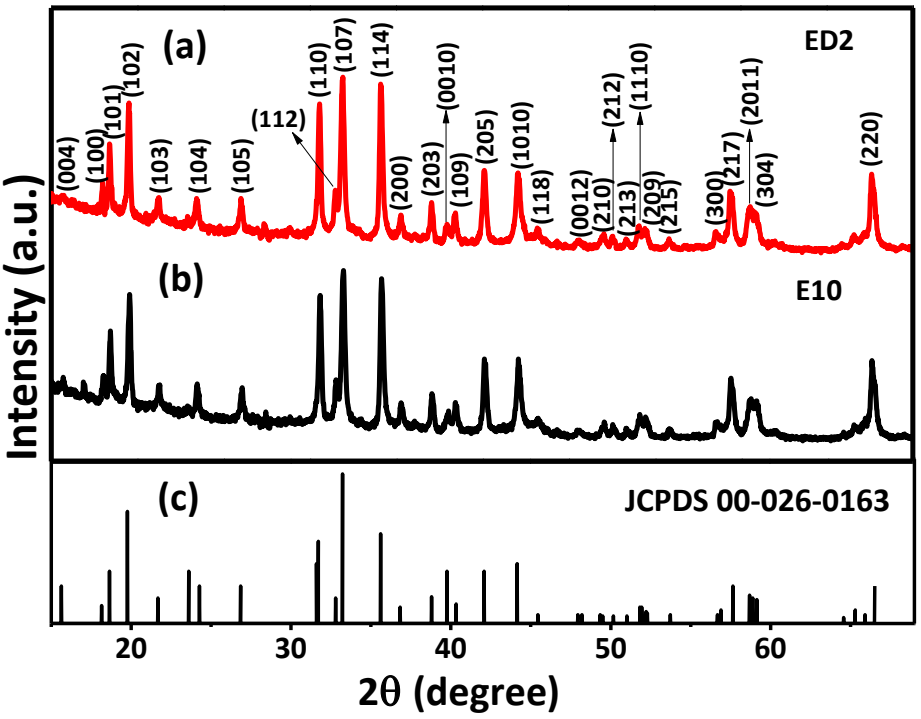

Figure 6.1: XRD patterns of samples **(a)** ED2 and **(b)** E10 compared with **(c)** JCPDS card no. 00-026-0163

6.2.2. FESEM Analysis

The morphology of the as prepared nanophosphors was examined by FESEM. FESEM images of sample E10 are exhibited in figure 6.2 (a & b). The particles appear to be a mix of multifaceted plate like and rod like morphology. The plates were roughly stacked against each other with plate length varying from 200 nm – 350 nm and plate thickness from 60 nm – 70 nm whereas the rod length was in the range 300 nm – 500 nm with rod thickness between 50 nm – 60 nm. Figure 6.2 (c & d) shows the FESEM images of ED2. Co-doping of Dy^{3+} did not bring any notable change in the morphology of sample ED2, which also has a mix of multifaceted plate like and rod like morphology. The length and thickness of the plates was between 200 nm to 300 nm and 50 nm to 60 nm respectively and that of rods varied between 350 nm to 550 nm and 70 nm to 80nm.

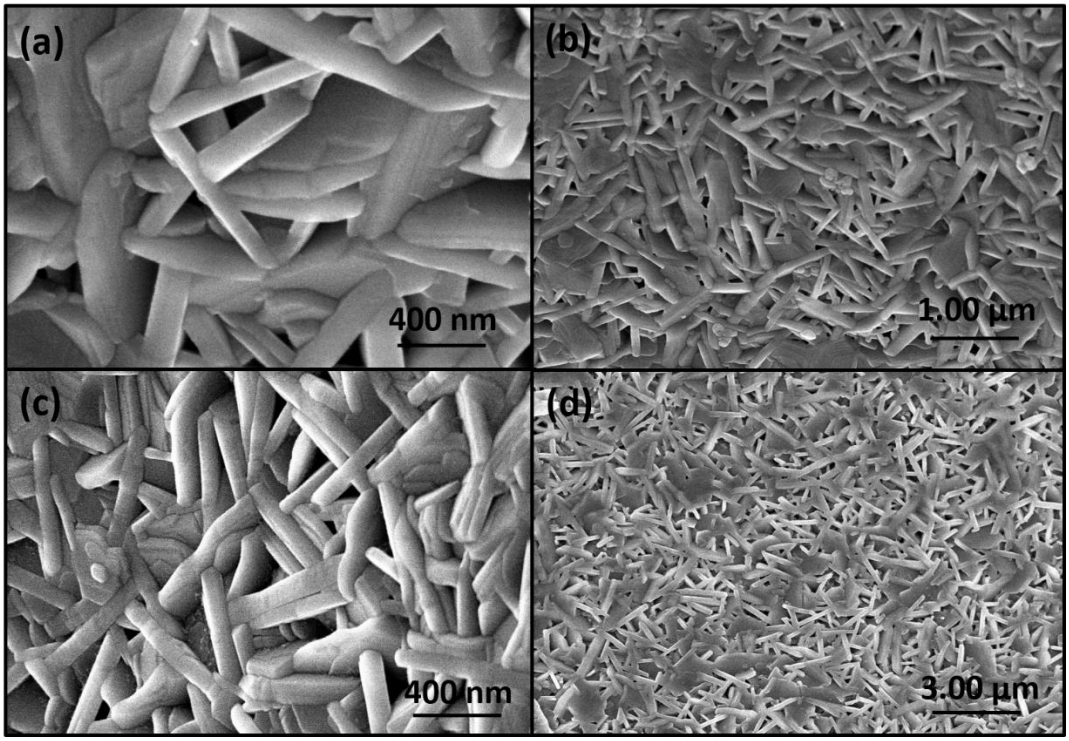

Figure 6.2: FESEM images of samples **(a & b)** E10 and **(c & d)** ED2

6.2.3. TEM Analysis

TEM images for samples E10 and ED2 are given in figure 6.3. The micrograph for the sample E10 given in figure 6.3 (a) illustrated an inter-mix of multifaceted plate like and rod like morphology. This combination of plate like and rod like morphology did not change with the co-doping of Dy^{3+} ions as seen in micrograph 6.3 (c) for sample ED2. The interplanar spacing between fringes 0.28 nm and 0.33 nm seen in figure 6.3 (b) for sample E10 correspond to the interplanar spacing of (110) and (105) planes respectively. Whereas for sample ED2 the interplanar spacing of 0.16 nm (figure 6.3(d)) correspond to (217) plane.

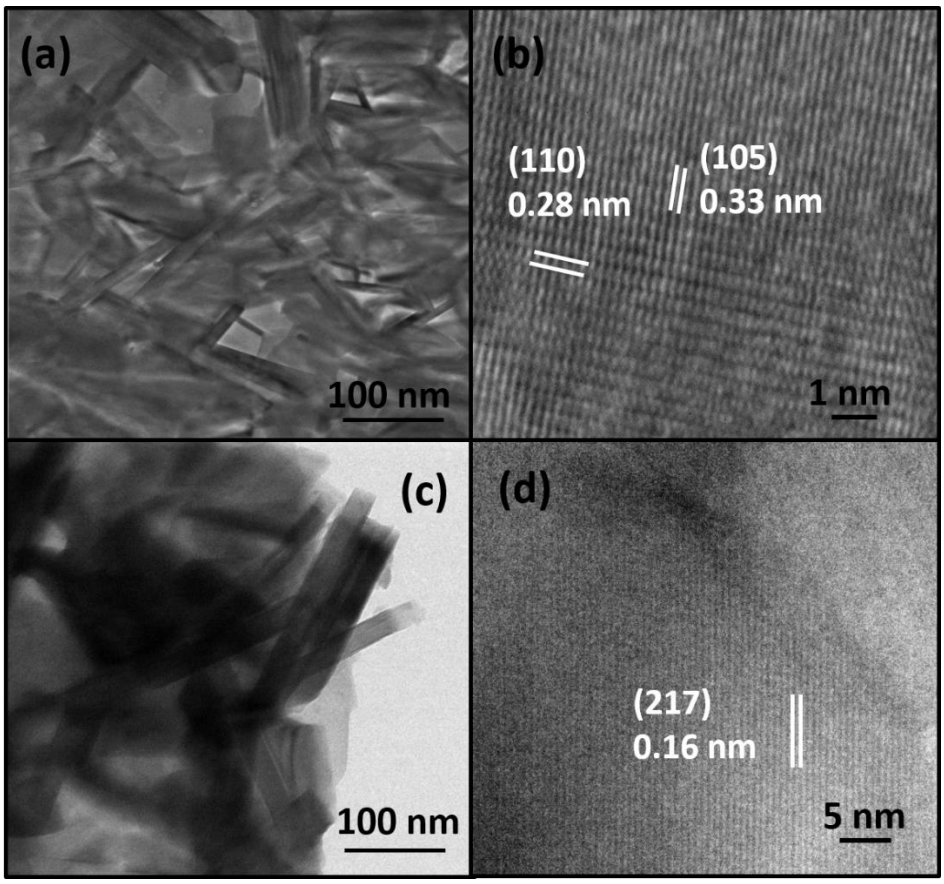

Figure 6.3: TEM images of **(a & b)** E10 and **(c & d)** ED2 nanophosphors

6.2.4. Photoluminescence Study

The photoluminescence properties of BAM:Eu^{2+} and BAM:Eu^{2+}/Dy^{3+} nanophosphors were investigated. PL excitation spectra for samples E10 and ED2 monitored at wavelength 450 nm are given in figure 6.4. Both the nanophosphors illustrated broadband with maximum peak intensity at approximately 330 nm. A small peak and a shoulder at 250 nm and 380 nm respectively were also observed, which correspond to the $4f^7 – 4f^65d^1$ electronic transitions of Eu^{2+} ions. The co-doping of Dy^{3+} ions did not affect the excitation peak maxima position. The obtained broad excitation spectra facilitate efficient absorption of long wavelength UV light [3, 4].

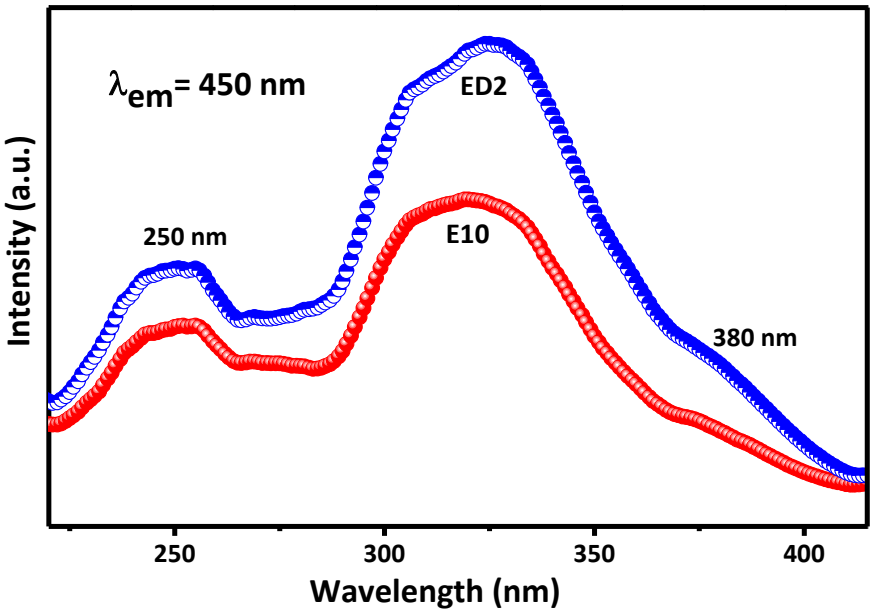

Figure 6.4: Photoluminescence excitation spectra of samples E10 and ED2

The PL emission spectra for E10 and ED2 nanophosphors excited at 330 nm are given in figure 6.5. A broadband emission peak at 450 nm was observed. Co-doping of Dy^{3+} ions did not affect the peak maxima located at 450 nm but increased the emission intensity of the phosphor. The maximum PL emission intensity was observed for 2mol% Dy^{3+} ion concentration. Beyond this concentration, PL emission intensity decreased due to concentration quenching as seen in the inset of figure 6.5. Dy^{3+} co-doping increased the photoluminescence efficiency of the phosphor by 36%. The blue emission at 450 nm is attributed to the $4f^6\ 5d^1$ to $4f^7$ electronic transitions of Eu^{2+} ions. No emission from Eu^{3+} ions in the spectral range 580 nm to 700 nm was detected, indicating complete reduction of Eu^{3+} to Eu^{2+}. Also, the characteristic Dy^{3+} emission peaks at 480 nm (bluish-green region) and 577 nm (yellow region) corresponding to f-f transitions of Dy^{3+} ions were absent [5]. Upon excitation of BAM:Dy^{3+} nanophosphor at 330 nm wavelength, as shown in figure 6.6, no emission peak was observed suggesting that Dy^{3+} ions did not act as luminescent centers in the BAM host lattice. It is clear from the literature, that Dy^{3+} ions in aluminates and silicates act as traps as they possess very high transfer energy when compared to other trivalent rare earth ions [6-10]. As Dy^{3+} emission peaks were not present in BAM:Eu^{2+}, Dy^{3+} emission spectra thus, it implies that Dy^{3+} ions act as hole or electron traps and as energy transporting media whereas, Eu^{2+} ions are the emission centers.

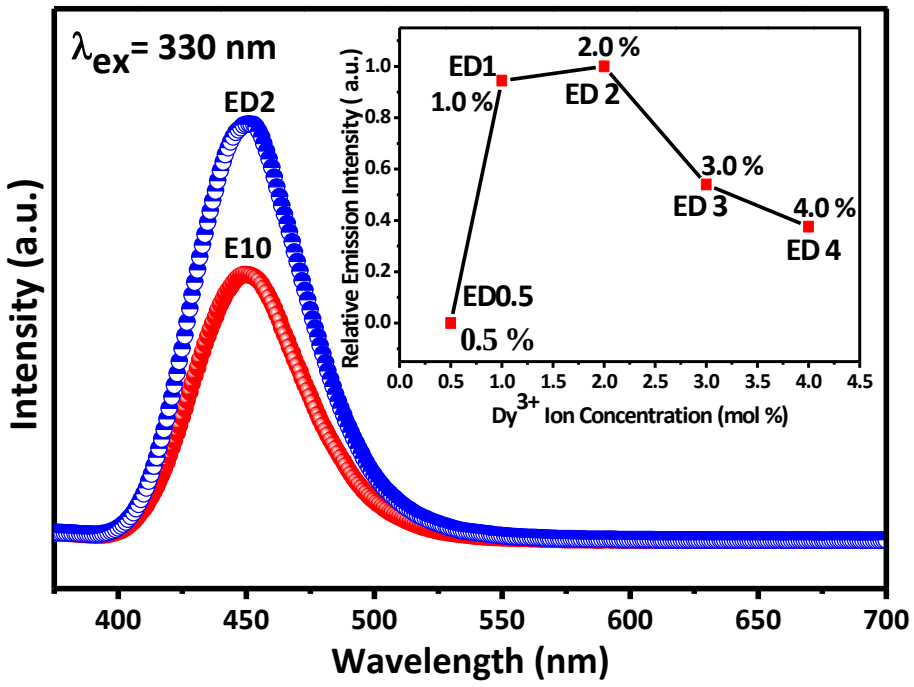

Figure 6.5: Photoluminescence emission spectra of samples E10 and ED2. Inset is the relative emission intensity of BAM:Eu^{2+}/ Dy^{3+} with varying Dy^{3+} concentration

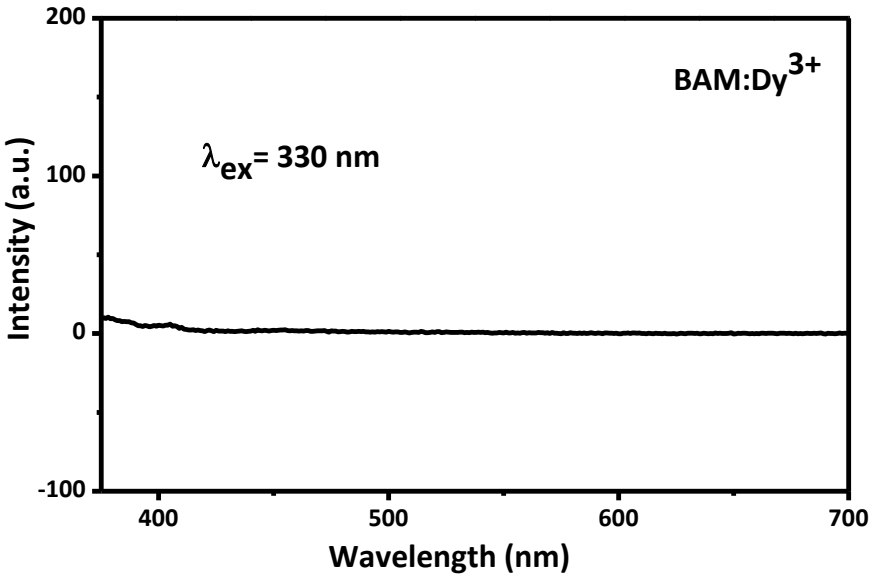

Figure 6.6: Photoluminescence emission spectrum of BAM:Dy^{3+}

6.2.4.1. Chromaticity Coordinates with Color Purity

Photoluminescent color of the samples E10 and ED2 under 330 nm excitation was characterized by Commission Internationale de I'Eclairage (CIE) chromaticity diagram. The chromaticity coordinates were calculated from the PL emission spectra of the phosphors using CIE coordinate calculator [11]. The CIE chromaticity diagram for nanophosphors E10 and ED2 are shown in figure 6.7. The corresponding CIEx and CIEy values are given in table 6.3. Dy^{3+} co-doping did not produce much change in the chromaticity coordinates. It was observed that the chromaticity coordinates for the two nanophosphors lie in the blue region and are near to the ideal blue coordinates (0.15, 0.06) [12].

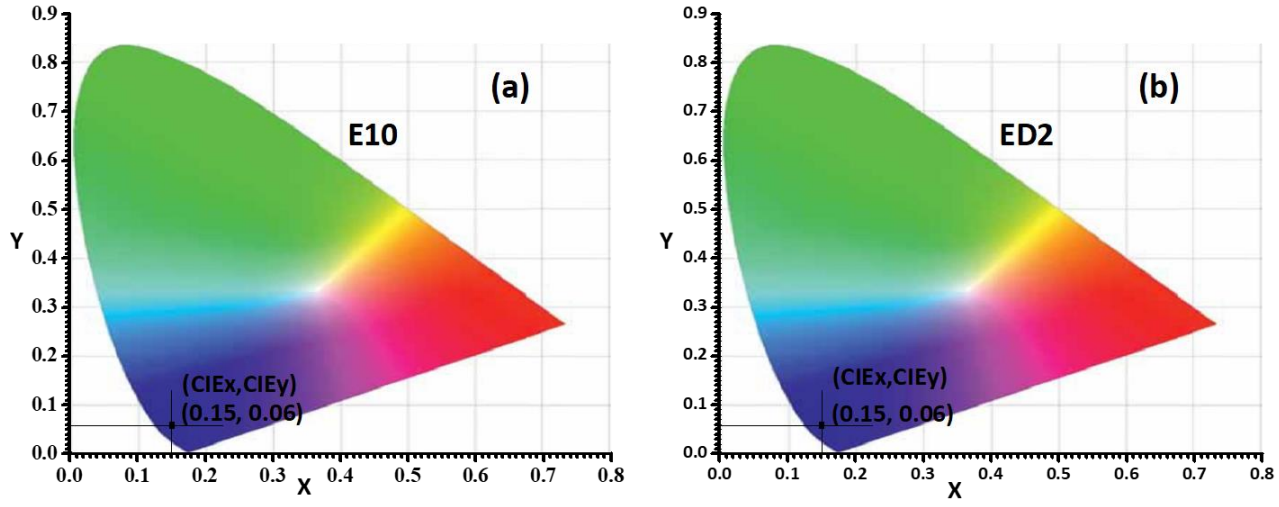

Figure 6.7: CIE chromaticity coordinate diagram of samples **(a)** E10 and **(b)** ED2

Color purity of synthesized samples was calculated using equation (6.1):

$$\textbf{Color Purity}\ (\%) = \frac{\sqrt{(x-x_i)^2 + (y-y_i)^2}}{\sqrt{(x_d-x_i)^2+(y_d-y_i)^2}}\ \textbf{X 100} \qquad (6.1)$$

where, (x, y) are the chromaticity coordinates of the sample, (x_d, y_d) represent coordinates of the dominant-wavelength point and (x_i, y_i), the coordinates of white light in CIE diagram are (0.3333, 0.3333)[13, 14]. Color purity was determined by substituting the values of (x, y), (x_i, y_i) and (x_d, y_d) in equation (6.1). Nanophosphors exhibited good color purity of about 94%.

Table 6.3: CIE coordinates and color purity of E10 and ED2 nanophosphors

Sample Name	CIEx	CIEy	Color Purity
E10	0.149	0.057	94%
ED2	0.147	0.055	94%

6.2.5. Thermoluminescence Measurement

Thermoluminescence study gives information about the naturally occurring or artificially created traps or imperfections are present in the structure of inorganic phosphors. The thermoluminescence (TL) glow curve represents the light emitted from different trapping levels in the optical bandgap of host material. Some electrons get trapped in crystal lattice imperfections. These trapped electrons are released with light emission upon heating the crystal. This emission is recorded as TL spectra called glow curve. Intensity of glow curve is related to the activation energy of trap level and trap depth can be determined [15]. Figure 6.8 exhibits TL glow curve of sample E10 and ED2 subjected to gamma ray dose of 500 Gy.

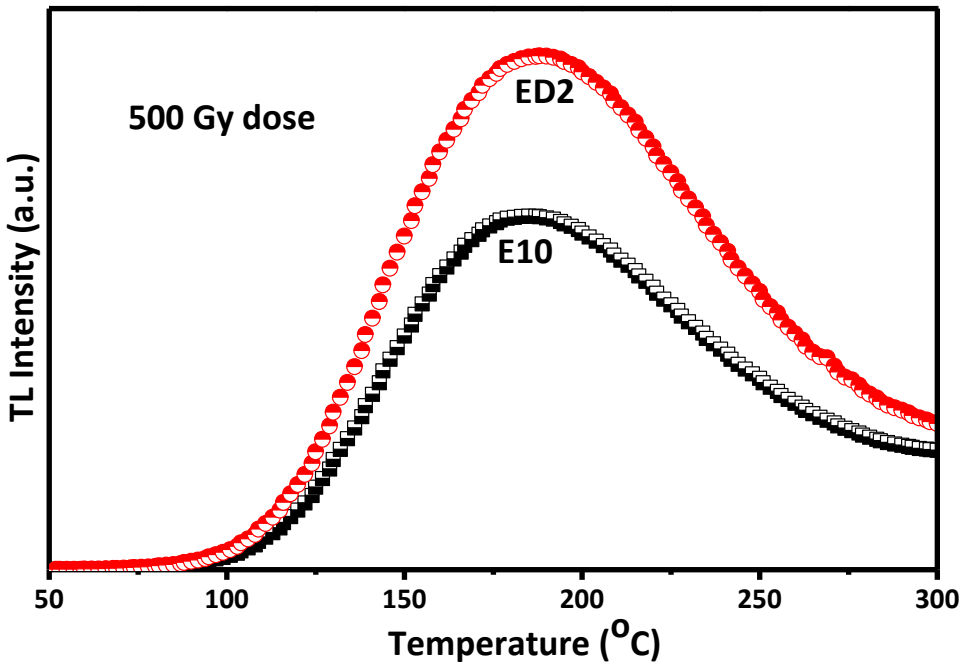

Figure 6.8: TL glow curve of samples E10 and ED2

Both the samples exhibit broad peak in TL glow curve. TL peak intensity increases with addition of Dy^{3+} ions. In BAM:Eu^{2+}, Ba^{2+} is replaced by Eu^{2+} as they have similar ionic radii but due to their different electronegativity this replacement produces traps in the host lattice. Whereas in BAM:Eu^{2+}/ Dy^{3+}, the replacement of Ba^{2+} by Dy^{3+} results in the positive charge defects in the host lattice and electronic traps are formed. Eu^{2+} in BAM:Eu^{2+}/Dy^{3+} also acts as a trap center. Upon excitation of Eu^{2+} and Dy^{3+} ions by an ionizing radiation, direct excitation from ground state to excited state occurs, which generates a large number of charge carriers i.e. holes and electrons. These free charge carriers when move to valence or conduction band, get trapped by the defects near the bottom of conduction band. Traps created by Dy^{3+} at various depths also trap electrons. Upon heating the sample, after the excitation removal, the trapped carriers are released which then recombine with Eu^{2+} leading to radiative emission [10, 15]. Therefore, the formation of trap levels by Dy^{3+} ions is responsible for the increase in TL peak intensity.

6.2.5.1. Kinetic Parameters

The trap levels determine the size, shape and intensity of the glow curves. The kinetic parameters as activation energy (E) or trap depth, order of kinetics (b), frequency factor (s) and shape factor (μ_g) associated with the glow peaks and the traps involved in the TL emission are determined by the Chen's peak shape method [16]. Shape factor, frequency factor and activation energy were calculated from the following expressions given by Chen [16].

$$\mu_g = \frac{\delta}{\omega} = \frac{T_{2-}T_m}{T_{2-}T_1} \quad (6.2)$$

$$E_\alpha = C_\alpha \left(\frac{kT_m^2}{\alpha}\right) - b_\alpha (2kT_m) \quad (6.3)$$

$$s = \frac{\beta_{HR}}{kT_m^2} \exp\left(\frac{E}{kT_m}\right) [1+ (b-1)\Delta_m]^{-1} \quad (6.4)$$

$$n_o = \omega I_m / \{\beta [2.52 + 10.2 (\mu_g - 0.42)]\} \quad (6.5)$$

$$\Delta_m = \frac{2kT_m}{E} \quad (6.6)$$

$$C_\tau = 1.51 + 3.0 (\mu_g - 0.42); b_\tau = 1.58 + 4.2 (\mu_g - 0.42) \quad (6.7)$$

$$C_\delta = 0.976 + 7.3 (\mu_g - 0.42); b_\delta = 0 \quad (6.8)$$

$$C_\omega = 0.976 + 7.3 (\mu_g - 0.42); b_\delta = 0 \quad (6.9)$$

where, $\omega = T_2 - T_1$, $\tau = T_m - T_1$ and $\delta = T_2 - T_m$.

T_m is the temperature at the maximum peak intensity of glow curve, T_1 and T_2 are the temperatures at FWHM of the maximum intensity peak, α represents τ, δ and ω. ω is the full width of glow curve, τ is width of first half on the rising side of glow curve, δ is width of second half on the falling side of glow curve as shown in figure 6.9, β_{HR} is TL heating rate and k is Boltzmann constant [17-19]. The kinetic parameters are tabulated in table 6.4.

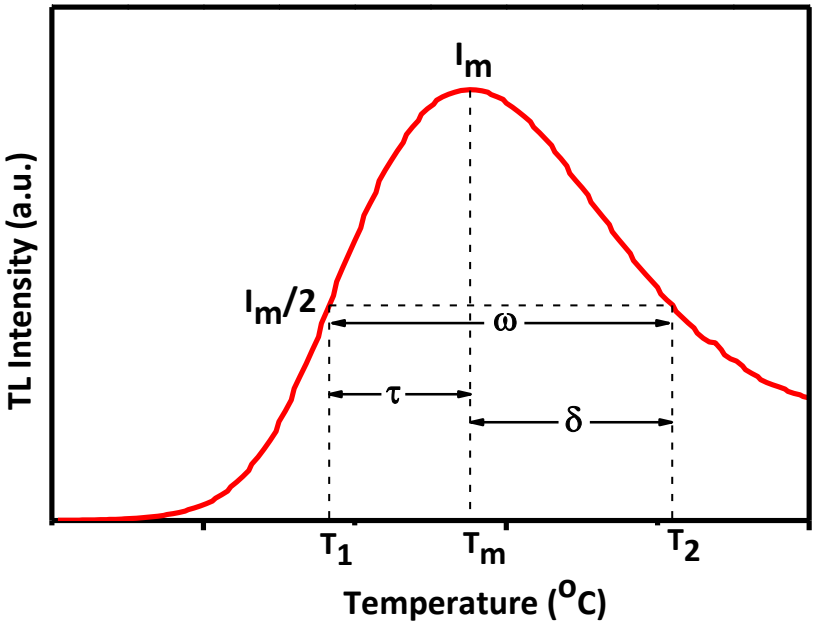

Figure 6.9: Schematic representation of peak shape method where I_m is the maximum peak intensity of the glow curve

Table 6.4: Thermoluminescence kinetic parameters of samples E10 and ED2

Sample Name	T_m (K)	Shape factor (μ_g)	Activation Energy, E(eV)	Frequency factor s (s^{-1})	Trap density n_0 (cm^{-3})
E10	458	0.61	0.66	2.6×10^6	3.4×10^9
ED2	461	0.59	0.61	6.8×10^5	5.4×10^9

The value of μ_g determines the order of kinetics (b) and differentiates between first and second order TL glow peaks. Samples possess first order kinetics if the value of μ_g is near 0.42 and second order kinetics if $\mu_g > 0.52$ [17, 20]. In the present case as observed from table 6.4, μ_g

= 0.61 for E10 and 0.59 for ED2 therefore, both the samples possess second order kinetics which means deeper traps were formed [15]. Although the TL intensity forED2 increased but the frequency factor (s) and activation energy (E) decreased. This is due to the smaller particle size of ED2, which is 58 nm for ED2 whereas, 65 nm for E10. With the decrease in particle size, surface to volume ratio and surface states or surface defects increases. Hence, the number of ions (holes and electrons) increases thus increasing the number of carriers accessible for thermoluminescence emission. As the energy required for thermostimulation i.e. the excitation of electrons from ground state to excited state through thermal energy, is not sufficiently high, so the carriers (electrons or holes) from the surface states are ionized. Thus, the carriers from the surface states are involved in the thermoluminescence process. The decrease in particle size results in the increase of surface states and ions, thus increasing the thermoluminescence emission. Furthermore, with the decrease in particle size, the electron and hole wave functions overlap effectively increasing their recombination rate. Therefore, due to these two effects, the decrease in particle size results in stronger thermoluminescence emission [21, 22]. In the present case, ED2 has smaller particle size and hence more surface defects, therefore, the trap depth or activation energy for ED2 decreased. The increase in trap density (n_o) of ED2 confirms the increase in defect states for ED2. The slight shift in T_m towards higher temperature for ED2 is due to the increase in defect states, which are influenced by particle size and the presence of dopants and codopants. Therefore, co-doping of Dy^{3+} has resulted in the formation of increased number of traps.

6.2.6. Thermal Stability Study

Thermal stability is an important aspect of phosphors, as they tend to degrade and their photoluminescence efficiency decreases when they are subjected to high temperature, approximately 600°C in air during the fabrication of displays. Among all the phosphors BAM:Eu^{2+} phosphor is the most vulnerable material in terms of degradation during panel processing [23]. To test the thermal stability of the prepared phosphors, the phosphor powders were annealed (or baked) at 600°C for 30 minutes in ambient air [24-26]. After baking, their photoluminescence spectra were recorded at 330 nm wavelength. Photoluminescence emission spectra of the baked samples E10 and ED2 in comparison to their initial emission are given in figure 6.10.

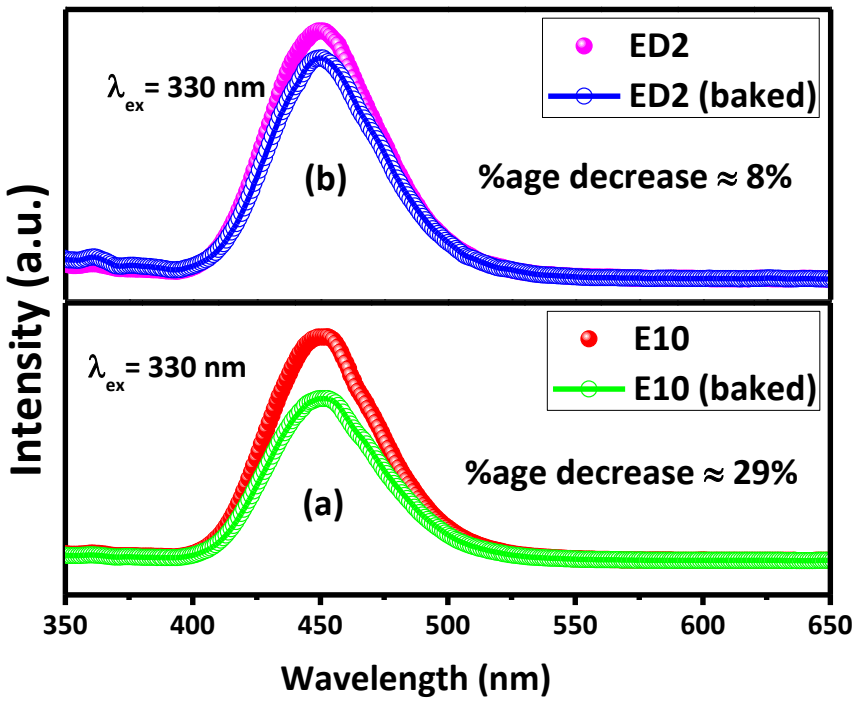

Figure 6.10: Photoluminescence emission spectra of samples **(a)** E10 (before and after baking) **(b)** ED2 (before and after baking)

It was observed that the photoluminescence emission intensity for E10 was decreased by 29% after baking whereas an inappreciable decrease of about 8% was observed for ED2 post baking. The root cause of degradation in BAM:Eu^{2+} phosphor is the oxidation of Eu^{2+} to Eu^{3+} and the creation of oxygen vacancies [24, 27-29]. Co-doping of Dy^{3+} in BAM:Eu^{2+}/ Dy^{3+} resulted in the formation of traps. These traps can capture the electrons and can also release the trapped electrons upon thermal activation. Thus the oxidation degree of Eu^{2+} to Eu^{3+} and the oxygen vacancies are decreased resulting in increased thermal stability [7, 30]. As a marginal decrease of 8% was observed in the photoluminescence emission of BAM:Eu^{2+}/ Dy^{3+} nanophosphor after baking at 600°C for 30 minutes, it indicated that Dy^{3+} co-doping in BAM:Eu^{2+} had significantly improved the thermal stability of BAM:Eu^{2+}/ Dy^{3+} nanophosphor. Therefore, BAM:Eu^{2+}/ Dy^{3+} nanophosphor is thermally stable as compared to BAM:Eu^{2+}.

6.3. Effect of Alkali Metal Ions on the Morphological and Optical Properties of BAM:Eu^{2+} Nanophosphor

The co-doping of trivalent rare earth ion (Dy^{3+}) in BAM:Eu^{2+} matrix helped in procuring blue light-emitting phosphor with high luminescence efficiency and high thermal stability. In the present section, the effect of co-doping of alkali metal ions (or monovalent ions) K^+, Na^+, and Li^+ on the morphological and optical characteristics of BAM:Eu^{2+} nanophosphor is presented. The Eu^{2+} ion concentration was fixed at 10 mol% and the molar concentration of Li^+, Na^+, and K^+ ions was varied separately in BAM:Eu^{2+} matrix to obtain optimum concentration for maximum photoluminescence intensity from BAM:Eu^{2+} nanophosphors. The molar concentration of Li^+ ions was varied from 0.005 mol% to 0.03 mol%, for Na^+ ions the variation was from 0.01 mol% to 0.04 mol% and for K^+ ions the molar concentration was varied from 0.01 mol% to 0.04 mol%. The codes to the prepared samples are discussed in chapter 3 (Experimental techniques (table 3.1)). However, the details of the prepared samples for this section are briefly given below in table 6.5.

Table 6.5: Samples with their corresponding codes

S.No.	Sample Name	Concentration (mol %)	Sample Code
1.	BAM:Eu^{2+}	Eu (10%)	E10
2.	BAM:Eu^{2+}/ Li^+	Eu (10), Li (0.005, 0.01, 0.02, 0.03)	EL05, EL1, EL2, EL3
3.	BAM:Eu^{2+}/ Na^+	Eu (10), Na (0.01, 0.02, 0.03, 0.04)	EN1, EN2, EN3, EN4
4.	BAM:Eu^{2+}/ K^+	Eu(10), K (0.01, 0.02, 0.03, 0.04)	EK1, EK2, EK3, EK4

The results of the characterized samples are discussed below.

6.3.1. XRD Study

Phase purity and the identification of phase for the prepared samples was checked by XRD analysis. The XRD patterns of samples E10, EL1, EN2 and EK3 are illustrated in figure 6.11. The peaks are labeled with their corresponding (hkl) values. Peaks matched well with JCPDS card no. 00-026-0163 which corresponds to the hexagonal β-alumina structure with P 63/m m c space group. No secondary peak was observed confirming the formation of pure phase. Absence of any additional peak due to dopant and co-dopants clearly suggested that dopant and co-dopants are incorporated well in host lattice. Also, the dopant and co-dopants did not induce any notable change in the crystal structure. The average crystallite size was estimated using Debye-Scherrer

equation [1]. The estimated average crystallite size and the unit cell parameters for the sample E10, EL1, EN2 and EK3 are tabulated in table 6.6. A slight decrease in the a, b and c values for samples EL1 and EN2 was observed. This may be attributed to the smaller ionic radius of Li^+ ions (r_{Li^+} = 0.76 Å) and Na^+ ions (r_{Na^+} = 1.02 Å). As the ionic radius of K^+ ions (r_{K^+} = 1.38 Å) is comparable to ionic radius of Ba^{2+} ions ($r_{Ba^{2+}}$ = 1.36 Å) therefore the a, b and c values of EK3 are nearly the same as that for E10. The variation in unit cell parameters justifies the crystallite size variation of the powder samples [2, 31].

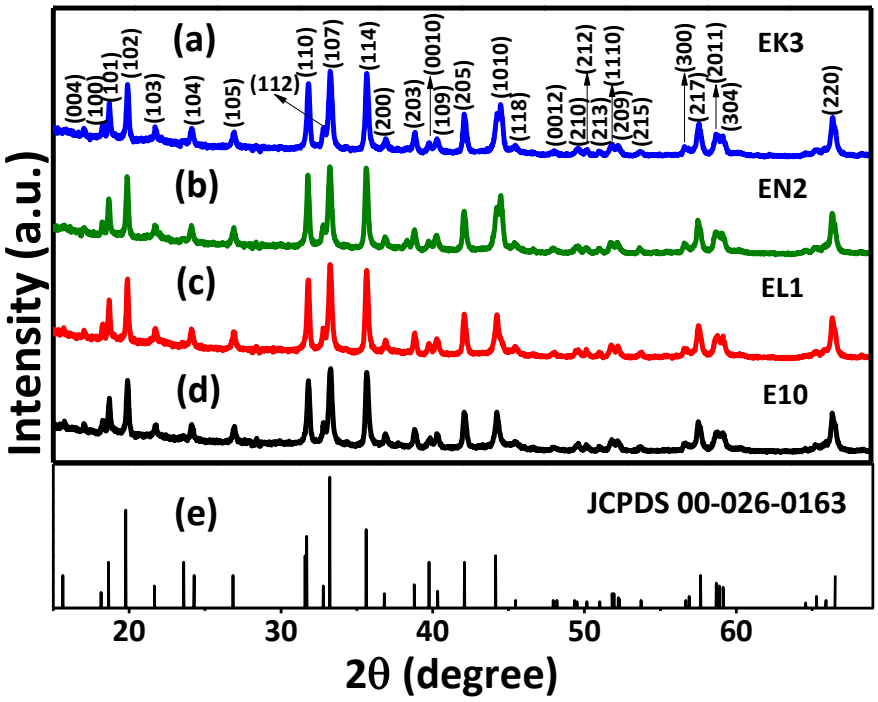

Figure 6.11: XRD patterns of samples **(a)** EK3 **(b)** EN2 **(c)** EL1 **(d)** E10 compared with **(e)** JCPDS card no. 00-026-0163

Table 6.6: Crystallite size and unit cell parameters for samples E10, EL1, EN2 and EK3

Sample Name	Crystallite Size (nm)	a (Å)	b (Å)	c (Å)
E10	65	5.63	5.63	22.68
EL1	55	5.61	5.61	22.57
EN2	59	5.62	5.62	22.63
EK3	64	5.63	5.63	22.66

6.3.2. FESEM Analysis

Surface morphology of the synthesized nanophosphor powders was investigated through FESEM study. FESEM images of the obtained samples are exhibited in figure 6.12. The images for sample E10 (figure 6.12 (a & b)) clearly indicated that the morphology was a mix of multifaceted plate like and rod like morphology. The length of the plates varied between 200 nm to 350 nm and plate thickness between 60 nm to 70 nm. The rod length was between 300 nm to 500 nm with rod thickness varying between 50 nm to 60 nm. Li^+ ions co-doping did not change the mix morphology of multifaceted plate like and rod like morphology (figure 6.12 (c & d)). The plate length for EL1 was within the range of 200 nm to 300 nm with plate thickness in the range 35 nm to 50 nm. The rod length was in the range of 250 nm to 450 nm and rod thickness varied from 49 nm to 50 nm. Similarly, Na^+ and K^+ co-doping also did not alter the mix morphology of multifaceted plate like and rod like morphology. The FESEM images of EN2 and EK3 are given in figure 6.12 (e & f) and figure 6.12 (g & h) respectively. The plate length for sample EN2 lied between 200 nm to 400 nm and plate thickness between 50 nm to 60 nm. The rod length for the same was in the range 300 nm to 400 nm with rod thickness is 40 nm to 60 nm range. Whereas, for sample EK3, the plate length lied in the range 400 nm to 600 nm with plate thickness between 50 nm to 80 nm and rod length varying between 500 nm to 600 nm with rod thickness in the range 70 nm to 80 nm. For all the samples the plates and rods were roughly stacked against each other.

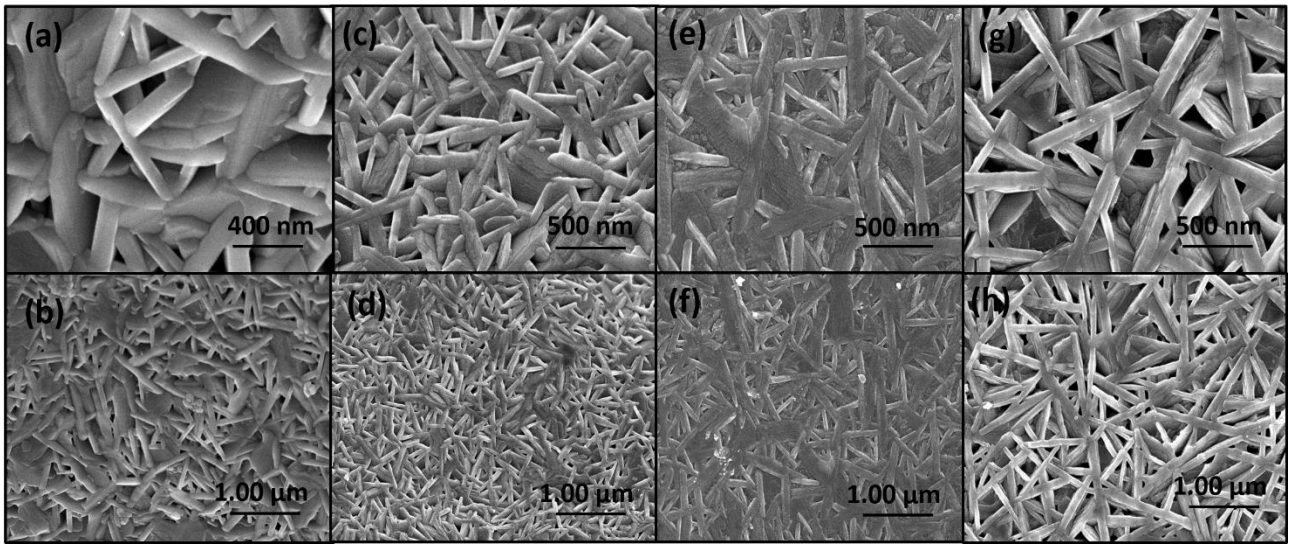

Figure 6.12: FESEM images of **(a & b)** E10 **(c & d)** EL1 **(e & f)** EN2 and **(g & h)** EK3 samples

6.3.3. TEM Analysis

TEM images for samples E10, EL1, EN2 and EK3 are shown in figure 6.13. The TEM micrograph for sample E10 as shown in figure 6.13 (a) illustrated a combination of multifaceted plate like and rod like morphology. This inter-mix of plate like and rod like morphology did not change with the co-doping of alkali metal ions (K^+, Na^+ and Li^+) as seen in micrographs 6.13 (c, e & g) for samples EL1, EN2 and EK3 respectively. The results are in good agreement with FESEM study. The interplanar spacing between lattice fringes 0.28 nm and 0.33 nm seen in figure 6.13 (b) for sample E10 correspond to the interplanar spacing of (110) and (105) planes respectively. For samples EL1, EN2 and EK3 the lattice fringes of 0.16 nm, 0.22 nm and 0.24 nm respectively were observed as seen in figure 6.13 (d, f & g) for samples EL1, EN2 and EK3 respectively. These lattice fringes of 0.16 nm, 0.22 nm and 0.24 nm correspond to the planes (217), (109) and (200) respectively and confirm the crystalline phase of the prepared nanophosphors.

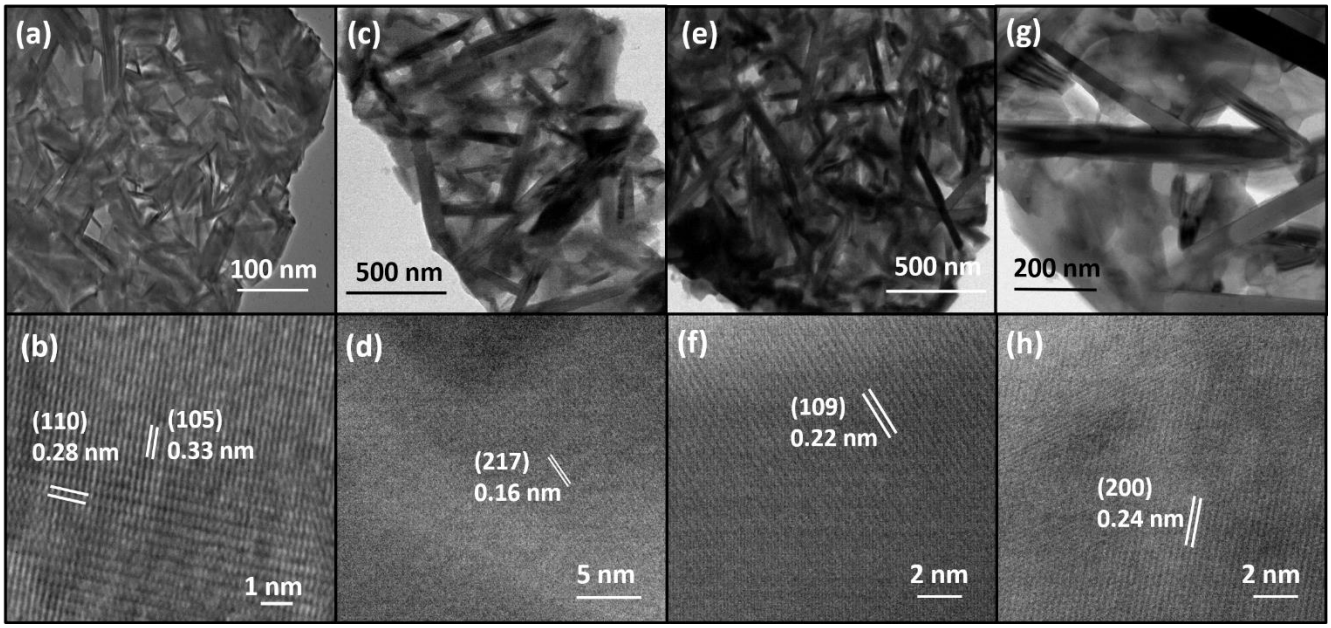

Figure 6.13: TEM images of samples **(a & b)** E10 **(c & d)** EL1 **(e & f)** EN2 and **(g & h)** EK3

6.3.4. UV-Vis Spectroscopic Analysis

UV- Visible spectroscopy provides an understanding of different electronic band structures and transitions. Upon interaction of UV/vis/NIR electromagnetic radiation with the materials, four possible outcomes are: the radiation gets absorbed, reflected, transmitted or scattered. When ultraviolet radiation is absorbed, then the excitation of electrons, both in atoms and molecules from lower energy level to higher energy level occurs. The material for which the analysis cannot be done using transmission measurements, reflectance spectroscopy is used. Optical properties of the prepared samples were studied by measuring the diffused reflectance of the samples and from it, the bandgap of the synthesized nanophosphors was determined by Kubelka-Munk method which is given by the following equation [32, 33]:

$$\boldsymbol{F(R)} = \frac{\boldsymbol{(1-R)^2}}{\boldsymbol{2R}} \tag{6.10}$$

Where F(R) is Kubelka-Munk function and R is absolute reflectance of the sample. When the rising section of $[h\upsilon F(R)]^2$ is extrapolated to the abscissa at zero F(R), then it yields the energies for the bandgap. The plots for the $(hv - (hvF(R_\infty))^2)$ and the respective tangent, are depicted for the E10, EL1, EN2 and EK3 samples in figure 6.14. The bandgap energies were obtained from the intersection point of the tangent to the plotted curve point with the horizontal axis (hv axis). The bandgap values are in the order of EK3 (E_g = 5.32 eV) > E10 (E_g = 5.3 eV)> EN2(E_g = 5.26 eV) > EL1(E_g = 5.22 eV). It was observed that upon lithium and sodium doping, the bandgap shifts towards lower energies. This could be attributed to the fact that lithium and sodium affected the localized region width of valence and conduction bands by developing several optically active sub-levels across the bandgap, thereby decreasing the bandgap [34, 35].

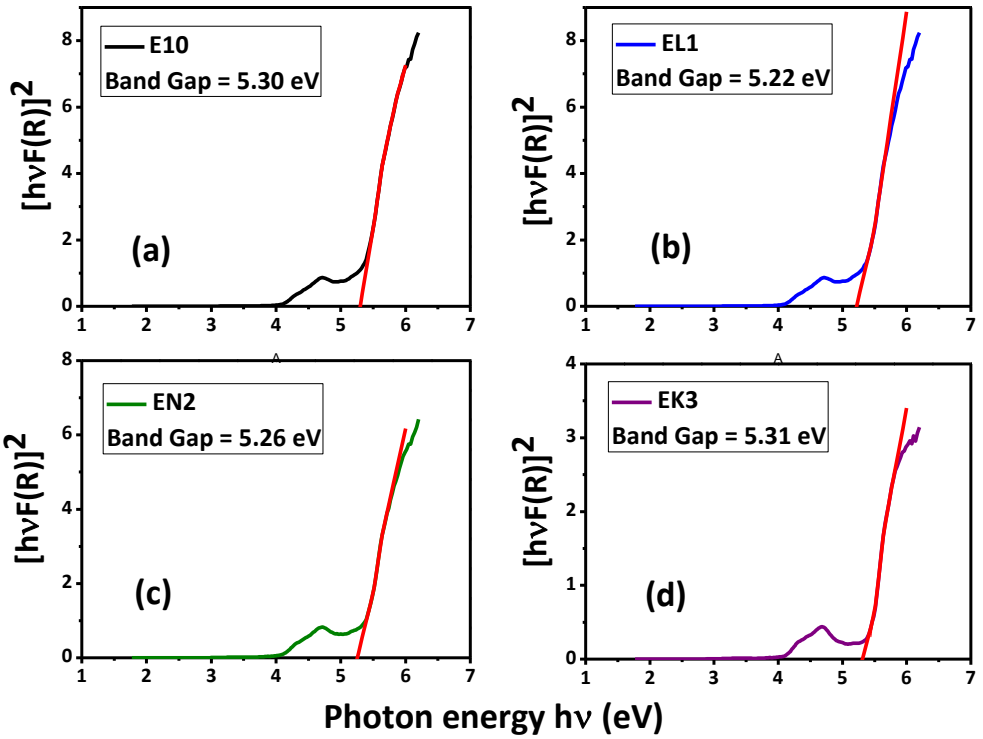

Figure 6.14: Kubelka-Munk plots for band gap calculation of samples **(a)** E10 **(b)** EL1 **(c)** EN2 **(d)** EK3

6.3.5. Photoluminescence Study

Optimum co-doping concentration of Li^+, Na^+, and K^+ was determined. Figure 6.15 shows the relative emission intensity for varying concentration of Li^+, Na^+, and K^+ in BAM:Eu^{2+}/ Li^+/ Na^+/ K^+ individually. Photoluminescence emission intensity increased with the increase in doping concentration of Li^+, Na^+, and K^+. The maximum photoluminescence enhancement for K^+, Na^+, and Li^+ co-doping in BAM:Eu^{2+} was achieved at 0.01 mol%, 0.02 mol% and 0.03 mol% respectively. Beyond this concentration, photoluminescence intensity decreased due to concentration quenching. Photoluminescence excitation and emission spectra for samples E10, EL1, EN2 and EK3 are given in figure 6.16 (a & b) respectively. The photoluminescence excitation spectrum was recorded at 450 nm. Excitation spectra for all the phosphors exhibited broadband from 280 nm to 440 nm. The excitation maxima at approximately 330 nm and a small shoulder at 380 nm was observed. These peaks were due to the $4f^7 - 4f^65d^1$ electronic transitions of Eu^{2+} ions. The co-doping of Li^+, Na^+, and K^+ ions did not affect the excitation peak maxima position however, the FWHM of the excitation bands increased with the alkali metal ion co-doping. The maximum

enhancement in FWHM of excitation band was achieved for Li^+ co-doping. The FWHM values for the excitation band of samples EL1, EN2, EK3 and E10 are 72 nm, 67 nm, 63 nm and 60 nm respectively. The ionic radius of the alkali metal ions is of the order of Li (r_{Li^+} = 0.76 Å) < Na (r_{Na^+} = 1.02 Å) < K (r_{K^+} = 1.38 Å). As the alkali metal ions have smaller ionic radius, therefore, they diffuse into the host matrix and change the local symmetry and lattice environment around the luminescent center which affects the crystal field splitting around lanthanide ions [36, 37]. More the crystal field splitting more is the expansion of excitation band. As Li^+ ion has least ionic radius so it easily diffuses in the host matrix therefore, crystal field splitting and hence FWHM of excitation band is more for sample EL1 followed by EN2 and EK3. The increase in the breadth of the excitation band enhances the absorption of NUV light making the phosphors efficient for NUV-LEDs [37].

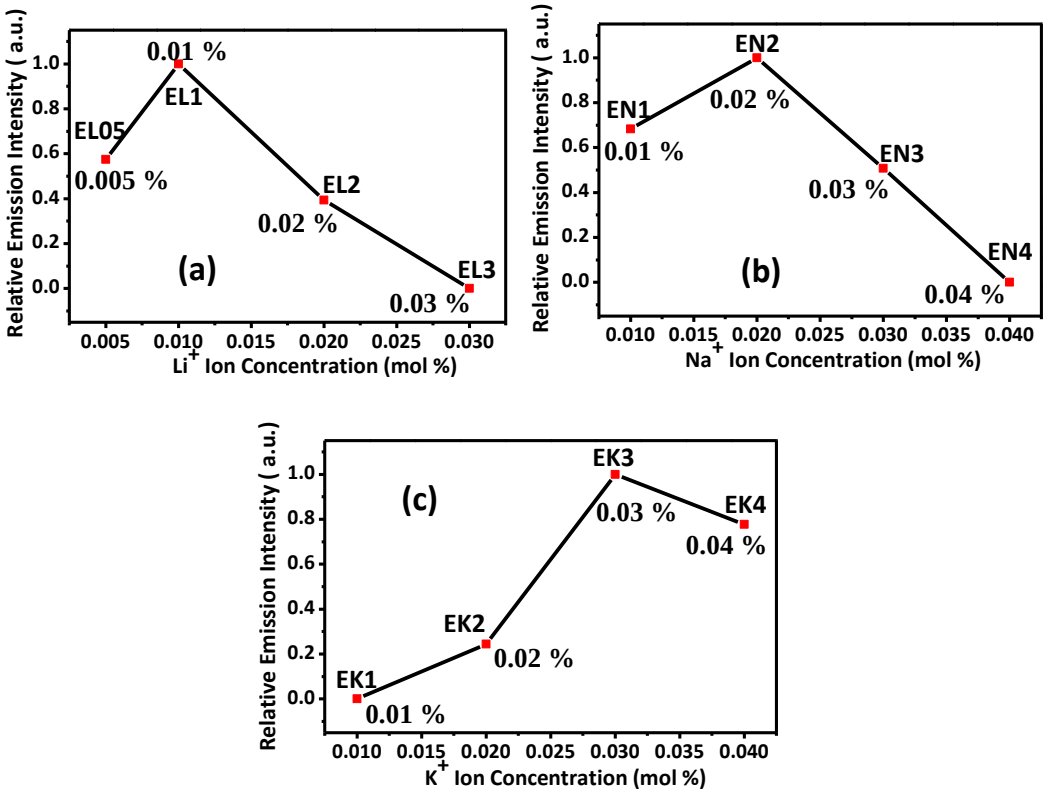

Figure 6.15: Relative emission intensity of **(a)** BAM:Eu^{2+}/ Li^+ with varying concentration of Li^+ ions **(b)** BAM:Eu^{2+}/ Na^+ with varying concentration of Na+ ions **(c)** BAM:Eu^{2+}/ K^+ with varying concentration of K^+ ions

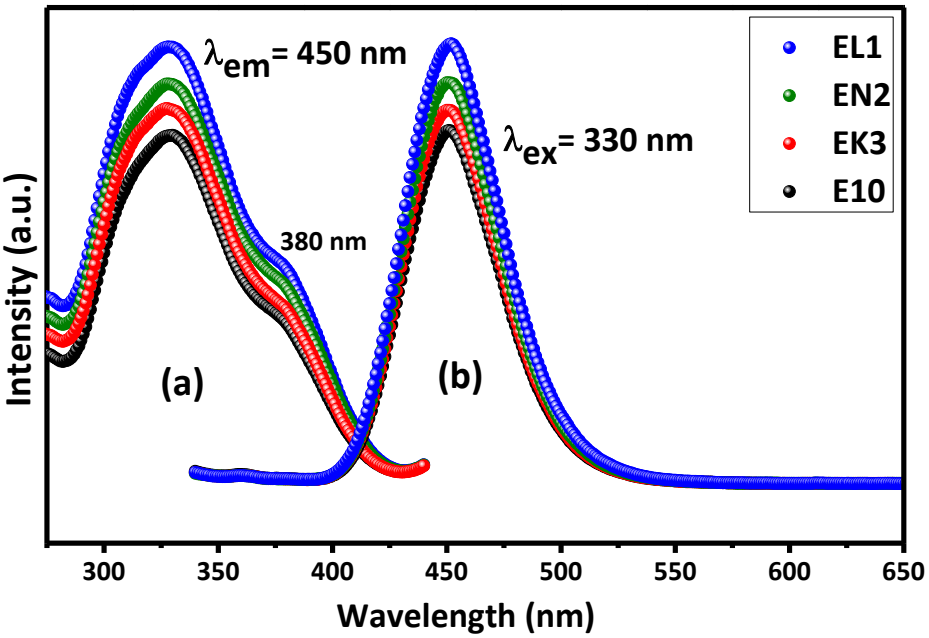

Figure 6.16: Photoluminescence **(a)** excitation spectra and **(b)** emission spectra of E10, EL1, EN2 and EK3 samples

The photoluminescence emission spectrum was recorded at 330 nm wavelength. A broadband emission was observed peaking at 450 nm due to the $4f^6 5d\text{-}4f^7$ electronic transitions of Eu^{2+} ions. Alkali metal co-doping did not affect the emission range and the peak maxima at 450 nm but increased the photoluminescence emission intensity of nanophosphors. The maximum increase in the photoluminescence emission intensity was observed for Li^+ co-doping. The order of photoluminescence emission intensity with alkali metal ion co-doping is $Li^+ > Na^+ > K^+$. The percentage increase for Li^+, Na^+, and K^+ co-doping is 20%, 11% and 5% respectively. When $Li^+/Na^+/K^+$ ions replace Ba^{2+} ions, the replacement is nonequivalent. Two monovalent ions will replace one divalent Ba^{2+} ion forming oxygen vacancies and defects. It has been reported that the formation of defects (oxygen vacancies) result in the enhancement of photoluminescence emission intensity [38, 39]. The oxygen vacancies formed at the surface of nanocrystals decrease the luminescence quenching centers thereby enhancing the photoluminescence emission intensity. As concentration of monovalent ions is increased further, the oxygen vacancies in the host lattice increase substantially and luminescence is quenched [40]. Owing to the least ionic radius of the Li^+ ions their diffusion is more in the host lattice. As the electronegativity of Li^+ ions is more therefore the excess Li^+ ions act as charge compensator hence increasing the

luminescence efficiency [31]. The electronegativity order for alkali metal ions is $Li^+ > Na^+ > K^+$ hence Li^+ ions perform better as charge compensators. In addition to this, the increased crystal field splitting for EL1 as evidenced from the excitation spectra and the smaller bandgap of EL1 (E_g = 5.22 eV) lead to the maximum photoluminescence emission intensity for EL1 followed by EN2 and EK3. Therefore, Li^+ ion co-doping gave the best result in terms of photoluminescence efficiency.

6.3.5.1. Chromaticity Coordinates with Color Purity

Photometric characteristics of the prepared nanophosphors were studied by calculating the CIE (Commission Internationale de l'Eclairage) coordinates and color purity. Figure 6.17 (a, b, c & d) shows the CIE chromaticity coordinate diagram for samples E10, EL1, EN2 and EK3 respectively. The CIE chromaticity coordinates for all the four samples were approximately the same and did not vary much with the co-doping of alkali metal ions. The CIE coordinates are near to the ideal blue coordinates (0.15, 0.06) [12]. The CIE coordinates and the color purity values are given in table 6.7. Color purity of the prepared samples was calculated using equation (6.11) and is given by:

$$\textbf{Color Purity}\ (\%) = \frac{\sqrt{(x-x_i)^2+(y-y_i)^2}}{\sqrt{(x_d-x_i)^2+(y_d-y_i)^2}} \times 100 \qquad (6.11)$$

where, (x, y) are the chromaticity coordinates of the sample, (x_i, y_i) = (0.3333, 0.3333), are the chromaticity coordinates of white light in the CIE diagram and (x_d, y_d) represents the chromaticity coordinates of dominant-wavelength point [13]. Substituting the values of (x, y), (x_i, y_i) and (x_d, y_d) to Eq. (6.11), color purity was calculated. Color purity of all the prepared samples was approximately 94%. Therefore the obtained phosphors exhibited good color purity with CIE coordinates near to ideal blue coordinates. Hence, co-doping of alkali metal ions in BAM:Eu^{2+} was beneficial in obtaining phosphors with good photoluminescence efficiency.

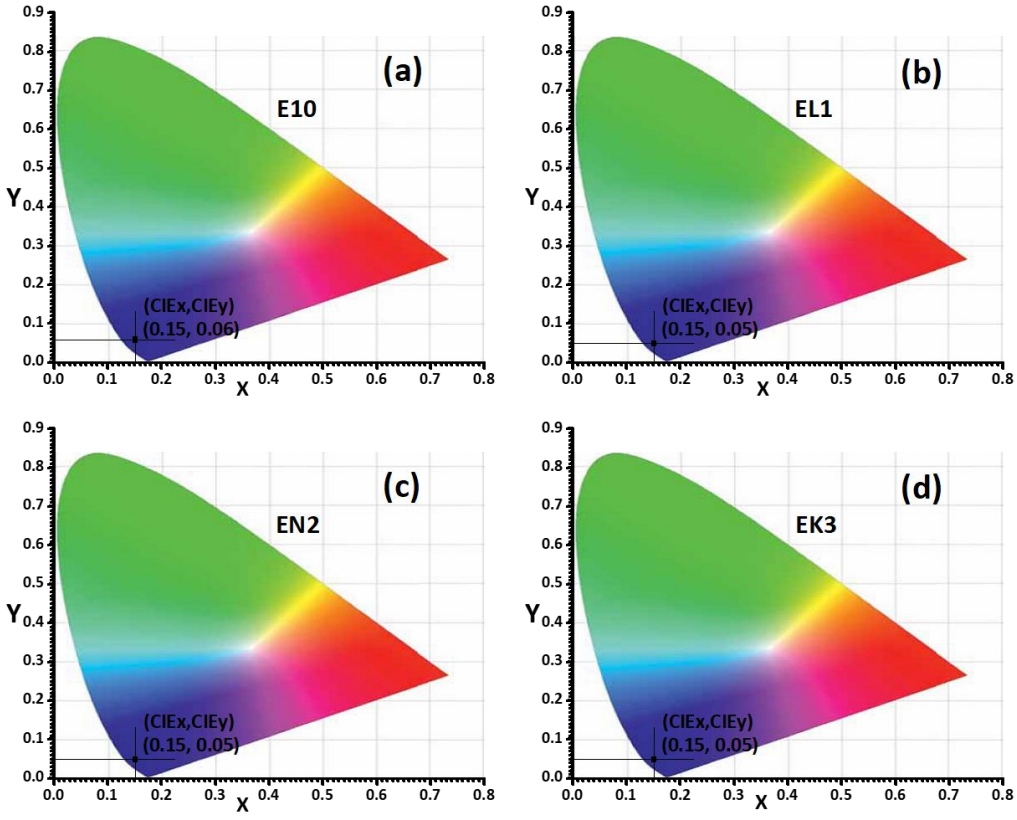

Figure 6.17: CIE chromaticity coordinate diagram for samples **(a)** E10 **(b)** EL1 **(c)** EN2 and **(d)** EK3

Table 6.7: CIE coordinates and color purity of samples E10, EL1, EN2 and EK3

Sample Name	CIEx	CIEy	Color Purity
E10	0.149	0.057	94%
EL1	0.146	0.052	94%
EN2	0.146	0.053	94%
EK3	0.146	0.054	94%

6.3.6. Thermal Stability Study

The prime application of phosphors is in the display devices. During the fabrication of the display devices, they are subjected to a high temperature of approximately 600°C. Processing at this temperature degrades the photoluminescence efficiency of the phosphors by deteriorating the brightness and decreasing the color purity of the phosphors [41]. Therefore, to check the stability of the phosphors under this thermal treatment the prepared nanophosphors were

annealed at 600°C for 30 minutes in ambient air [24, 25]. The photoluminescence emission spectra of the obtained annealed or baked phosphors were recorded at 330 nm wavelength. The corresponding photoluminescence emission spectra for the baked samples in comparison to their initial emission is given in figure 6.18 (a, b, c & d).

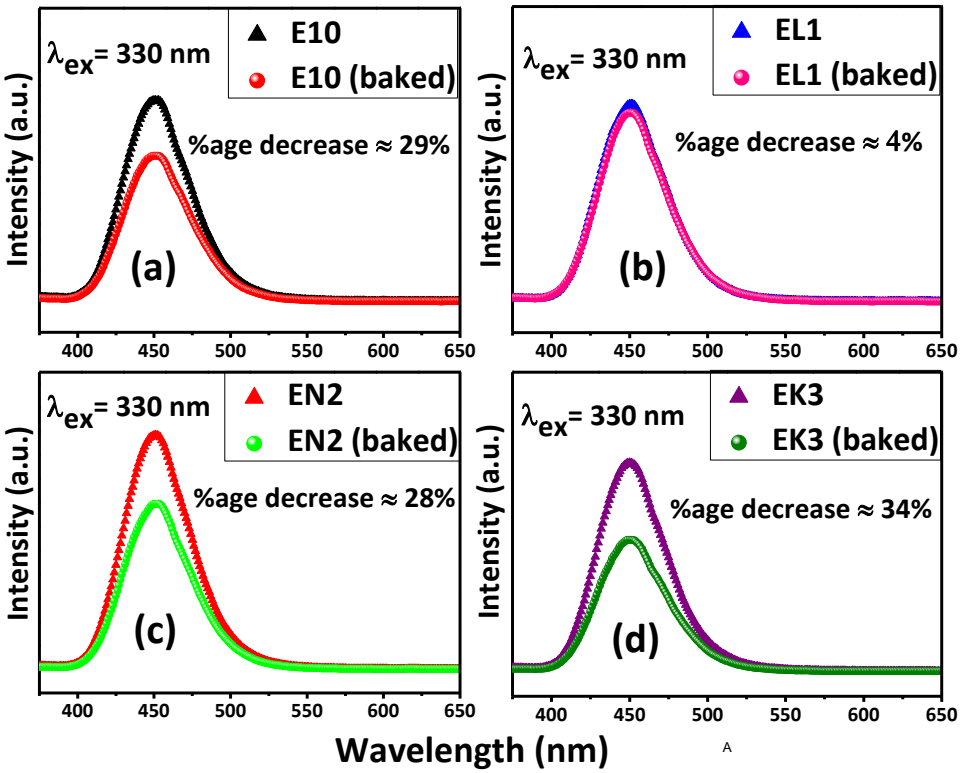

Figure 6.18: Photoluminescence emission spectra of samples **(a)** E10 (before and after baking) **(b)** EL1 (before and after baking) **(c)** EN2 (before and after baking) **(d)** EK3 (before and after baking)

Photoluminescence emission intensity for all the samples decreased after heat treatment. BAM:Eu^{2+} is the most vulnerable material in terms of thermal degradation. The main cause of its degradation of photoluminescent properties is the oxidation of Eu^{2+} to Eu^{3+} and the diffusion of cations (Ba^{2+}, Eu^{2+}, Mg^{2+}, Al^{3+}) in the inter slabs of the β-alumina structure with the creation of oxygen vacancies [24, 27, 29]. Least decrement in the photoluminescence emission intensity was observed for Li^{+} ion co-doping. Li^{+} ions are more electronegative therefore, the Li – O bond length would be shorter than Na – O and K – O bond length hence decreasing the lattice parameters [37]. Since the spinel block is compacted with the Li^{+} ions, therefore, the movement of Eu^{2+} ions and the adsorption of oxygen atoms is hindered. Also by acting as a charge compensator, the

degree of oxidation of Eu^{2+} decreases hence increasing the thermal stability [40]. Thus, Li^{+} ion co-doping was effective in improving the photoluminescence efficiency and thermal stability of BAM:Eu^{2+} nanophosphor.

6.4. Morphological and Optical Study of Ca^{2+} Doped BAM:Eu^{2+} Nanophosphor

In the present section, the effect of co-doping of divalent calcium ions Ca^{2+} on the morphological and optical characteristics of BAM:Eu^{2+} nanophosphor is presented. The Eu^{2+} ion concentration was fixed at 10 mol% and the molar concentration of Ca^{2+} ions was varied in BAM:Eu^{2+} matrix to obtain optimum concentration for maximum photoluminescence intensity from BAM:Eu^{2+} nanophosphors. The molar concentration of Ca^{2+} ions was varied from 2 mol% to 8 mol%. The codes to the prepared samples are discussed in chapter 3 (Experimental techniques (table 3.1)). However, for simplicity, the details of the prepared samples for this section are tabulated in table 6.8.

Table 6.8: Samples with their corresponding codes

S.No.	Sample Name	Concentration (mol %)	Sample Code
1.	BAM:Eu^{2+}	Eu (10%)	E10
2.	CaBAM:Eu^{2+}	Eu (10), Ca (2, 4, 6, 8)	EC2, EC4, EC6, EC8

The results of the characterized samples are discussed below.

6.4.1. XRD Study

XRD patterns of samples EC4 and E10, indexed and compared with JCPDS Card No. 00-026-0163 are given in figure 6.19. XRD patterns matched well with JCPDS Card No. 00-026-0163 confirming the hexagonal β-alumina structure with P 63/m m c space group for the prepared samples. The absence of any secondary peak indicated the formation of a pure phase of the prepared phosphors. The doping and co-doping of Eu^{2+} and Ca^{2+} had almost no effect on the BAM phase composition. The intense peaks of the XRD patterns suggested a high degree of crystallinity for the prepared samples. The average crystallite size estimated from Debye Scherrer equation [1] for samples E10 and EC4 was approximately 65 nm and 61 nm respectively.

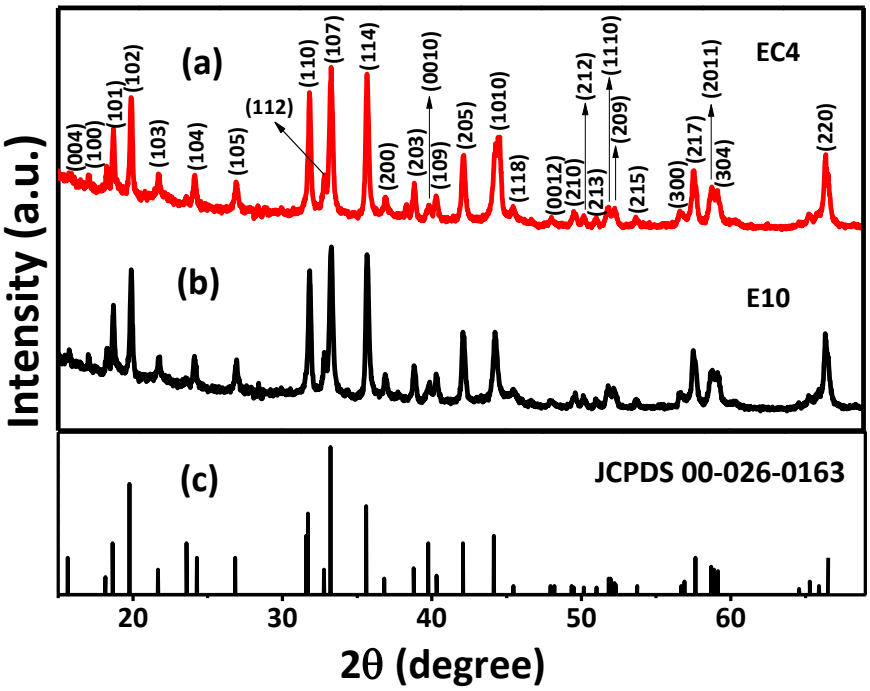

Figure 6.19: XRD patterns of samples **(a)** EC4 **(b)** E10 compared with **(c)** JCPDS card no. 00-026-0163

6.4.2. FESEM Analysis

The surface morphology of the synthesized nanophosphors was investigated through FESEM study. The FESEM images of the samples E10 and EC4 are given in figure 6.20. from the FESEM image of the sample E10 (figure 6.20 (a & b)), it was observed that the morphology contained both multifaceted plates and rods roughly stacked against each other. The length of the plates varied from 200 nm to 300 nm with plate thickness from 60 nm to 70 nm. Whereas, the rod length lied between 300 nm to 500 nm and rod thickness between 50 nm to 60 nm. FESEM images for sample EC4 are given in figure 6.20 (c & d). No effect of Ca^{2+} co-doping was seen on the morphology for sample EC4 that had a similar mix of multifaceted plate like and rod like morphology. For sample EC4 the plate length was between range 320 nm to 550 nm with plate thickness between 50 nm to 80 nm. The rod length was between 230 nm to 450 nm with rod thickness in range 60 nm to 70 nm. The plates and rods were roughly stacked against each other.

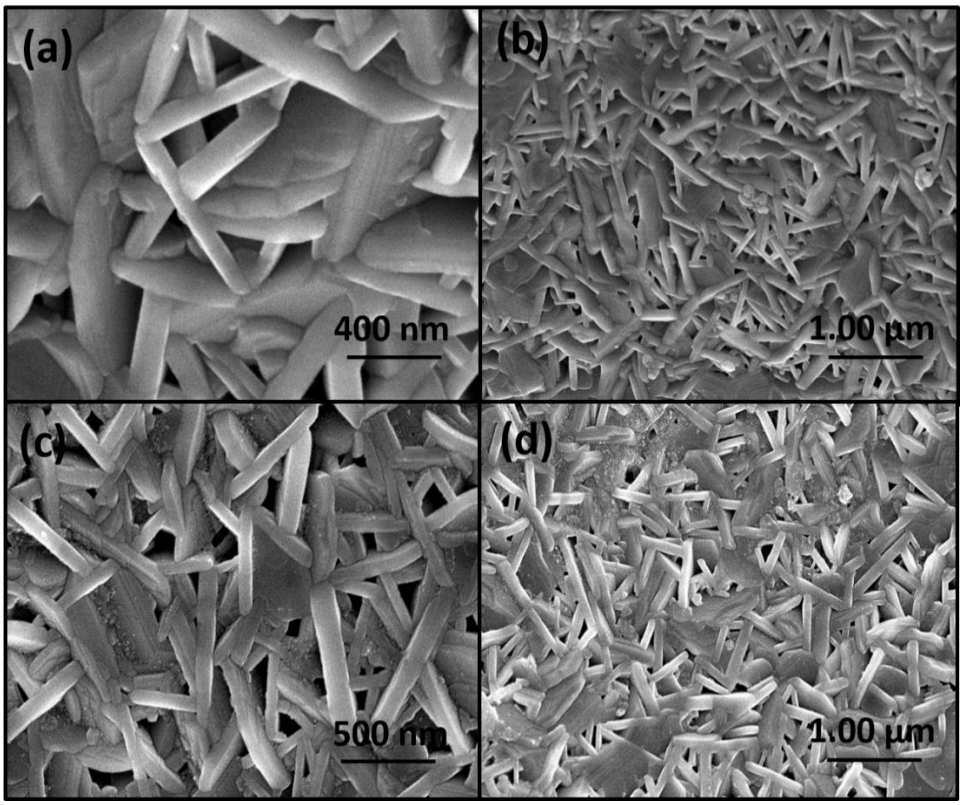

Figure 6.20: FESEM images of samples **(a & b)** E10 **(c & d)** EC4

6.4.3. TEM Analysis

TEM micrographs for samples E10 and EC4 are exhibited in figure 6.21 (a & b) and figure 6.21 (c & d) respectively. A mix of multifaceted plate like and rod like morphology was observed for both the samples concluding that the addition of Ca^{2+} ions did not alter the morphology. The result is consistent with the FESEM study. The lattice fringes for the samples E10 and EC4 as seen in figure 6.21 (b & d) respectively confirm the crystalline phase of the prepared samples. The lattice fringes at 0.28 nm and 0.33 nm for sample E10 (figure 6.21 (b)) correspond to the planes (110) and (105) respectively. Whereas, for sample EC4 the lattice fringes at 0.41 nm and 0.23 nm (figure 6.21 (d)) correspond to the planes (103) and (203) respectively.

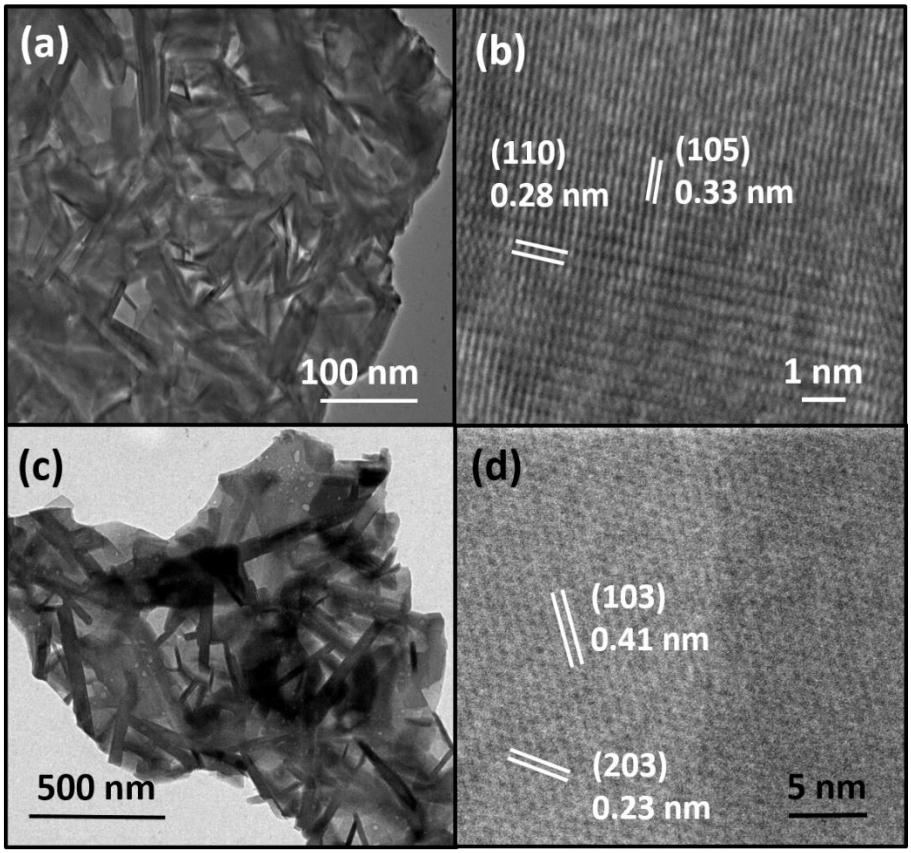

Figure 6.21: TEM micrographs of samples **(a & b)** E10 **(c & d)** EC4

6.4.4. UV-Vis Spectroscopic Analysis

The bandgap energies of the prepared samples E10 and EC4 were calculated through Kubelka-Munk plots obtained from the diffused reflectance data of the synthesized samples. The Kubelka-Munk plots for samples E10 and EC4 are illustrated in figure 6.22 (a & b) respectively. Kubelka-Munk plots are the plots between $[h\upsilon\ F(R)]^2$ and hν and the Kubelka-Munk method is given by equation (6.12) [32, 33]:

$$\boldsymbol{F(R)} = \frac{\boldsymbol{(1-R)^2}}{\boldsymbol{2R}} \tag{6.12}$$

where F(R) is the Kubelka-Munk function and R gives the absolute reflectance of the sample. The bandgap energy was calculated by extrapolating the $[h\upsilon\ F(R)]^2$ versus hν plot to the abscissa at zero F(R). The bandgap values for samples E10 and EC4 were 5.30 eV and 5.28 eV respectively. The bandgap energy did not change much with Ca^{2+} co-doping and is approximately the same for the two samples.

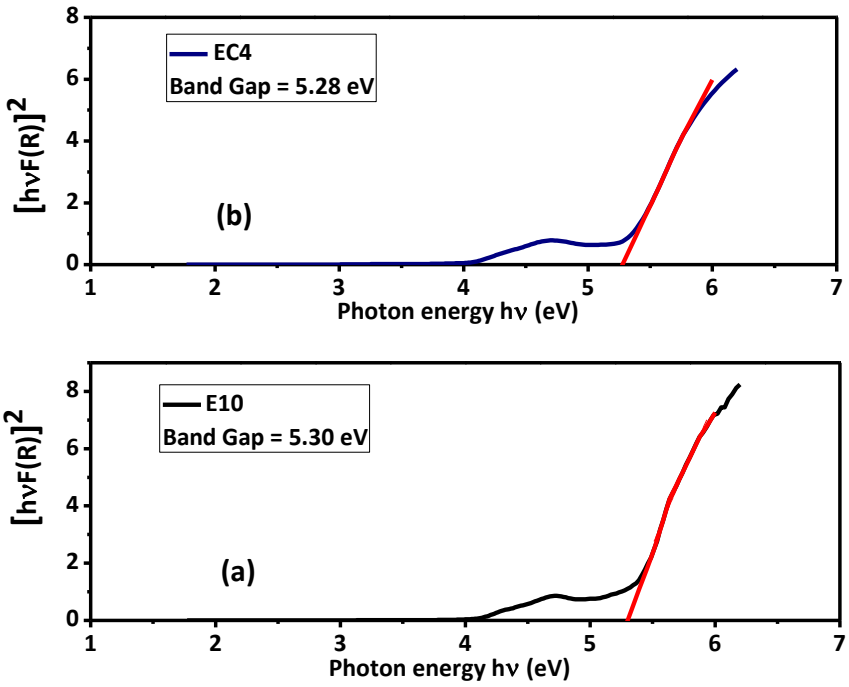

Figure 6.22: Kubelka-Munk plots for band gap calculation of samples **(a)** E10 and **(b)** EC4

6.4.5. Photoluminescence Study

The optimum concentration of Ca^{2+} ions to achieve maximum photoluminescence emission intensity was determined. Figure 6.23 shows the relative emission intensity of CaBAM:Eu^{2+} with varying concentration of Ca^{2+} ions. The maximum photoluminescence emission intensity for CaBAM:Eu^{2+} was achieved for 4 mol% concentration of Ca^{2+} ions. Beyond this concentration, the photoluminescence emission intensity was decreased due to concentration quenching.

Excitation and emission spectra of samples E10 and EC4 are given in figure 6.24 (a & b). Photoluminescence excitation spectra monitored at 450 nm wavelength exhibited a broadband with maxima at approximately 330 nm. Also, a small peak was observed at 380 nm. These peaks at 330 nm and 380 nm are due to the $4f^7$-$4f^6 5d^1$ electronic transitions of Eu^{2+} ions. Co-doping of Ca^{2+} ions did not change the position maxima of excitation band at 330 nm. The broad excitation band range (280 nm to 440 nm) matches well with the range of NUV-LED chips (380 nm to 420 nm). So, the prepared phosphor can find use in NUV-LED chips.

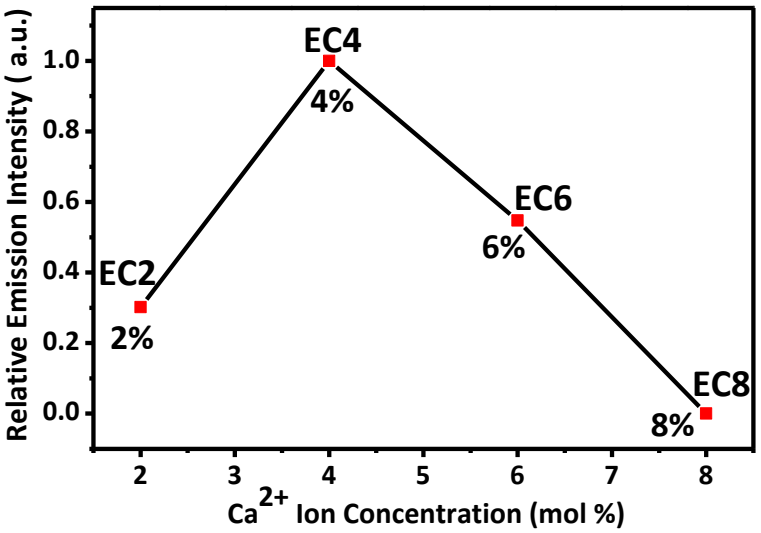

Figure 6.23: Relative emission intensity of CaBAM:Eu^{2+} with varying concentration of Ca^{2+} ions

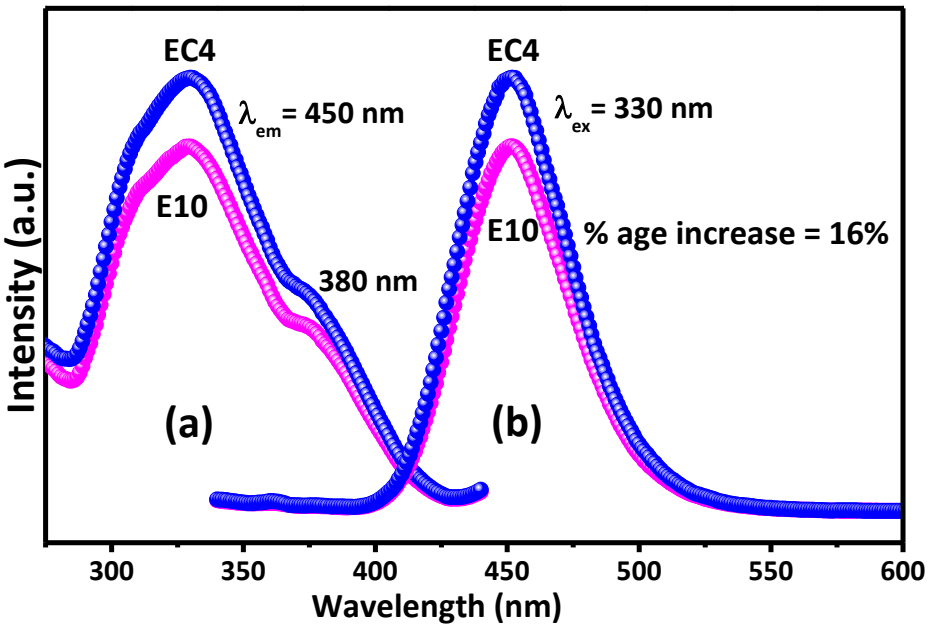

Figure 6.24: Photoluminescence **(a)** excitation spectra and **(b)** emission spectra of samples E10 and EC4

The photoluminescence emission spectra (figure 6.24 (b)) were recorded at 330 nm. The photoluminescence emission spectra illustrated a broadband peaking at 450 nm corresponding to$4f^6 5d^1$-$4f^7$ transition of Eu^{2+} ions ascribing blue color to the phosphor. Ca^{2+} co-doping did not change the peak maxima located at 450 nm but increased the photoluminescence emission

intensity by approximately 16%. The photoluminescence emission enhancement may be attributed to the following reasons. The ionic radius of Ba^{2+}, Ca^{2+} and Eu^{2+} ions is of the order Ba^{2+} (r_{Ba}^{2+} = 1.35 Å) > Eu^{2+} (r_{Eu}^{2+} = 1.17 Å) > Ca^{2+} (r_{Ca}^{2+} = 1.00 Å). The ionic radius of Ca^{2+} ions is less than that of Ba^{2+} ions. When Ca^{2+} ions replace Ba^{2+} ions, crystal field strength decreases and crystal field splitting increases. According to the crystal field theory, crystal field splitting tends to increase with the decrease in the size of host cation [42]. Therefore, with the replacement of Ba^{2+} ions by Ca^{2+} ions, the crystal field splitting increases and hence the luminescence emission intensity increases. Also, the ionic radius of Ca^{2+} ions and Eu^{2+} ions are nearly comparative and the ions with comparable ionic radius can replace each other easily at lattice sites. Hence, the Eu^{2+} ions would easily replace Ca^{2+} ions increasing the number of Eu^{2+} ions in the matrix and enhancing the photoluminescence emission intensity. The increase in the photoluminescence emission intensity occurs until the concentration of Ca^{2+} ions reach 4 mol%. After this concentration, the photoluminescence intensity decreases due to concentration quenching.

6.4.5.1. Chromaticity Coordinates with Color Purity

The CIE color coordinates and color purity of the prepared phosphors were calculated from the PL emission spectra of the phosphors using CIE coordinate calculator [11]. The color purity was calculated using the formula:

$$\textbf{Color Purity}\ (\%) = \frac{\sqrt{(x-x_i)^2+(y-y_i)^2}}{\sqrt{(x_d-x_i)^2+(y_d-y_i)^2}} \times 100 \qquad (6.13)$$

Where (x, y) are the chromaticity coordinates of the sample, (x_i, y_i) are the chromaticity coordinates of white light in the CIE diagram, taken as (0.3333, 0.3333) and (x_d, y_d) represents the chromaticity coordinates of dominant wavelength point [13]. Figure 6.25 (a & b) shows the CIE coordinates (CIEx, CIEy) for the samples E10 and EC4 respectively. The values of CIE color coordinates and color purity for samples E10 and EC4 are tabulated in table 6.9. It was inferred from table 6.9 that with the inclusion of Ca^{2+} ions in BAM:Eu^{2+}, the chromaticity color coordinates remained approximately the same and were close to the ideal blue coordinates (0.15, 0.06) [12]. The prepared phosphors exhibited good color purity of approximately 94%.

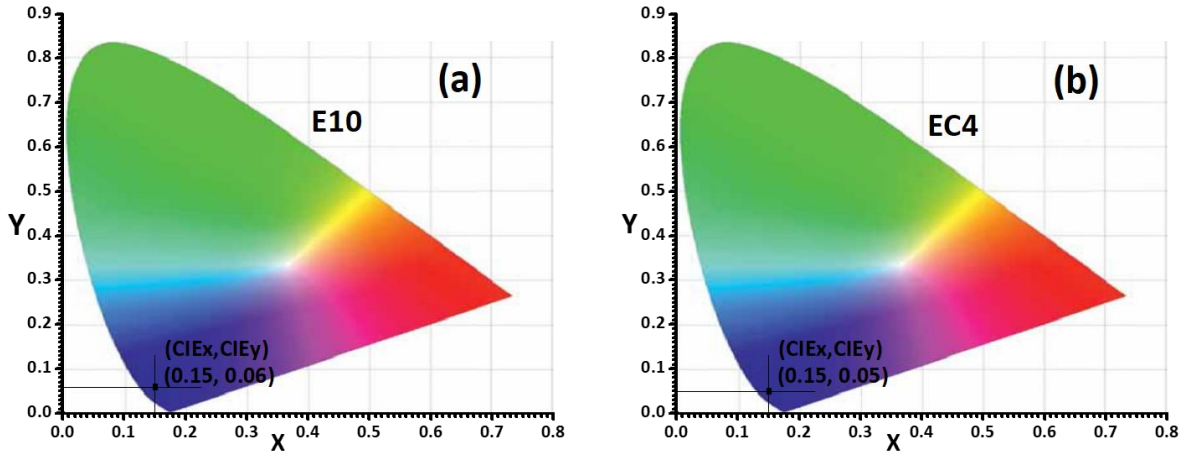

Figure 6.25: CIE chromaticity coordinate diagram for samples **(a)** E10 and **(b)** EC4

Table 6.9: CIE coordinates and color purity of samples E10 and EC4

Sample Name	CIEx	CIEy	Color Purity
E10	0.149	0.057	94%
EC4	0.146	0.054	94%

6.4.6. Thermal Stability Study

To measure the emitting potential of prepared phosphors for practical applications, the thermal stability of prepared phosphors was checked. Hence, the prepared phosphors were annealed (or baked) at 600°C for 30 minutes in ambient air as at this temperature the phosphors are heated during the fabrication of the display devices which results in the decrement of their photoluminescence emission intensity or thermal degradation [24, 25, 41]. After this heat treatment, the photoluminescence emission spectra of the baked samples were recorded at 330 nm excitation wavelength. The photoluminescence emission spectra of the baked samples E10 (baked) and EC4 (baked) in comparison to their initial emission is illustrated in figure 6.26 (a & b) respectively. It is clear from photoluminescence emission spectra shown in figure 6.26 (b) that Ca^{2+} co-doping improved the thermal stability of the phosphor. The percentage decrease in the photoluminescence emission intensity after baking was nearly 29% for E10 and 5% for EC4. When Ca^{2+} ions replace Ba^{2+} ions in the host matrix then owing to the smaller ionic radius of Ca^{2+} ions ($r_{Ca^{2+}}$ = 1.00 Å) as compared to the ionic radius of Ba^{2+} ions ($r_{Ba^{2+}}$ = 1.35 Å), lattice deformation

occurs in the host structure decreasing cation diffusion [43]. As the diffusion of cations in the interslabs of β-alumina structure of BAM:Eu^{2+} phosphor causes a decrease in photoluminescence emission or thermal degradation therefore, the restricted cationic movement would help in improving thermal stability. The other cause of thermal degradation in BAM:Eu^{2+} phosphor is the oxidation of Eu^{2+} to Eu^{3+} [24, 27-29]. As Ca^{2+} ions are more electronegative than Ba^{2+} ions hence adsorption of oxygen atoms decreases preventing oxidation of Eu^{2+} to Eu^{3+} thus improving thermal stability. Therefore, the inclusion of Ca^{2+} ions in BAM:Eu^{2+} was beneficial in improving the thermal stability of the phosphor.

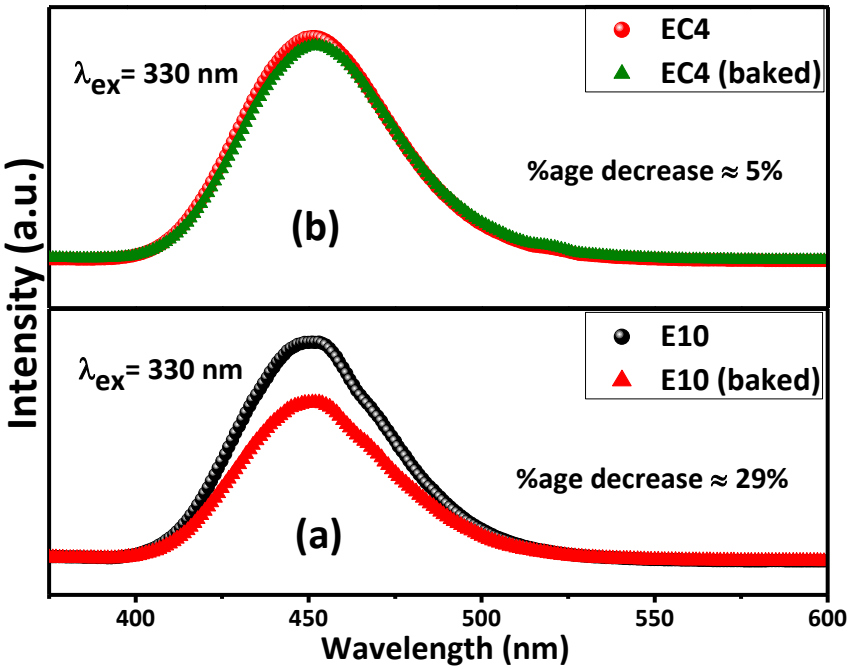

Figure 6.26: Photoluminescence emission spectra of samples **(a)** E10 (before and after baking) and **(b)** EC4 (before and after baking)

References

[1] S. Som, S. Sharma, S. Lochab, Swift heavy ion induced structural and optical properties of Y_2O_3:Eu^{3+} nanophosphor, Materials Research Bulletin, 48 (2013) 844-851.

[2] Y. Linqin, P. Xingping, S. ZHANG, W. Yuhua, W. CHANG, Photoluminescence properties of Ca-doped $BaMgAl_{10}O_{17}$:Eu^{2+},Mn^{2+} blue phosphor using BaF_2 and CaF_2 as co-flux, Journal of Rare Earths, 32 (2014) 1109-1113.

[3] Y. Zhou, J. Lin, Morphology control and luminescence properties of $BaMgAl_{10}O_{17}$:Eu^{2+} phosphors prepared by spray pyrolysis, Journal of Solid State Chemistry, 178 (2005) 441-447.

[4] R. Shanker, A. Khan, R. Kumar, H. Chander, V. Shanker, S. Chawla, Understanding and arresting degradation in highly efficient blue emitting $BaMgAl_{10}O_{17}$:Eu^{2+} phosphor—A longstanding technological problem, Journal of luminescence, 143 (2013) 173-180.

[5] K. Shinde, S. Dhoble, Luminescence in $Li_2Sr_2Al_2PO_4F_9$:Dy^{3+}-a novel nanophosphor, Luminescence, 27 (2012) 91-94.

[6] T. Peng, L. Huajun, H. Yang, C. Yan, Synthesis of $SrAl_2O_4$:Eu, Dy phosphor nanometer powders by sol–gel processes and its optical properties, Materials Chemistry and Physics, 85 (2004) 68-72.

[7] L. Jiang, C. Chang, D. Mao, B. Zhang, A new long persistent blue-emitting $Sr_2ZnSi_2O_7$:Eu^{2+}, Dy^{3+} prepared by sol–gel method, Materials Letters, 58 (2004) 1825-1829.

[8] Y. Lin, Z. Zhang, Z. Tang, X. Wang, J. Zhang, Z. Zheng, Luminescent properties of a new long afterglow Eu^{2+} and Dy^{3+} activated $Ca_3MgSi_2O_8$ phosphor, Journal of the European Ceramic Society, 21 (2001) 683-685.

[9] C. Shi, Y. Fu, B. Liu, G. Zhang, Y. Chen, Z. Qi, X. Luo, The roles of Eu^{2+} and Dy^{3+} in the blue long-lasting phosphor $Sr_2MgSi_2O_7$:Eu^{2+}, Dy^{3+}, Journal of luminescence, 122 (2007) 11-13.

[10] S.K. Sao, N. Brahme, D. Bisen, G. Tiwari, Photoluminescence and thermoluminescence properties of Eu^{2+} doped and Eu^{2+}, Dy^{3+} co-doped $Ba_2MgSi_2O_7$ phosphors, Luminescence, 31 (2016) 1364-1371.

[11] R. Nagaraja, V.P. Manjari, B. Sailaja, R. Ravikumar, A novel orange emitting Sm^{3+} ions doped $NaCaAlPO_4F_3$ phosphor: Optical and luminescence properties, Journal of Molecular Structure, 1130 (2017) 96-102.

[12] C.S. McCamy, Correlated color temperature as an explicit function of chromaticity coordinates, Color Research & Application, 17 (1992) 142-144.

[13] E.F. Schubert, Light-emitting diodes Cambridge University Press, New York, (2006) 35-40.

[14] J. Schanda, Colorimetry: understanding the CIE system, John Wiley & Sons, 2007.

[15] I.P. Sahu, D. Bisen, N. Brahme, M. Ganjir, Enhancement of the photoluminescence and long afterglow properties of $Sr_2MgSi_2O_7$:Eu^{2+} phosphor by Dy^{3+} co-doping, Luminescence, 30 (2015) 1318-1325.

[16] R. Chen, Glow curves with general order kinetics, Journal of the Electrochemical Society, 116 (1969) 1254-1257.

[17] V. Bhatia, D. Kumar, A. Kumar, V. Mehta, S. Chopra, A. Vij, S. Rao, S.P. Singh, Mixed transition and rare earth ion doped borate glass: structural, optical and thermoluminescence study, Journal of Materials Science: Materials in Electronics, 30 (2019) 677-686.

[18] D. Kumar, S. Rao, S.P. Singh, Structural, optical and thermoluminescence study of Dy^{3+} ion doped sodium strontium borate glass, Journal of Non-Crystalline Solids, 464 (2017) 51-55.

[19] N. Suriyamurthy, B. Panigrahi, Effects of non-stoichiometry and substitution on photoluminescence and afterglow luminescence of $Sr_4Al_{14}O_{25}$:Eu^{2+}, Dy^{3+} phosphor, Journal of luminescence, 128 (2008) 1809-1814.

[20] D. Kumar, S. Rao, S.P. Singh, Effect of Er^{3+} on NaSrB glass: thermoluminescence and structural analysis, Applied Physics A, 125 (2019) 38.
[21] B. Chandra, R.K. Chandrakar, V. Chandra, R. Baghel, Effect of particle size on activation energy and peak temperature of the thermoluminescence glow curve of undoped ZnS nanoparticles, Luminescence, 31 (2016) 478-486.
[22] W. Chen, Z. Wang, Z. Lin, L. Lin, Thermoluminescence of ZnS nanoparticles, Applied physics letters, 70 (1997) 1465-1467.
[23] C.R. Ronda, Luminescence: from theory to applications, John Wiley & Sons, 2007.
[24] G. Bizarri, B. Moine, On $BaMgAl_{10}O_{17}:Eu^{2+}$ phosphor degradation mechanism: thermal treatment effects, Journal of luminescence, 113 (2005) 199-213.
[25] B. Howe, A.L. Diaz, Characterization of host-lattice emission and energy transfer in $BaMgAl_{10}O_{17}:Eu^{2+}$, Journal of luminescence, 109 (2004) 51-59.
[26] Y.F. Wang, Q.Q. Zhu, L.Y. Hao, X. Xu, R.J. Xie, S. Agathopoulos, Luminescence and Structural Properties of High Stable Si–N-Doped $BaMgAl_{10}O_{17}:Eu^{2+}$ Phosphors Synthesized by a Mechanochemical Activation Route, Journal of the American Ceramic Society, 96 (2013) 2562-2569.
[27] Y.H. Wang, Z.H. Zhang, Luminescence thermal degradation mechanism in $BaMgAl_{10}O_{17}:Eu^{2+}$ phosphor, Electrochemical and Solid-State Letters, 8 (2005) H97-H99.
[28] K. Yokota, S.-X. Zhang, K. Kimura, A. Sakamoto, Eu^{2+}-activated barium magnesium aluminate phosphor for plasma displays–Phase relation and mechanism of thermal degradation, Journal of luminescence, 92 (2001) 223-227.
[29] A. Lacanilao, G. Wallez, L. Mazerolles, P. Dubot, L. Binet, B. Pavageau, L. Servant, V. Buissette, T. Le Mercier, Structural analysis of thermal degradation and regeneration in blue phosphor $BaMgAl_{10}O_{17}:Eu^{2+}$ based upon cation diffusion, Solid State Ionics, 253 (2013) 32-38.
[30] Y.-F. Wang, L. Liu, R.-J. Xie, Q. Huang, Microwave assisted sintering of thermally stable $BaMgAl_{10}O_{17}:Eu^{2+}$ phosphors, ECS Journal of Solid State Science and Technology, 2 (2013) R196-R200.
[31] J. Zhou, Y. Wang, B. Liu, J. Liu, Photoluminescence properties of $BaMgAl_{10}O_{17}:Eu^{2+}$ phosphor prepared by the flux method, Journal of Physics and Chemistry of Solids, 72 (2011) 995-1001.
[32] L. Yang, B. Kruse, Revised Kubelka–Munk theory. I. Theory and application, JOSA A, 21 (2004) 1933-1941.
[33] A.E. Morales, E.S. Mora, U. Pal, Use of diffuse reflectance spectroscopy for optical characterization of un-supported nanostructures, Revista mexicana de física, 53 (2007) 18-22.
[34] P. Pandey, R. Kurchania, F.Z. Haque, Structural, diffused reflectance and photoluminescence study of cerium doped ZnO nanoparticles synthesized through simple sol–gel method, Optik, 126 (2015) 3310-3315.
[35] F. Yakuphanoglu, R. Mehrotra, A. Gupta, M. Munoz, Nanofiber organic semiconductors: The effects of nanosize on the electrical charge transport and optical properties of bulk polyanilines, Journal of Applied Polymer Science, 114 (2009) 794-799.
[36] W. Ran, L. Wang, L. Tan, D. Qu, J. Shi, Remote Control Effect of Li^+, Na^+, K^+ Ions on the Super Energy Transfer Process in $ZnMoO_4:Eu^{3+}$, Bi^{3+} Phosphors, Scientific reports, 6 (2016) 27657.
[37] J. Chen, C. Li, Z. Hui, Y. Liu, Mechanisms of Li^+ ions in the emission enhancement of $KMg_4(PO_4)_3:Eu^{2+}$ for white light emitting diodes, Inorganic chemistry, 56 (2017) 1144-1151.
[38] J. Zhang, Z. Zhang, Z. Tang, Y. Tao, X. Long, Luminescent properties of the $BaMgAl_{10}O_{17}:Eu^{2+}$, M^{3+} (M= Nd, Er) phosphor in the VUV region, Chemistry of materials, 14 (2002) 3005-3008.

[39] G. Bizarri, B. Moine, On the role of traps in the $BaMgAl_{10}O_{17}:Eu^{2+}$ fluorescence mechanisms, Journal of luminescence, 115 (2005) 53-61.

[40] Y. Zhu, G. Zheng, X. Xin, R. Zhuang, L. Zhang, Strong luminescence enhancement of Li doped Y_2O_3:5%Eu^{3+} phosphors, Journal of Materials Science: Materials in Electronics, 28 (2017) 1485-1488.

[41] T.K. Anh, P.T.M. Chau, N.T.Q. Hai, L.Q. Minh, Cathodo-, Thermo-, and Photo-luminescent Properties of Nano $Y_2O_3:Eu^{3+}$ Fabricated by Controlled Combustion Synthesis.

[42] X. Zhang, J. Zhang, J. Huang, X. Tang, M. Gong, Synthesis and luminescence of Eu^{2+}-doped alkaline-earth apatites for application in white LED, Journal of luminescence, 130 (2010) 554-559.

[43] Y. Linqin, P. Xingping, S. Zhang, W. Yuhua, W. Chang, Photoluminescence properties of Ca-doped $BaMgAl_{10}O_{17}:Eu^{2+}$, Mn^{2+} blue phosphor using BaF_2 and CaF_2 as co-flux, Journal of Rare Earths, 32 (2014) 1109-1113.

CHAPTER 7

CONCLUSIONS AND FUTURE SCOPE

Overview

This chapter summarizes the results obtained from different experiments performed in the previous chapters (chapter 4, 5 & 6). The effect of phase purity, morphology and co-doping of different ions on the luminescence properties of BAM:Eu^{2+} nanophosphors was studied. The obtained results are concluded and summarized. At the end of the chapter, some suggestions for future work in this field are given.

7.1. Conclusions

In the present work, we report an efficient post-treatment of solution combustion synthesis route to synthesize BAM:Eu^{2+} nanophosphors with pure phase. BAM:Eu^{2+} nanophosphors were synthesized using solution combustion synthesis technique. The optimum concentration of Eu^{2+} ion was optimized to obtain maximum photoluminescence emission intensity. The photoluminescence emission intensity increased with the increase in Eu^{2+} ion concentration till 10 mol% of Eu^{2+} ion concentration. After this, the increase in ion concentration decreased the photoluminescence emission intensity due to concentration quenching. Impurity peaks of $BaAl_2O_4$ phase were observed from the XRD pattern of BAM:Eu^{2+} (10%) indicating the formation of impure phase. As phase purity is an essential parameter for achieving good photoluminescence efficiency therefore to procure pure BAM:Eu^{2+} phase, additional steps of acid leaching and annealing on the combustion synthesized powders were performed. BAM:Eu^{2+} samples obtained after acid leaching and annealing exhibited pure phasic characteristics with radical improvement in crystallinity, well-defined uniform morphology and appreciable luminescence efficiency. XRD and FTIR results for the same revealed that acid leaching was essential to get pure BAM:Eu^{2+} phase by eliminating the unwanted $BaAl_2O_4$ phase. It was also concluded from the results that annealing at 600°C helped in better crystallization of the powders. Annealing reduced the number of atoms on the surface and defect centers thereby reducing non-radiative recombinations and non-radiative relaxation centers thus enhancing photoluminescence emission intensity. These modifications in the synthesis route led to a substantial increase in photoluminescence emission intensity of about 23% in comparison to the sample prepared by conventional solution combustion synthesis route. The CIE color coordinates of monophasic BAM:Eu^{2+} nanophosphor were very close to ideal blue color coordinates with good color purity of about 94%. Therefore, a significant increase in photoluminescence emission intensity with improvement in color purity advocates the modification in the synthesis process.

To further study the luminescent properties of BAM:Eu^{2+} nanophosphors the effect of morphology on the luminescence efficiency was studied. To modify the morphology, β-cyclodextrin (β-CD) and thioglycerol (TG) were used as template agents during synthesis of BAM:Eu^{2+} nanophosphors via solution combustion synthesis route. β-CD and TG both transformed the multifaceted plate-like morphology to rod-like morphology. It was clear from the XRD, and FESEM study that inclusion of β-CD, and TG helped in obtaining increased crystallinity, crystallite size and homogeneous morphology of the nanophosphor particles.

However, incorporation of β-CD facilitated the formation of rods with larger length and hence highest photoluminescence emission intensity. In comparison to multifaceted plate like morphology, rod-like morphology gave higher photoluminescence emission intensity because rods have smaller specific surface area and exhibit less scattering of light. The scattering of light for plate like morphology was more due to the large specific surface area thus providing resistance to its photoluminescence emission efficiency. The approximate percentage increase with β-CD was 30% and with TG was 13%. Thus maximum photoluminescence emission was obtained with the addition of β-CD in BAM:Eu^{2+} nanophosphor. Photoluminescence emission and thermal stability were increased with both β-CD and TG. However, β-CD gave the highest emission output and a thermally stable nanophosphor with good color purity, which can potentially be applied in high resolution plasma display panels.

Furthermore, to study the effect of substitution on the luminescent properties of BAM:Eu^{2+} nanophosphors co-doping of Dy^{3+}, Ca^{2+} and alkali metal ions Li^{+}, Na^{+}, K^{+} was performed. Dy^{3+} co-doped BAM:Eu^{2+} nanophosphors were prepared successfully. XRD study revealed the pure phase formation of the as prepared nanophosphors. The nanophosphors had a mix of multifaceted plate like and rod like morphology as depicted from the FESEM analysis. From the thermoluminescence study, it was evident that the Dy^{3+} ions resulted in the formation of trap levels. As concluded from the photoluminescence study of BAM:Eu^{2+}/ Dy^{3+}, the Dy^{3+} ions play an important role of creating traps whereas; Eu^{2+} ions act as emission centers. A significant increase of approximately 36% was observed in the photoluminescence emission intensity of BAM:Eu^{2+}/ Dy^{3+} in comparison to BAM:Eu^{2+}. The obtained blue light had high color purity with CIE color coordinates close to ideal blue coordinates. Inclusion of Dy^{3+} ions also helped in improving the thermal stability of the nanophosphor. Thus, Dy^{3+} co-doping had been effective in obtaining a highly luminescent and thermally stable nanophosphor with good quality blue light.

The alkali metal ion co-doping in BAM:Eu^{2+} had also been an efficient co-doping. The XRD study of BAM:Eu^{2+}/Li^{+}, BAM:Eu^{2+}/Na^{+} and BAM:Eu^{2+}/K^{+} depicted the pure phase formation of the prepared nanophosphors. The crystallite size and unit cell parameters for BAM:Eu^{2+}/Li^{+} and BAM:Eu^{2+}/Na^{+} decreased due to the smaller ionic radius of Li^{+} ions and Na^{+} ions as compared to Ba^{2+} ions. There was no effect on the morphology of the prepared nanophosphors with alkali metal ion co-doping. However, the photoluminescence efficiency increased with the alkali metal ion co-doping. The maximum increase in the photoluminescence emission intensity was

observed for Li^+ co-doping. The order of photoluminescence emission intensity with alkali metal ion co-doping is $Li^+ > Na^+ > K^+$. Li^+ ion co-doping gave better result due to its least ionic radius and high electronegativity, which helped in its easy diffusion in the host lattice and its better performance as charge compensator. Also the increase in crystal field splitting in BAM:Eu^{2+}/Li^+ increased its photoluminescence emission intensity. The prepared nanophosphors exhibited good color purity with CIE coordinates near to ideal blue coordinates. Alkali metal ion co-doping was also beneficial in improving the thermal stability of the nanophosphors. BAM:Eu^{2+}/Li^+ gave the best result in terms of photoluminescence efficiency and thermal stability.

Ca^{2+} co-doping was successfully achieved in BAM:Eu^{2+} through solution combustion synthesis route. XRD study revealed the pure phase formation of CaBAM:Eu^{2+} nanophosphor. However, Ca^{2+} co-doping did not produce any change in the morphology of the prepared nanophosphor. Inclusion of Ca^{2+} ions effectively increased the photoluminescence emission intensity with good color purity and CIE color coordinates very near to ideal blue color coordinates. Thermal stability also increased with Ca^{2+} co-doping. Therefore, Ca^{2+} ions effectively improved photoluminescence characteristics.

In this work we have studied the photoluminescence properties of BAM:Eu^{2+} nanophosphors and have been successful in effectively increasing the photoluminescence efficiency of BAM:Eu^{2+} nanophosphors through phase purity, change in morphology and co-doping. All the prepared nanophosphors exhibited excellent photoluminescence characteristics with good quality blue light. The thermal stability of the prepared nanophosphors also increased remarkably through the proposed ways. However, the best result was obtained for BAM:Eu^{2+}/ Dy^{3+} nanophosphor with 36% increase in photoluminescence emission intensity in comparison to BAM:Eu^{2+} nanophosphors and a marginal decrease of 8% in thermal stability. Therefore, with such characteristics, the prepared nanophosphors can find potential applications in NUV-LEDs and high resolution display devices.

7.2. Future Scope

The quest for new findings never ends. Although extensive work has been done to enhance the photoluminescence properties of BAM:Eu^{2+} nanophosphors, still many possibilities for further research are present. Some of which are listed below:

- Effect of other polymers and chelating agents on the morphological and optical properties of BAM:Eu^{2+} nanophosphors can be studied.
- Strontium ion co-doping can be performed on BAM:Eu^{2+} nanophosphors. In addition, the combined effect of calcium and strontium co-doping can be studied.
- As Dy^{3+} ions gave best result and also as they emit in both blue and yellow region, therefore, combination of some other dopant with Dy^{3+} ion could help in achieving tunable wavelength.
- Effect of UV irradiation on the optical properties of BAM phosphors could give interesting results.